PhD Program

Bioengineering and Robotics

Curriculum

Bionanotechnology (XXXII cycle)

Year

2018/2019

STRENGTHEN OF DPNS FEATURES FOR THERANOSTIC APPLICATIONS

AND

MECHANICAL-CONTROL OF CHEMOTHERAPEUTIC EFFICACY THROUGH MODULATION OF CELL PROLIFERATION

Author

ILARIA FRANCESCA RIZZUTI

Supervisors

DR. PAOLO DECUZZI

DR. MORGAN DELARUE

A mia madre e mio figlio

Acknowledgment

I wish to thank the reviewers for their valuable comments and suggestions to improve the quality of the thesis.

The first project was partially supported by the European Research Council, under the European Union's Seventh Framework Programme (FP7/2007-2013)/ERC grant agreement no. 616695, by the Italian Association for Cancer Research (AIRC) under the individual investigator grant no. 17664, and by the European Union's Horizon 2020 research and innovation programme under the Marie Skłodowska-Curie grant agreement no. 754490. I acknowledge the precious support provided by the Nikon Center, the Material Characterization Facility, the Electron Microscopy, and

For the second project I acknowledge the *Fondation Toulouse Cancer Santè, Plan Cancer Inserm, and Cancèropole Grand Sud Ouest.* I also thank the LAAS / CNRS and the CRCT *(Centre de Recherches en Cancérologie de Toulouse)* for the technological support.

Full abstract

Solid tumors are complex biological structures which are composed of cellular and matrix components, everything being perfused by blood vessels. During tumor development, modifications of both biochemical and mechanical parameters are observed and can feedback on one another. Cancer cells constantly interact with their mechanical environment and the whole tissue is mostly confined by its surrounding. Compressive mechanical stress develops in part from cell proliferation and could eventually result in the clamping of blood vessels leading to increased interstitial fluid pressure (hydrostatic pressure). The consequent hypoperfusion poses important obstacles to drug delivery and nanomedicines. In fact, the tortuous tumor microvasculature has blood velocities up to one order of magnitude lower compared to healthy capillary networks. Moreover, the fast angiogenesis during tumor progression leads to high vascular density in solid tumors, large gaps exist between endothelial cells in tumor blood vessels, and tumor tissues show selective extravasation and retention of macromolecular drugs (Enhanced Permeation Retention – EPR – effect). These effects have served as a basis for the development of drug delivery systems which are aimed at enhancing tumor tissue targeting and drug therapeutic effectiveness. Over the last 15 years, a plethora of materials and different formulations have been proposed for the realization of nanomedicines. Yet, drug-loading efficiency, sequestration by phagocytic cells, and tumor accumulation of nanoparticle-loaded agents - nanomedicines - are sub-optimal.

Starting from these considerations, during my PhD, I studied two complementary approaches: in the first two years my work was focused on implementing the characteristics of Discoidal Polymeric Nanoconstructs designed with controlled geometries and mechanical properties. In the last year, I investigated the role of mechanical stress on chemotherapeutic efficacy.

More precisely, this work first reviews the use of deformable discoidal nanoconstructs (DPNs) as a novel delivery strategy for therapeutic and imaging agents. Inspired by blood cell behavior, these nanoconstructs are designed to efficiently navigate the circulatory system, minimize sequestration by phagocytic cells, and recognize the tortuous angiogenic microvasculature of neoplastic masses. In this work, the synthesis, drug loading and release, and physico-chemical

characterization of DPNs were enhanced with particular emphasis on the ability to independently control size, shape, surface properties, and mechanical stiffness. Two different loading strategies were tested, namely the straightforward “direct loading” and the “absorbance loading”. In the former case, the agent was directly mixed with the polymeric paste to realize DPNs whereas, in the latter case, DPNs were first lyophilized and then rehydrated upon exposure to a concentrated aqueous solution of the agent. Under these two loading conditions, the encapsulation efficiencies and release profiles of three different molecules and their corresponding prodrugs were systematically assessed (1,2-Distearoyl-sn-glycero-3-phosphorylethanolamine lipid chains or 1 kDa PEG chains were directly conjugated with Cy5.5 or methotrexate and Doxorubicin). Moderately hydrophobic compounds with low molecular weight showed encapsulation efficiencies of 80%, with absorption loading (direct loading has efficiencies around 1%). The DOX-DPN showed on triple negative breast cancer cells a toxicity comparable to free DOX. Preliminary *in vivo* preliminary studies conducted with directly loaded Cy5-DPN demonstrated a fairly solid integration of the imaging compound with the polymer matrix of the particles.

The second part of the work dissect what happens to free drugs or to drugs carried by nanovectors once they reach the tumor site. As we mention above, the elevated mechanical stress derived from tumor progression could result in blood vessels clamping with consequent reduction of drug efficacy. It is quite obvious to imagine that if the drug fails to reach the tumor it cannot act on it. Indeed, mechanical stress within the tumor site is present from the early stages of the disease. Our goal was to understand what happens when mechanical stress is not yet so large enough to fully collapse the blood vessels. Are there mechanical alterations that can affect the efficacy of a chemotherapeutic? We studied how mechanical perturbations of the tumor microenvironment could contribute to the mechanical-form of Gemcitabine drug resistance.

Specifically, we developed a new *in vitro* strategy to mimic the mechanical compression stress induced by the stroma during tumor progression. We embedded pancreatic tumor spheroids into agarose polymeric matrix in order to demonstrate the effect of mechanical compressive stress on tumor proliferation. Then, we validated our results with other types of mechanical stresses. Finally, we investigated the therapeutic efficacy of a proliferation-based chemotherapy: Gemcitabine.

Collectively, having the physical cues of cancer in mind, it can be important to cross-fertilize the fields of physical oncology and nanomedicine.

Preface

In these three years I had the opportunity to know two different multidisciplinary environments, I adapted myself to two different scientific contexts and I learned to look at things from more perspectives.

I spent my first 2 years of my PhD in the Laboratory of Nanotechnology for Precision Medicine at the Italian Institute of Technology (IIT) in Genova – Italy, under the supervision of Dr Paolo Decuzzi.

At the IIT we reviewed the use of deformable discoidal nanoconstructs (DPNs) as a novel delivery strategy for tumor therapy and imaging. We optimized the synthesis procedure, drug loading and release as well as the physico-chemical characterization of DPNs. Moreover, two different loading strategies were tested and the encapsulation efficiencies and release profiles of three different molecules and their corresponding prodrugs were systematically assessed.

In the third year of my PhD I went abroad in Toulouse (France) in the MILE group at the LAAS-CNRS under the supervision of Dr. Morgan Delarue. For six months of that period, I mainly worked at CRCT *(Centre de Recherches en Cancérologie de Toulouse)* in the Julie Guillermet's research group (Morgan Delarue's collaborator) to acquire skills on biological techniques and pancreatic cancer.

In the MILE team we investigated the effect of a drug from another perspective: considering that the drug entered the tumor, we worked on how mechanical perturbations of the tumor microenvironment may contribute to modulating the efficacy of a drug.

Each project require specific introduction and chapters, so I decided to write my work accordingly. Each chapter has a dedicated introduction, methods, results, conclusion and discussion. I finish my thesis by a global discussion on nanomedicine and mechanics.

Specifically, the manuscript is organized in five main chapters which read as follows.

Chapter 1 Introduction: brief global introduction of the two main thesis topics.

Chapter 2 Tune and strengthen of DPNs features for theranostic applications: context composed of a global view of the existing nanomedicine systems, main obstacles of their development (physiology of the tumor, immune response and poor efficiency of drug loading); focus of the work, presentation and evaluation of the developed methods and results, and finally main conclusions.

Chapter 3 Mechanical control of chemotherapeutic drug efficacy: context composed of the role of mechanical stress during the cancer progression, mechanical-forms of drug resistance, Gemcitabine chemotherapeutic mechanism of action and pancreatic cancer cells as a model of this study; focus of the work, presentation and evaluation of the developed methods and results, and finally main conclusions.

Chapter 4 Conclusion and prospective: global conclusion and discussion on the two main topics, connecting the dots and describing the next challenges, and how my work rationalize some of these challenges.

Valorization: brief description of the two main objectives and emphasis on the main activities and publications disseminated during this PhD work.

Appendix: a. Nanotechnology tools (brief description of the main nanotechnology instruments used for the nanofabrication and particles characterization, I reported also the references of the books where they come from and on which there are the full descriptions); **b. A mathematical model perfectly predicts the effect of compressive stress on drug efficacy (**full mathematical specifications of the model developed to predict the influence of mechanical stress on chemotherapeutic efficacy).

Contents

1. Chapter: Introduction

Solid tumors consist of different structural components in addition to tumor cells, such as blood and lymphatic vessels, the extracellular matrix (ECM) with its more common constituents that are collagen, hyaluronan and stromal cells. The presence of these components in a solid tumor can vary depending on the type, organ of origin and stage of growth and can participate in mechanical stress generation inside and around the tumor.

Considering the fact that tumor progression is described by the development of tumor and/or stromal mass at the expense of the surrounding host tissue, the development of a tumor is associated with the generation and accumulation of mechanical stress. In this sense, solid tumors carry an interesting and complex mechanical system involving both solid and fluid mechanics in which the stresses arising from the solid phase of a tumor determine, largely, both fluid stresses and cancer progression (1) (2). Solid stresses can affect the physiology of tumor cells either directly by compressing them, or indirectly by compressing blood and lymphatic vessels. On the one hand, compressive mechanical stress partly develops from cell proliferation in a confined environment, and can modulate cell division and migration and potentially induce cell death (3) (4) (5) (6) (7). Futhermore, the compression of the blood vessels causes hypoperfusion and dysfunction of the lymphatic vessels. Hypoperfusion and interstitial hypertension pose important obstacles to drug delivery and may exclude large intratumor areas from chemotherapeutic agents coming from the blood, which could lead to reduced efficacy of chemotherapy and nanomedicine (8) (9).

Despite the multiple origins of solid stress involved in tumors and their pleiotropic role in tumor progression and treatment, few works have been dedicated to the area of cancer biomechanics and compressive solid stress.

During tumor development, modifications of blood vessels permeation and blood velocity occur. Angiogenesis leads to high vascular density in solid tumors, large gaps exist between endothelial cells in tumor blood vessels, and tumor tissues show selective extravasation and retention of macromolecular drugs (Enhanced Permeation Retention – EPR – effect) (10). More importantly, the tortuous tumor microvasculature has significantly different biophysical features as compared to healthy capillary networks. The mean blood velocities in tumors are up to one order of magnitude lower because of the overall higher hydraulic resistance and lower perfusion, as compared to normal vascular networks (11). These effects serve as a basis

for development of new types of nanomedicines. Over the last 15 years, a plethora of materials and different formulations have been proposed for the realization of nanomedicines. Yet, drug-loading efficiency, sequestration by phagocytic cells, and tumor accumulation of nanoparticle-loaded agents - nanomedicines - are sub-optimal. (12)

Starting from these considerations, two complementary approaches to study these issues were tried: first, an attempt was made to implement the characteristics of controlled release specialized nanovectors (Chapter 2), then we investigated the role of mechanical stress on therapeutic efficacy (Chapter 3).

In particular in the first work, a top-down hybrid fabrication strategy, combining nanoscale lithographic techniques, wet etching, and polymer chemistry, was developed to tailor the size, shape, surface properties, and mechanical stiffness of Discoidal Polymeric Nanoconstructs. Atomic force microscopy was conveniently used for testing the mechanical properties of these Nanoconstructs. Moreover, was enhanced the encapsulation and stability of payloads of DPNs: was identified a new loading strategy for achieving encapsulation efficiencies well above 80%. The geometrical properties of all DPN configurations were plenty characterized using transmission electron microscopy, multisizer coulter counting, and dynamic light scattering. In addition, Miguel Ferreira and other colleagues did a systematic analysis of the loading and release for a variety of imaging and therapeutic agents loaded into DPNs (1,2-Distearoyl-sn-glycero-3-phosphorylethanolamine lipid chains or 1 kDa PEG chains were directly conjugated with Cy5.5 or methotrexate and doxorubicin).

In the second part we investigated how mechanical stresses modulate the response to biochemical signaling. Several recent works suggest that mechanical stresses alter chemical signaling from the microenvironment, which can play a role in tumor progression. In this context however, the precise role of the microenvironment and its interactions with the tumor are poorly understood (13). Recent evidences notably suggest that increased rigidity of the microenvironment is linked to resistance of solid tumors to chemotherapy. We investigated the impact of mechanical stress, in particular compressive, in the efficacy of drug treatment. We demonstrated a reduction in proliferation of compressed pancreatic cancer spheroids then, we proved that the mechanical stress affect the efficacy of a proliferation-based chemotherapeutics.

2. Chapter: Tune and strengthen of DPNs features for theranostic applications.

2.1. Context

2.1.1. Nanomedicine

Nanomedicine is the application of nanotechnology to medicine (14) (15) (16). Nanomedicine derive from the merging of different knowledges coming from chemistry, biology, physics, mathematics, and engineering (17). However, biological, physical, chemical, mechanical, and optical properties at the nanoscale level differ from those of the larger, "bulk", counterparts.

The most important concept in this field is the possibility to design multifunctional nanoparticles (NPs) that can provide numerous benefits. In particular, compared to conventional medicines, NPs can improve efficacy, bioavailability, targeting ability, and safety of systemically administered drugs (14) (18) (19) (20).

The physical characteristics of NPs can differ in many ways (21). Among the key parameters, there are:

- Size: NPs have at least one dimension in the range of 1 to 100 nm, although they can also be micrometer-sized particles. In this way they have novel structural, optical, and electronic properties. They also have improved solubility and increased bioavailability and circulation time;

- Shape: NPs can be spheres, discs, hemispheres, cylinders, cones, tubes, and wires. In this way, different physical and steric interactions, loading capacity, and transport capabilities can be modulated;

- Surface area: as particles size decreases, the ratio between volume and exposed area increases significantly. An increase in surface area means that a greater portion of atoms are located on the particles surface relative to the core. This makes NPs more reactive and more prone to be conjugated with electrostatic charges or biomolecules selected for targeting or other purposes;

- Permeability: NPs small size can facilitate the crossing of biological barriers that are normally not accessible. For example, NPs can transport anti-cancer drugs into tumors

according to the Enhanced Permeation and Retention (EPR) effect, through which drug delivery systems smaller than 200 nm should target passively tumors (22); or they can cross the blood-brain barrier through the use of different uptake mechanisms.

One of the most interesting capability in nanomedicine is the functionalization of NPs by altering NPs properties through chemical or physical modifications applied to achieve a specific effect. Various approaches to functionalize NPs include:

- Targeting: NPs can be actively targeted using cell-specific ligands, magnetic localization, and/or size based selectivity (23) (24). The targeting property can enhance the efficacy of NP drug-delivery systems while significantly reducing toxicity (22);

- Surface Conjugation: the NP surface can be conjugated to a lot of biomolecules for different purposes. Some candidates are fluorescent dyes for imaging (25), agents for genetic therapy such as small inhibitory RNA (siRNA) (26), targeting molecules that bind to highly expressed tumor cell receptors to facilitate the transport of imaging contrast agents, which aid in tumor detection;

- Improved bioavailability: opsonins, immune system proteins, are the proteins in charge of activating the immune complement to mark the NPs for destruction by macrophages and other phagocytes (27). Opsonins recognize less neutral NPs than charged particles, and hydrophilic particles less than hydrophobic particles. It is possible to design NPs to be neutral or conjugated with hydrophilic polymers (such as polyethylene glycol - PEG) to prevent opsonization, prolonged circulation time, reduce RES uptake, and/or enhance biocompatibility (28) (29).

- Controlled release: NPs can also be designed to be activated to release therapeutic or diagnostic molecules in response to a site-specific trigger such as pH, temperature, magnetic field, enzymatic activity, and light or radiofrequency signals (14). For example, the acidic environment inside inflammatory and tumor tissues (pH 6.8) and cellular vesicles, such as endosomes (pH 5.5–6.0) and lysosomes (pH 4.5–5.0), can be exploited to trigger drug release (30).

Nanoplatforms are commonly classified in some principal categories: the most widely used are dendrimers, micelles, nanotubes, nanoshells, liposomes, and polymeric nanoparticles (Figure 1) (21).

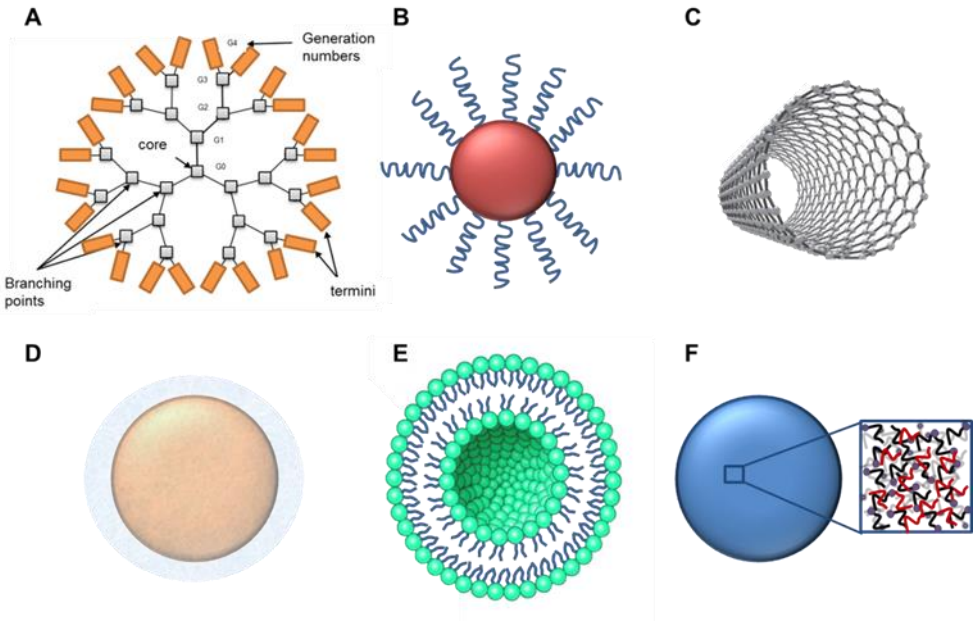

Figure 1. Schematic Representation of Nanoparticles. *A. Dendrimers. B. Micelles. C. Nanotubes. D. Nanoshells. E. Liposomes. F. Polymeric nanoparticles.*

Figure 1A depicts the schematic of dendrimers. They are branched polymeric macro-molecules forming a star-like structure made of a repetition of starting small units (31) (32) (33). Dendrimers present a size ranging from 1 to 20 nm and due to their dimensions, they are rapidly uptaken by cells and provoke a reduced activation of the immune system. Their propensity to form complex with biomolecules present in the circulation limits their use in clinic.

Micelles (Figure 1B) are composed by an inner hydrophobic core, suitable for the entrapment of non-polar molecules, and an external hydrophilic layer, crucial for their solubility in aqueous solutions. They are made of a single layer of phospholipids and present a size of about 7-35 nm. The main advantage in their use is the great easiness of the synthesis process. However, the main limitation concerns their impossibility to transport hydrophilic molecules (34).

Carbon nanotubes, depicted in Figure 1C, are composed of a distinct molecular form of carbon atoms that give them unusual thermal, mechanical, and electrical properties (35). If modified with PEG, they are surprisingly stable in vivo, with long circulation times and low uptake by the reticuloendothelial system (RES).[48] Carbon nanotubes have been used for the delivery of imaging and therapeutic agents and in the transport of DNA molecules into cells.

Carbon nanoshells (Figure 1D) are composed of a silica core that is covered by a thin metallic shell, usually composed of gold. Their primary use is in thermal ablation therapy but they also scatter light, a property which is useful for cancer imaging (36).

Nevertheless, the most common drug delivery systems are liposomes and polymeric nanoparticles.

Liposomes (Figure 1E) are constituted by one or multiple lipid double layer and thus, in the latter case, present two aqueous phases, one in the core and one between the bi-layers in which it is possible to entrap polar molecules (37). Instead, non-polar molecules can be loaded in the lipid bilayer. To increase their circulation half-life, liposomes can present also PEG in the external layer and this addition has been shown to increase by ten-fold the circulation half-life of liposomes (38). Moreover, by using lipids of different fatty-acid-chain lengths, scientists can construct liposomes to be temperature-sensitive or pH-sensitive, thereby permitting the controlled release of their contents only when they are exposed to specific environmental conditions. In 1995, "Doxil", the first liposomal platform has been approved by FDA as therapeutic agent for the treatment of AIDS-associated Kaposi's sarcoma. It represents a liposome formulation loaded with Doxorubicin (39) (40).

Finally, polymeric nanoparticles (Figure 1F) are colloidal system realized by amphiphilic molecules. This platform usually presents a spherical-like structure with a size range of approximately 50-250 nm. Generally a block of co-polymers is used to have both the hydrophobic and the hydrophilic part. Based on the synthesis procedure, it is possible to obtain two different systems: nanoparticles with a polymeric hydrophobic core and nanoparticles with an aqueous core surrounded by the polymer (22). Several clinical studies have already used polymeric nanoparticles (41). The choice of the material used is fundamental for the physico-chemical characterization, the pharmaco-kinetic properties, and the biodegradability of NPs. Biodegradable polymers are of particular interest, since they can be fully metabolized and removed from the body, creating non-toxic NPs (42). Poly-lactic-co-glycolic acid (PLGA) is an especially intriguing example of a biodegradable polymer, since relative proportions of his components, polylactic acid (PLA) and polyglycolic acid (PGA), can be used to tune the biodegradability of PLGA (43).

More recently, another nano-platform has been developed. It consists of an inner hydrophobic core made of the polymeric matrix (PLGA) and an external layer made of lipids monolayer.

Some of these lipids are also conjugated with PEG to stabilize more the nanoparticle in circulation (28) (29). This platform combine higher rate of loading efficiency of non-polar molecules, but presents also a lipid layer to resemble more to biologic vesicles (44).

2.1.2. Three major challenges to improve the Nanoparticles performance

Nanoparticles for the systemic delivery of therapeutic agents and imaging passed the preclinical studies for treatment and cancer detection (45). Compared to the free drugs, agents loaded within nanoparticles (nanomedicines) enhance the bioavailability and blood longevity, increase the protection against degradation and promotes higher accumulation and controlled release at biological targets. In addition, nanoparticles can carry multiple and different agents, for the combination therapy (46) (47), multimodal imaging (48) (49) and theranostics (combined delivery of therapeutic agents and imaging (50) (51)). Despite all of these advantages, nanomedicines are yet to be fully part of clinical therapy. In the process of improving the performance of systemically injected nanoparticles, three major challenges should be addressed: i. increasing loading efficiency and controlled release of therapeutic molecules; ii. mitigating recognition by the mononuclear phagocytic system (MPS); iii. enhancing tissue-specific accumulation.

Over the last 15 years, a large number of different nanomedicines have been proposed. Yet amounts of encapsulated drugs are still a minor portion of the overall nanoparticle mass, leading to inadequate loading efficiencies. In most lipid or polymeric-based delivery systems, only up to 10% of the nanoparticle mass is constituted by active therapeutic agents (52) (53). Indeed, the drug, in order to achieve therapeutically effective doses, is administered in a large mass of inert materials. This inadequate loading efficiency could lead to a local or systemic toxicity, especially due to the large amount of material to be administered.

The second challenge is related to the modulation of the nanoparticles interaction with the MPS. Nanoparticles are seen as foreign objects and they tend to be rapidly coated by opsonins from the complement system that facilitate their recognition and sequestration by professional phagocytic cells, mostly located within the liver (Kupffer cells) and the spleen (splenic macrophages) (54) (55). Results from biodistribution studies indicated that over 50% of the injected dose of nanoparticles is trapped into filtering organs (liver and spleen) (56) (57) (58) (59) (60) (61).

Non-specific MPS sequestration is closely linked with the third challenge, which is related to enhancing the accumulation of injected nanoparticles at the biological target. Importantly, a recent retrospective study documented that, on average, only 0.7% of the injected nanoparticles actually reach the neoplastic mass (62). Therefore, starting from these considerations, with this work we tried to make a contribution to reduce "the nanoparticles weaknesses".

2.1.3. The Current Paradigm in Cancer Nanomedicine Design

In preclinical animal models Maeda et al. (10) observed that the rapid tumor vascularization is characterized by a discontinuous endothelium and exhibit irregular openings (fenestrations) ranging in size in the few hundreds of nanometers scale. Consequently, through these fenestration, sufficiently small nanoparticles could passively penetrate and be retained within the tumor, following a process named the enhanced permeability and retention (EPR effect) (10). Furthermore, longer circulation half-lives may enhance the tumor accumulation (the number of passages into the diseased vasculature would increase). Inspired by the EPR effect and the need for long circulation times, a large number of nanoparticles for cancer treatment and imaging are synthesized with a spherical shape, an average diameter of 100 nm, and a surface mostly decorated with polyethylene glycol (PEG) chains. Currently, this is the major paradigm for cancer nanomedicine design. Referring on the self-assembly, organic materials have been used, such as lipids, polymers, block copolymers, and combinations thereof, as well as non-organic materials, such as iron oxide, gold, silver, and carbon-based materials (63) (64) (65) (66) (67) (68) (69) (70). Despite such an incredibly large number of formulations, tumor deposition is about 1% on average of the injected dose (62).

2.1.4. Biological Inspiration in Cancer Nanomedicine Design

After injection, nanoparticles are transported by hemodynamic forces into the blood vessels. On the way, nanoparticles are surrounded by a multitude of cells and molecules, including the abundant red blood cells (RBCs) occupying from 40% to 50% of the vascular volume. Under flow, deformable RBCs tend to accumulate within the vessel core, leaving a "cell-free layer" next to the walls (Figure 2) (71). The leukocytes and platelets, which are much less abundant than the RBCs, are pushed laterally towards the wall, in the area we have just called "cell-free layer". This behavior facilitates the wall adhesion, and extravasation of leukocytes and platelets. This is particularly relevant at sites of inflammation, where leukocytes abandon the vascular district and invade the tissue (72) (73) (74). Taking inspiration from these

phenomena, one of the solutions could be the design of particles that margin in the cell-free layer such as leukocytes and platelets and efficiently reach vascular abnormalities, such as the presence of fenestrations. However, since RBCs form a very compact block of cells in the core of the vessel, only the fairly large particles would be pushed laterally near the vessel wall. Small particles (10-500 nm) would move quite comfortably between the red blood cells and accumulate less efficiently in the cell-free layer (Figure 2) (75).

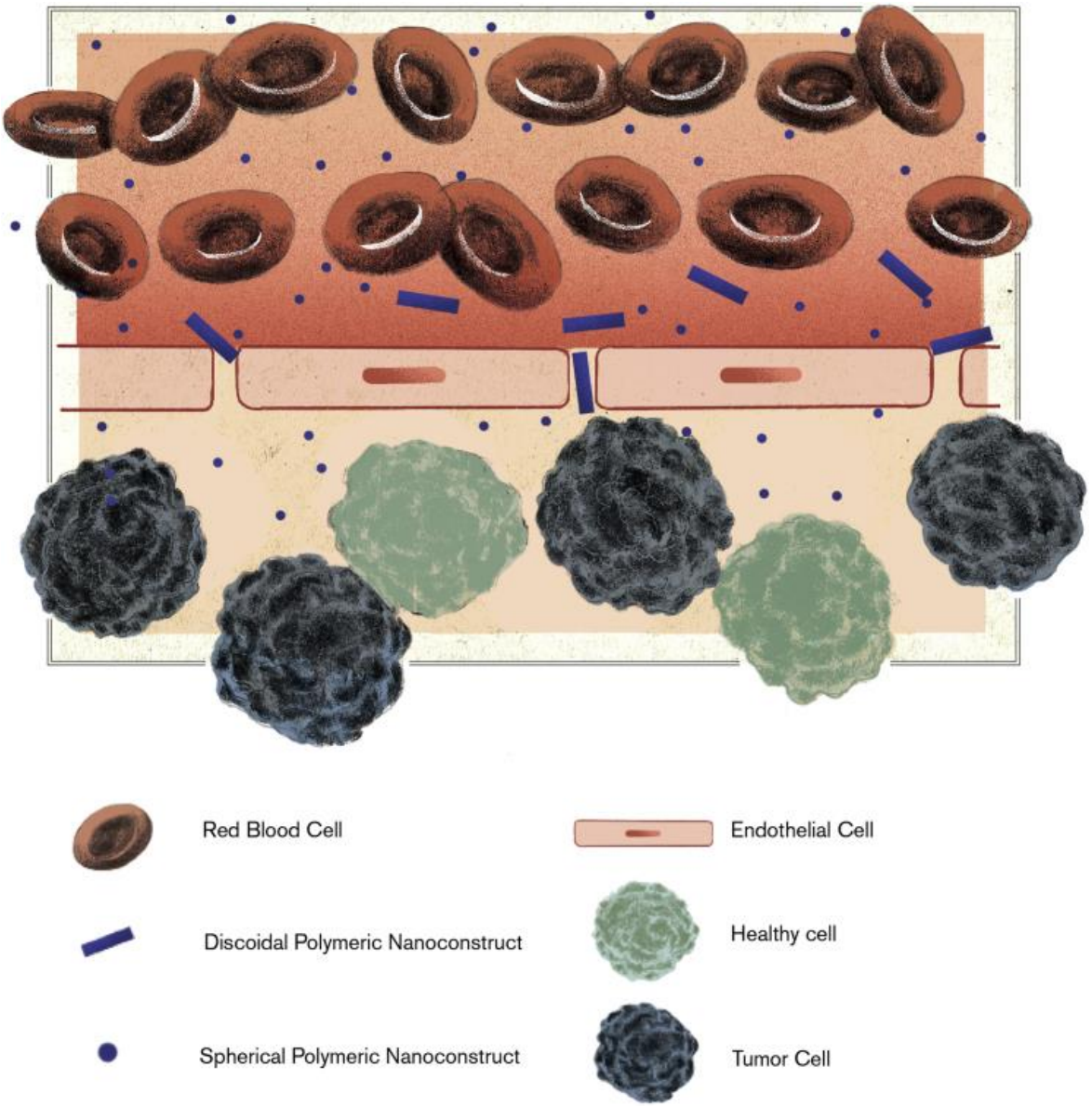

Figure 2. *(Lee T. R. et al., 2013)****Distribution of Red Blood Cells and Nanoparticle accumulation within the Tumor Parenchyma Vascular.*** *RBCs tend to accumulate within the vessel core, leaving a cell-free layer next to the wall. Nanoconstructs with comparable in size to RBCs (0.8-9µm), tend to be pushed laterally and accumulate within the cell-free layer next to the vessel walls. In contrast, small nanoparticles can find their way within the shoal of RBCs and tend to be distributed quite uniformly across the blood vessel* (75)*. Small nanoparticles passively cross the endothelial fenestrations and accumulate in a perivascular position. Sub-micrometric and micrometric nanoconstructs, which are sufficiently deformable, adhere to the vessel walls and could squeeze in through fenestrations* (12)*.*

Furthermore, particles of non-spherical shape, such as cylindrical or discoidal would increase the likelihood of border and escape the flow of RBCs. Therefore, aiming at enhancing lateral margination, one could design particles with size similar to platelets and with a non-spherical shape.

Another challenge consider is the realization of adherent particles. It is important to underline that the tumor microvasculature has different biophysical characteristics compared to healthy tissues. The average speed is one order of magnitude lower than in normal vascular networks due to greater hydraulic resistance and lower perfusion (8). Moreover, the tumor capillaries express specific and more abundant endothelial receptors (76). Then, the right combination of particles size and shape is crucial for the adhesion to the tumor microvasculature. In particular, discoidal and cylindrical particles expose a greater surface area for adhesion to the vessel wall and therefore have the possibility of establishing more molecular bonds and colloidal interactions with endothelial cells than spherical particles. In addition, the hemodynamic displacement forces from the RBCs flow would be less effective on adherent particles. Therefore, referring to a given volume, the non-spherical shape is fundamental to maximize interactions with endothelial cells and minimize the hemodynamic displacement forces (figure 2) (77) (78). Another alternative might seem the realization of small but discoid shaped particles. Those particle would feel, like the spherical ones, the hemodynamic forces of displacement and would easily settle even in healthy capillaries giving a non-specific release. The larger size solves this problem because large cylindrical particles would be affected by the displacement force not only in healthy vessels but also in tumor vessels. Upon arriving at the tumor site, they would accumulate and release the drug more easily due to the tortuous capillaries. Therefore, within the tumor vasculature, we would have a preferential deposition of submicrometric particles with cylindrical or discoidal shape. In recent years, this discovery has led to the development of sub-micrometric release particle systems. For example, discoid mesoporous silicon particles have been designed, which tend to preferentially release in the tumor site due to a favorable balance between adhesion and dynamic marginalization (78) (79) (80) (81). More recently, Merkel et al. (82) (83) have introduced long - circulating particles which mimic the RBCs. In fact, the administration of micrometric and submicrometric particles mainly raises concerns such as: sequestration from macrophages, difficulty in crossing the tumor endothelium and limited blood longevity. However, these concerns could be addressed by employing deformable particles. But, deformable particles with RBCs size would travel within the vessel core together with RBCs,

decreasing the probability of extravasation and release. However, instead particles in the sub-micron to micron size range would be pushed laterally by the abundant RBCs flow and confined to moving in the cell-free layer bouncing between endothelium and RBCs (Figure 2). Also, deformable particles would squeeze and navigate better through smallest cerebral capillaries and in the lungs and spleen microcirculations (82) (83). Moreover the resistance of deformable particles to macrophage uptake would limit their sequestration by Kupffer cells (11). On the other hand, the smaller particles can be rapidly absorbed by the Kupffer cells and easily permeate the discontinuous hepatic endothelium and end up in the Disse space. To conclude, the deformable particles are able to squeeze and infiltrate in the abnormal fenestration of tumor capillaries and circulate in the blood for a long time, like platelets and RBCs.

2.1.5. top-down synthesis approach

Spherical nanoparticles are generally synthesized by favoring the self-assembly of molecules, polymeric chains or grains under vigorous steering (84) (85) (86). Differently, non-spherical particles are fabricated via a top-down approach, involving techniques widely utilized in the microelectronic industry. Very few research groups have documented the fabrication and *in vivo* application of non-spherical particles for biomedical applications. Well known are the works presented by the groups of Ferrari (87); De Simone (88); Mitragotri (89); and Park (90). Sub-micrometer mesoporous silicon particles with a quasi-hemispherical, discoidal and cylindrical shape were fabricated by Ferrari and collaborators combining optical lithography and electrochemical etching (91). De Simone and co-workers have demonstrated differently shaped nanoparticles with a characteristic size as small as 200 nm, utilizing a proprietary methodology known as PRINT (particle replication in non-wetting templates) (92) (83). Mitragotri's group has utilized mechanical stretching and the intrinsic viscoplastic properties of several polymers to morph the shape of originally spherical micron-sized particles (89). The laboratory of Park has developed a sacrificial hydrogel template approach to synthesize variously shaped particles, mostly in the micron-sized regime, for controlling the long term release of therapeutic agents (90) (93).

Key et al. (94) presented a novel top-down approach for the facile synthesis particles with a precise control on size, shape, surface properties, and mechanical stiffness. The approach was demonstrated for the production of discoidal polymeric nanoconstructs (DPNs). Importantly, this platform shown an unprecedented blood longevity and accumulation within the tortuous

tumor neovasculature. The sub-micrometric size and deformability of discoidal polymeric nanoconstructs minimizes permeation across the liver endothelium and the non-specific sequestration by hepatic Kupffer cells.

2.2. Focus of the work

Considering the mentioned promising results about the DPNs we can say that this platform could put into practice the above-described notions of marginating, adhering, and deformable nanoparticles. However, the production method was time and resources consuming. In addition, the nanoconstructs yield was around 13% respect to the theoretical number. Furthermore, the encapsulation efficiency was around 1%.

The first aim of my PhD project was to enhance DPNs production and DPNs properties in term of stability in circulation, ability to reach the targeted cells and to load and release the drug more efficiently, avoiding the sequestration from phagocytic cells of the immune system. Moreover the pharmacological properties of DPNs were finely tuned by changing the loading strategies and compound properties (hydrophobicity and molecular weight).

Specifically here, a hybrid fabrication strategy, combining nanoscale lithographic techniques, wet etching, and polymer chemistry, was developed to tailor the size, shape, surface properties, and mechanical stiffness of nanoconstructs. This strategy is more precise, reproducible, quicker and more efficient than the previous one. Going into details the nanoconstruct geometry (size and shape) is imposed with a master silicon template, which is realized via direct laser writing for sub-micron to micron sizes (5000 nm to 600 nm). Circular, rectangular, elliptical, hexagonal, square, triangular, and other shapes can be readily realized. Nanoconstruct thickness can also be modulated by properly adjusting the etching of the silicon wafers. The nanoconstructs are obtained by polymerizing a mixture of poly(lactic-co-glycolic acid) (PLGA) and PEG chains in a sacrificial template (imposed with the silicon master template), which is then dissolved in water under gentle agitation. Polymer concentrations affect the hydrophobicity of the particles matrix, thus influencing water content and deformability. Low PEG concentrations lead to more hydrophobic matrices, which are characterized by reduced swelling and lower deformability, whereas high PEG concentrations lead to more hydrophilic matrices, which are associated with increased swelling and higher deformability.

Atomic force microscopy can be conveniently used for testing the mechanical properties of these nanoconstructs, whose Young's modulus can vary from a cell-like value (Young's modulus of 10 kPa) to that of more rigid blocks (Young's modulus on the order of 10 MPa). Furthermore, these nanoconstructs are constituted by polymer matrices comprising both hydrophobic and hydrophilic micro-domains that serve as pockets for a variety of therapeutic and imaging molecules. Surface properties can be readily modified after releasing nanoconstructs and activating PLGA terminations for chemical conjugation with antibodies, peptides, aptamers, and various other ligands. Also, lipid and polymer-drug conjugates and contrast agents can be readily incorporated within these polymeric matrices, leading to the development of theranostic agents. Moreover, as we said above, the encapsulation of therapeutic into nanoparticles has substantial impact in clinical medicine. The traditional approach, based on DPNs direct loading, where therapeutic and imaging agents are dispersed within the polymeric paste and directly loaded into the wells of the template, demonstrated often inefficient, leading to low encapsulation values. In this project was enhanced the encapsulation and stability of payloads of DPNs: was identified a new loading strategy for achieving encapsulation efficiencies well above 80%. In particular, we developed a new and innovative drug loading system using the absorption effect of the polymeric matrix to intercalate the drug with the polymer. In addition, Ferreira et al did a systematic analysis of the loading and release for a variety of imaging and therapeutic agents loaded into DPNs. Six different compounds were realized by conjugating directly 1,2-Distearoyl-sn-glycero-3-phosphorylethanolamine (DSPE) lipid chains or 1 kDa PEG chains with the near-infra red molecules Cy5.5 or the chemotherapeutic molecules methotrexate (MTX) and doxorubicin (DOX). The resulting six compounds present different molecular weights and hydrophobicity levels as compared to the original, unconjugated molecules. The six compounds are entrapped within the polymeric matrix of DPNs using both loading strategies (the old and the new one); and the encapsulation efficiencies and release profiles are consequently assessed. Finally, the pharmacological properties of DPNs are documented in vitro on triple negative breast cancer cells (MDA-MB-231) and in vivo in healthy mice.

1.1. Methodologies

1.1.1. Fabrication of DPNs silicon master template

Discoidal polymeric nanoconstructs were synthesized by employing a top-down fabrication process that can be split into four main phases that during this work were analyzed separately: spin coating, laser writing, deep reactive ion etching, and silanisation (fig. 3).

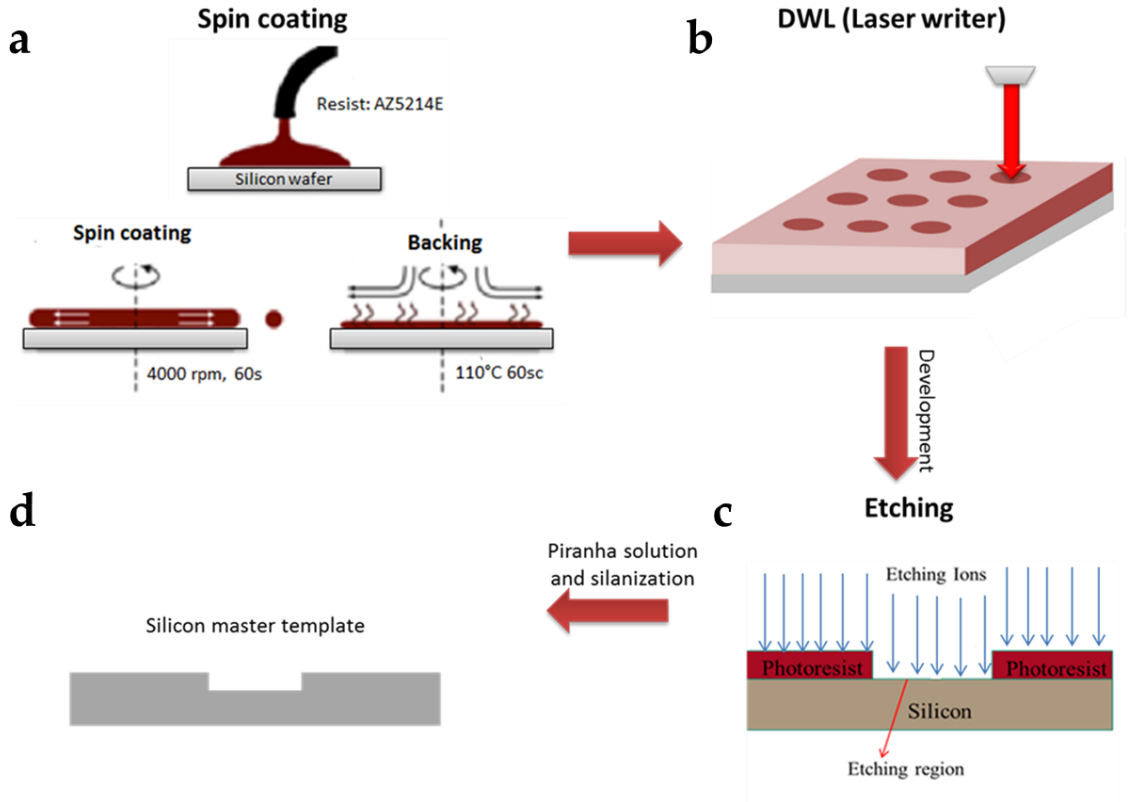

Figure 3. The four main steps of the silicon master template fabrication: *(a) spin coating, (b) laser writing, (c) deep reactive ion etching and (d) silanisation.*

The first step is related to the use of the Direct Writer Lithographic (DLW) technique to fabricate a silicon master template presenting an array of holes with circular, elliptical, and quadrangular base and fixed size. The geometrical pattern of the template was drawn using the LASI software. The drawing was converted from GDS format to HIMT format. An AZ5214E resist was written via a laser writer system at 405 nm (Heidelberg Instruments DWL66FS). The wafer (4 inches, doped P, 525 x 25 µm) was first washed through sonication in acetone and isopropanol. The primer and the resist were deposited over the silicon wafer by spin coating (Sawatec) using the following protocol: 10 sec at 500 rpm and 60 sec at 4,000

rpm, resulting in a final thickness of about 1.4 µm (fig. 3a). This coating was baked on a hot plate at 110 °C for 1 min. Then, with the instrument Heidelberg Direct Writer Lithography, an exposure job was set up with a defocusing value of 1,700 nm and laser intensity of 0.75 mWatt (fig. 3b). The substrate was developed with AZ726 developer for 4 min. The pattern was transferred to the underlying silicon substrate by deep reactive ion etching with SF6/O2 plasma for 60 sec (Sentech SI500 Instrument GmbH RIE) (fig. 3c). The resist was removed in a piranha solution (sulfuric acid and hydroxide peroxide (3:1)) for 5 min. The Silicon Template was sinalised to avoid interaction between the silicon template structured and silicone materials such as PDMS. An oxygen plasma (pressure 0.5 mBar, stabilization 15 sec, time 1 min, Oxygen (%) 100, frequency 100 W) was made on the silicon master template followed by silanization with 125µl of CF3(CF2)5(CH2)2SiCl3 for 1 hour under reduce pressure (fig. 3d). The resulting silicon master template was imaged with Scanning Electron Microscopy (Helios Nanolab 650 Dual Beam, Fei company).

1.1.2. PDMS and PVA sacrificial templates

Once the silicon master template was obtained, the following step requires the realization of a polydimethylsiloxane (PDMS) replica. The silicon master template was fixed on a Petri dish (d=10 cm). A solution of PDMS and curing agent (10:1) was cast over the Si wafer. The mixture was then polymerized at 60° for 3 h. This resulted in a second template, presenting cylindrical pillars on his configuration (fig. 4.2 left). This process was repeated seven times to generate seven PDMS templates. The templates were fixed into a petri dish (d=15 cm) and covered with ~30 mg of PDMS (10:1) to form a unique structure with the size of a Petri dish.

The final step required the realization of a sacrificial template of poly(vinyl) alcohol (PVA). A 5% PVA solution was deposited over the PDMS replica template. Was left to dry in an oven for 3h at 60°C, the PVA solution became a thin film. Upon complete drying and was peeled off the PDMS template (fig. 4.2 right). This template presented circular wells, just like the original master Si template (fig. 4.2 middle).

1.1.3. DPNs Fabrication

For the synthesis of soft DPNs (s-DPNs), 30 mg of poly(lactic-co-glycolic acid) (PLGA) were dissolved in chloroform (CHCl3) and mixed with 6 mg of polyethylene glycol (PEG) diacrylate and 10 µg of 2-Hydroxy-40-(2-hydroxyethoxy)-2-methylpropiophenone (photoinitiator). For rigid DPN (r-DPNs) synthesis, 90 mg of PLGA was dissolved in CHCl3 with the same co-constituents described above. Instead, for rigid rigid DPN (rr-DPNs)

synthesis was always used a tripled PLGA concentration but removing PEG and Photo-initiator. 30 µg of DSP-CY5 or Lipid rhodamine B (Avanti Polar Lipids, USA) was also added for providing proper fluorescent optical contrast. The resulting polymeric paste was carefully deposited in the wells of the sacrificial PVA template (fig. 4.3 left) and exposed to UV-light for polymerization (fig. 4.3 middle). The resulting PVA film, loaded with the above polymeric paste, was immersed in water and left to stir for 3h. This step led to the dissolution of the PVA and the release of DPNs in the aqueous solution (fig. 4.3 right). DPNs were eventually collected via centrifugation and membrane filtration to remove residual fragments of PVA.

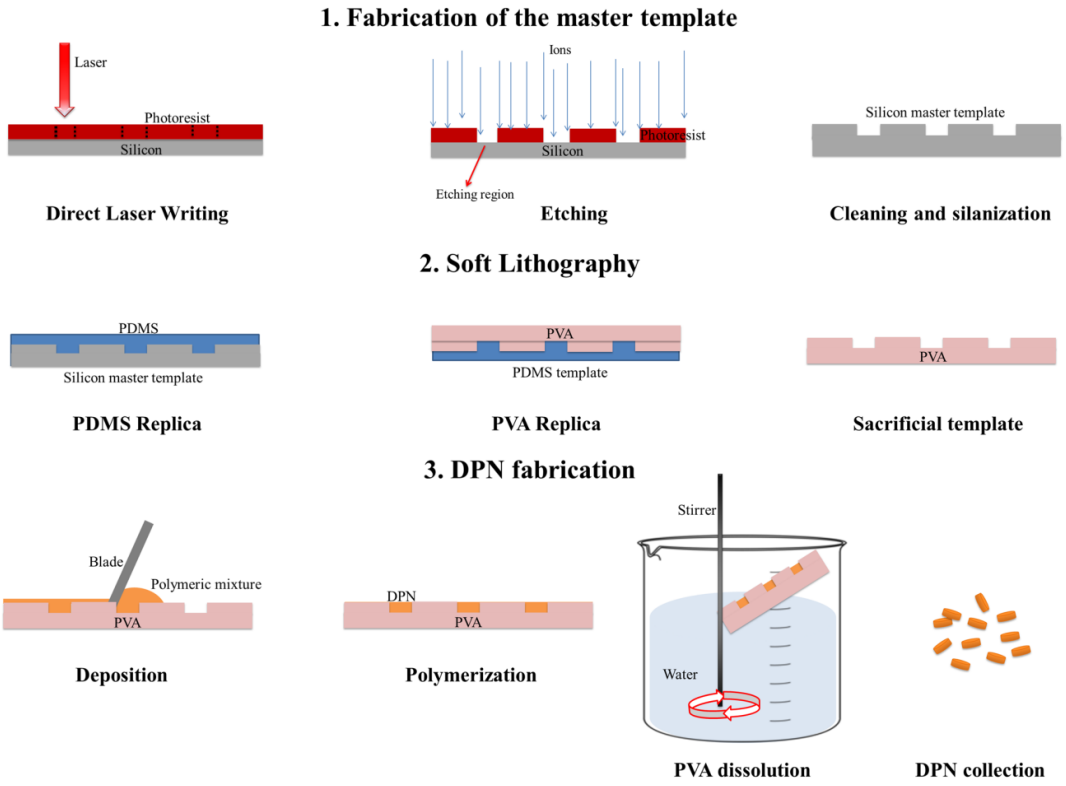

Figure 4. DPNs Fabrication steps. *1) Realization of a silicon master template; 2) Soft Lithography (PDMS and PVA replication); 3) DPN fabrication (loading of the PLGA/PEG mixture, polymerization, sacrificial template dissolution and DPN collection).*

1.1.4. DPNs loading

Two loading protocols were developed, namely, direct and absorption loading. In "direct loading", the imaging and/or therapeutic agents of interest were dispersed within the original polymeric paste and directly distributed in the wells of the PVA template. In "absorption loading", the collected DPNs were lyophilized to form a powder. This was eventually

dispersed in an aqueous solution carrying the imaging and/or therapeutic agents of interest. Re-hydration led to the rapid absorption of the molecules within the hydrogel structure of DPNs. The concentration of DPNs, imaging agents, and therapeutic molecules, the volume of the aqueous solution was systematically varied to identify optimal loading conditions.

1.1.5. DPNs Characterization

The size and shape characterization was done on all silicon master templates, PDMS replicas and the particles from the four different DPN configurations by Scanning Electron Microscope Helios Nanolab 650. Ultra-high resolution SEM images were acquired at high vacuum conditions after 10 nm aurum coating using a Q150T ES sputter-coater (Quorum). 5 ~ 25 keV of beam energies and corresponding electron currents of 0.98 pA ~ 0.14 nA were used. In all cases, the mode 2 configuration was used.

DPNs still embedded within the PVA templates were observed using an A1+ confocal microscope (Nikon-A1, Nikon corporation Japan) equipped with 63X lens working in oil immersion (an additive 1.5X optical magnification was applied). Lipid rhodamine B (Avanti Polar Lipids, USA) was used in the fabrication step to allow particle visualization.

DPN concentration and size distribution profiles were performed through a multisizer (Beckman Coulter, USA). The ζ-potential was calculated using DLS (Malvern, UK). Morphological analysis of DPNs was also determined by TEM (JEOL, Japan). TEM samples were prepared by the drop-casting method over a carbon-coated grid, were sputtered with 10 nm of carbon and analyzed operating at an acceleration voltage of 100 kV. The DPNs solution was placed and dried on a carbon-copper grid, and was carbon coated with 10-20 nm before Transmission Electron Microscope imaging (JEOL JEM 1011 TEM working at 100KV).

1.1.6. AFM Young Modulus/stiffness analysis

The mechanical properties of DPNs were tested using a Nanowizard III AFM system (JPK Instruments, Germany), mounted on an AxioObserver D1 (Zeiss, Germany). Silicon nitride triangular cantilever (DNP, Bruker, USA), with a nominal spring constant of 0.06 N/m, was employed. The typical radius of curvature of the tip was 20 nm. The actual spring constant was determined in situ for each cantilever using the thermal noise method (Hutter & Bechhoefer, 1993). QI Advanced software module was included in the setup. QI data set were acquired in milliQ water, by applying maximum forces load between 1 nN and 2 nN. Force-

distance (FD) curves length was maintained constant for each data collection, ranging from 0.5 µm to 1 µm, the tip was always moved at a constant velocity of 17 µm/s.

FD curves were analyzed by using the JPK Data Processing software (JPK Instruments, Germany). Each FD curve of the QI map was converted into force-indentation (FI) curve and fitted with the Hertz model, by using a Poisson's ratio of 0.5. The AFM tip was approximated as a quadratic pyramid indenter.

Three different polymeric paste compositions were prepared to produce: soft DPN (sDPN), rigid DPN (rDPN) and rigid rigid DPN (rrDPN). In particular, the preparation of the polymer paste for the sDPN, rDPN and rrDPN synthesis has been described in the section 2.3 DPNs Fabrication. 10 µL sDPN, rDPN, rrDPN colloids (1000 nm of diameter × 400 nm of thickness discs with a circular base) were deposited on Poly-L-Lysine coated glass substrates (HistoBond + 76 x 26 x1 mm; Marienfeld). The sample was dried at room temperature and subsequently rehydrated in milliQ water, for at least 3 h prior the AFM data acquisition. Atomic force microscope and the Young's modulus was calculated by analyzing the resulting force-displacement curves.

1.1.7. Prodrugs synthesis

Conjugating lipid chains - Cyanine-5 (DSPE-Cyanine-5), DSPE-Cy5-A, and DSPE-Cy5-B (near-infrared imaging agents Cy5.5) were synthesized as reported by Lee and coworkers with some modifications (95). 15 mg of DSPE-NH2 were dissolved in 3 mL of dichloromethane (DCM) and 1.5 mL of MeOH. 0.98 eq of Cyanine-5 NHS ester was dissolved in 200 ml of dimethylformamide (DMF) and added to the previous solution. A catalytic amount of triethylamine (TEA) was added to the reaction and left to stir for 16 hours. The resulting product was precipitated with cold diethyl ether, then washed 3 times with cold diethyl ether obtaining the final compound with a yield of 90%.

DSPE-Methotrexate. 15 mg of DSPE-NH2 were dissolved in 3 mL of dichloromethane (DCM) and 1.5 mL of MeOH. 0.98 eq of Methotrexate ester was dissolved in 200 ml of dimethylformamide (DMF) and added to the previous solution. A catalytic amount of triethylamine (TEA) was added to the reaction and was left to stir for 16 hours. The intended product was precipitated with cold diethyl ether, then washed 3 times with cold diethyl ether getting the final product with a yield of 90%.

PEG-Methotrexate. 20 mg of PEG-NH2 (1,000 Da) were dissolved in 3 mL of dichloromethane (DCM) and 1.5 mL of MeOH. 0.98 eq of Methotrexate was dissolved in 200 ml of dimethylformamide (DMF) and added to the previous solution. A catalytic amount of triethylamine (TEA) was added to the reaction and was left to stir for 16 hours. The intended product was precipitated with cold diethyl ether, then washed 3 times with cold diethyl ether getting the final product with a yield of 90%.

Linoleic acid-doxorubicin. LA-Dox was synthesized as reported by Fernandes and coworkers with some modifications (96). Briefly, an aqueous solution of Doxorubicin hydrochloride (5 mg/mL) was neutralized with a solution of sodium bicarbonate solution (50 mg/mL). A linoleic acid solution (50 mg/mL) in ethanol was incubated with EDC/NHS (molar ratio of 3:1) for 1 h under magnetic rotation at room temperature. The obtained solution was added drop by drop to the above mixture while stirring. After 12h, the mixture was centrifuged (12,7000 rpm, 30 min). The red pellet was washed with distilled water three times, removing the unreacted water-soluble Doxorubicin. Finally, the red pellet was collected and dried under vacuum.

DSPE-doxorubicin. An aqueous solution of Doxorubicin hydrochloride (5 mg/mL) was neutralized with a solution of sodium bicarbonate solution (50 mg/mL). A DSPE-succinic-acid (50 mg/mL) in ethanol was incubated with EDC/NHS (molar ratio of 3:1) for 1 h under magnetic rotation at room temperature. The obtained solution was added drop by drop to the above mixture while stirring. After 12h, the mixture was centrifuged (12,7000 rpm, 30 min). The red pellet was washed with distilled water three times, removing the unreacted water-soluble Doxorubicin. Finally, the red pellet was collected and dried under vacuum.

1.1.8. Loading and release studies

To calculate the amount of drug inside DNPs, samples were lyophilized and dissolved in acetonitrile (ACN). All samples were analyzed by HPLC at 240 nm UV absorbance (Agilent 1260 Infinity, Germany). The encapsulation efficiency was defined as the percentage weight ratio between the drug amount loaded inside DPNs at the end of their preparation and the initial input amount of the drug. For the release studies, 200 μL of DPN solution was poured into Slide-A-Lyzer MINI dialysis microtube with a molecular cut off of 10 kDa (Thermo Scientific) and dialyzed against 4L of H2O at 37 °C. For each time point, in triplicate, DPNs were collected and destroyed with ACN to release the molecule of interest. Samples were

analyze depending on an HPLC (Agilent 1260 Infinity, Germany) at 340 nm UV absorbance for MTX prodrugs, and 490 nm and 646 for LA-Dox and Cy5 respectively.

1.1.9. Cell culture and viability

The human Triple Negative Breast Cancer MDA-MB231 cell line was obtained from the American Type Culture Collection (ATCC). Cells were cultured in Eagle's minimal essential medium (EMEM) (ATCC,USA) containing 10% FBS (Gibco, Thermo Fisher Scientific, USA), 1% penicillin/streptomycin (Sigma-Aldrich, USA), under a humid atmosphere (37°C, 5% CO2, 95% air). Upon reaching appropriate confluence, cells were passed. Cell viability was determined via an MTT assay, which detects the reduction of MTT (3-(4,5-dimethylthiazolyl)-2,5-diphenyltetrazolium bromide) (Sigma-Aldrich, USA) by mitochondrial dehydrogenase to blue formazan product. This reflects the normal function of mitochondria and, hence, the measurement of cytotoxicity and cell viability. Briefly, 2x105 cells/well were seeded in 96-well plates and incubated at 37°C, 5% CO2, for 24 h. Next, the medium was replaced with EMEM containing the corresponding concentrations of Doxorubicin (DOX), doxorubicin pro-drug (LA-DOX, DSPE-DOX, (LA-DOX) DPNs and (DSPE-DOX) DPNs) (0.1-50 μM), Methotrexate (MTX), PEG-MTX and DSPE-MTX (0-100 μM)) and (DSPE-MTX) DPNs (0.01-0.5 μM). After 24h, 48h, 72h, and 96h of incubation, the MTT solution (5.0 mg/mL PBS) was added to each well and incubated at 37°C for 4h. The resulting formazan crystals were dissolved by adding ethanol (200 μL/ well), and the absorbance was read at 570 nm using a microplate reader (Tecan, CH). Controls (i.e.: cells that had received no drug) were normalized to 100% and readings from treated cells were expressed as percentage of viability inhibition. Five replicates were considered for each data point.

2. Results

2.1. Silicon master template fabrication

A versatile fabrication strategy was used to realize polymeric nanoconstructs with controlled geometrical and mechanical features, including the size, shape, surface properties, and mechanical stiffness – the 4S parameters. These features can be independently tuned in the fabrication process to affect the therapeutic and imaging performances, as shown. (94). The silicon template appears as a matrix of wells reproducing the geometry of DPNs (fig. 7a). These wells represent the intended size and geometry of the desired nanoconstructs (fig. 8 a, b, c and d left and middle insets).

In this work, we report the production of four different types of particles coming from a carefully optimization and improvement of the nanofabrication process. The precise geometry of the single particle derives from different silicon master templates obtained by laser writer and electron beam lithography. In particular, at first, the optimal resist was chosen, then we focused on the spin coating parameters, but the bulk of the work was done on the pattern design, the laser dose/defocus and the following silicon etching process. Generally, the laser writing lithography, since it can only work in proximity and not in contact, is used to direct writing and perform optical lithography masks with structures ranging from 5 µm to 10 mm. The dimensions of our structures are located into the resolution limits of the machine, so in our case, it is a delicate process susceptible to problems that will decrease the yielding and reproducibility. In fact, one of the most important goals achieved in this project was the fine calibration of the machine parameters and the pattern design according to the laser proximity diffraction limits.

A pattern of wells has been designed on the silicon wafer in order to optimize the spaces and, therefore, the waste of material during the various phases of particle production. The gaps between the structures were at the machine's resolution limit and the number of structures designed was such as to cover the entire silicon wafer.

The AZ 5214 E resist was chosen due to its excellent covering property during the ions etching process and its easy removal from the silicon wafer.

The first problem identified was the optimization of the resist depth. In particular, if the obtained resist thickness was not optimal, the developer could not develop to the bottom of

the patterned wells, causing the shielding of silicon etching. In fact, the first objective was to find the right spin coating parameters to obtain a useful resist depth. Different spin coating speeds combined with different development times, and different concentrations of the developer were evaluated until reaching an optimal combination.

Moreover, often during the development, the main issue was the detachment of the resist from the silicon wafer. This was solved by a preliminary primer deposition that prevented the detachment of the resist after development.

In addition, the identification of the optimum defocus point for a certain resist thickness was crucial. An incorrect laser focusing often gives optical aberrations. Consequently, a correct defocus is a critical point of the reproducibility. A meticulous statistical work was done on this parameter in combination with different laser power doses. Indeed, the laser potency dose was another fundamental parameter for the technique reproducibility. Several power dose matrixes were made to define the useful laser potency. In particular, figure 5 shows an example of a laser matrix dose of 30%, 40% and 50% (at the fixed grey filter S30/10) combined with nominal diameters (drawn by LASI) of 800 nm, 900 nm and 1000 nm.

a

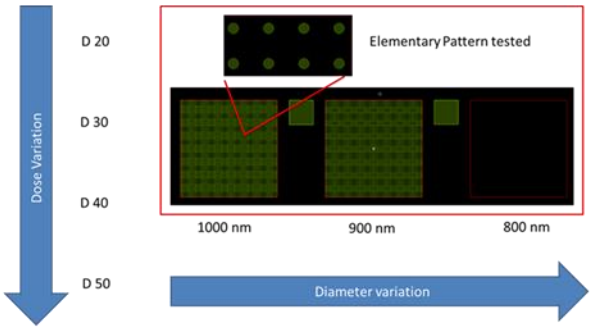

b

Dose %	count	D_n (um)	D (um)	SD
30	10	0,8	0,83	0,06
30	10	0,9	1,05	0,07
30	10	1	1,12	0,1
40	10	0,8	1,2	0,03
40	10	0,9	1,39	0,02
40	10	1	1,56	0,03
50	10	0,8	1,42	0,03
50	10	0,9	1,59	0,01
50	10	1	1,71	0,02

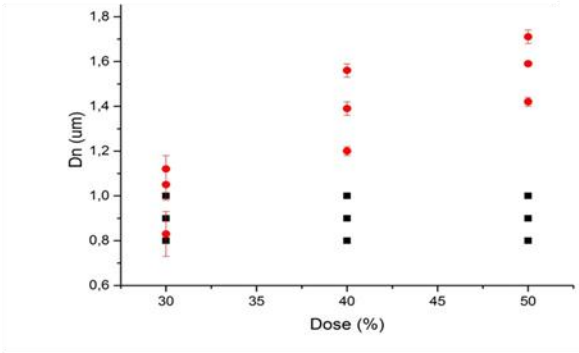

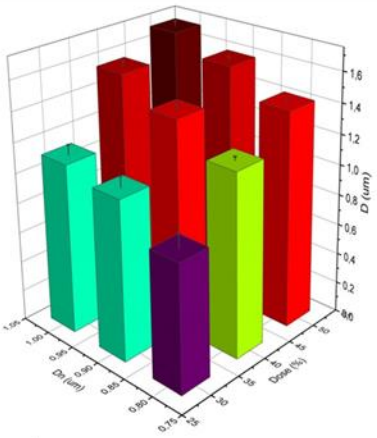

c

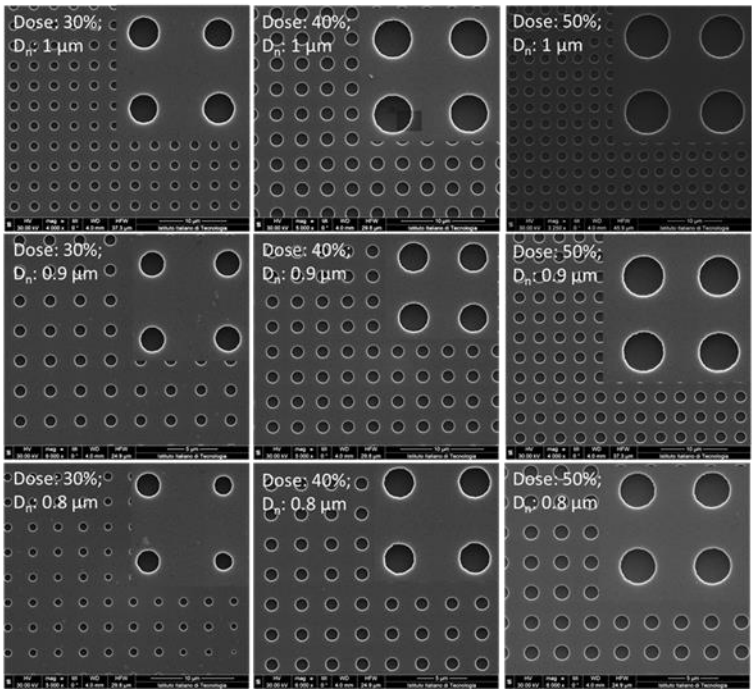

Figure 5. Laser writer dose power matrix at three different wells nominal diameter (800 nm, 900 nm and 1000 nm). *(a) experimental plan, (b) actual diameter at 30%, 40% and 50% of laser dose vs nominal diameter and (c) SEM images from patterned silicon templates obtained into the dose matrix.*

In figure 5a shows the detail experimental plan of the test, while in figure 5b, the two graphs and the table shows the variation of the diameter of the wells in function of the applied dose. Figure 5c is reported the SEM images of the 9 patterns obtained. It is possible to observe from the data that the nominal diameter at 900 nm combined with the doses 40-50% gives greater size homogeneity an actual wells diameter closer to 1000 nm. In the previous works of the group, this was seen as the optimal size of the DPN to adhere to the endothelial tight junctions.

In figure 6 are reported the SEM images coming from the laser defocus optimization process. Results show that the combination of 50% of the laser dose with a defocus of 1800-1700 was able to create a more homogenous template, with holes with a diameter closer to 1000 nm.

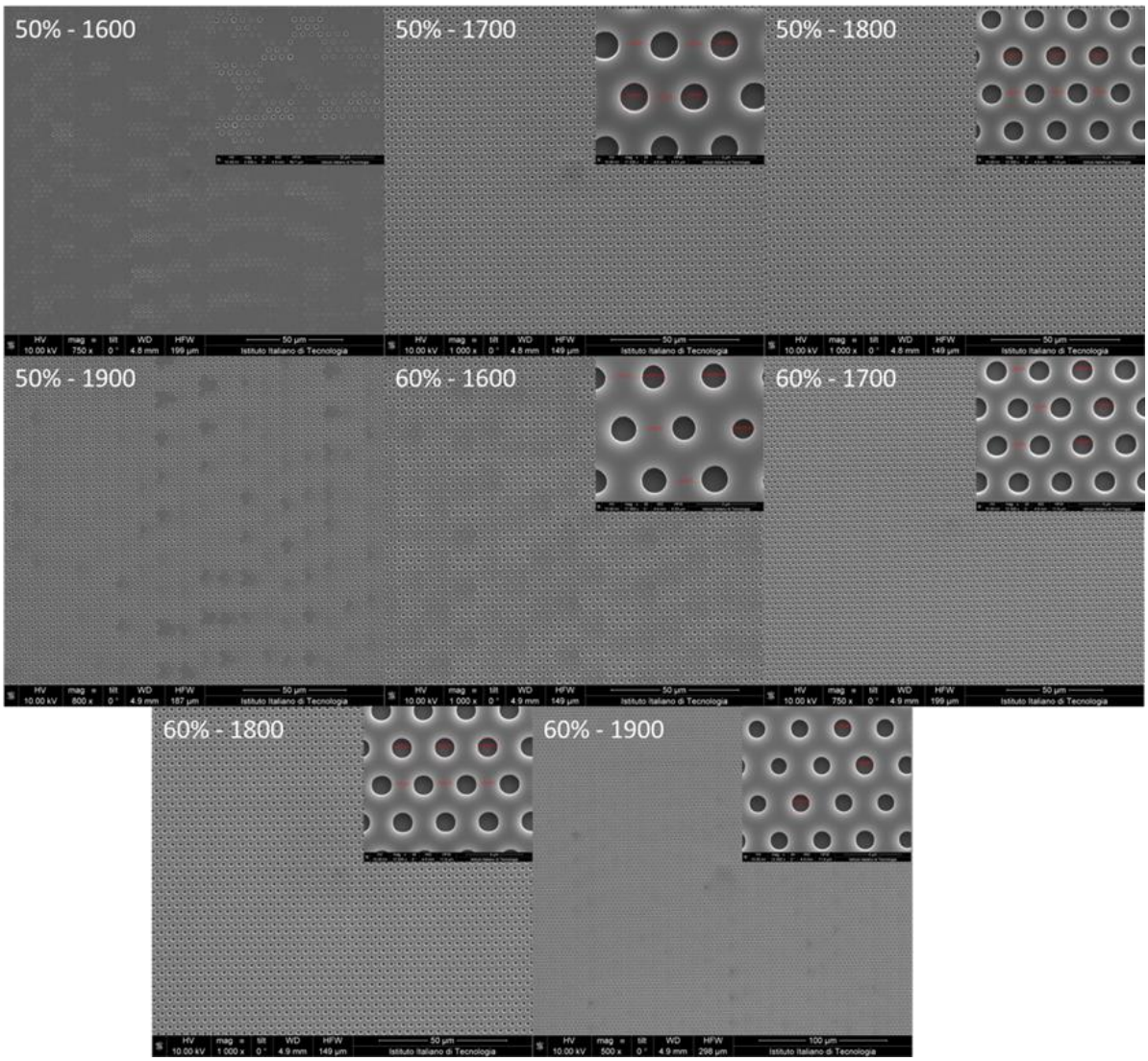

Figure 6. SEM images from the patterned silicon templates obtained into the Dose/ Defocus matrix test.

This type of calibration was performed for the four nanoconstructs configuration shown.

This meticulous optimization work led to an increase in the size of the silicon master template and in an increment of the number of wells reproduced per template. This led to an increased particle yielding production of 40 times for the same number of templates.

Besides that, this work showed for the first time the possibility to use the DLW lithographic technique to fabricate a silicon master template presenting such a large array of discoidal wells with circular, elliptical, and quadrangular base and fixed size within the limits of resolution.

2.2. DPNs Production

In fact, the silicon master template is used as a mold to realize a PDMS replica. The PDMS replica exhibits arrays of pillars with the same geometry of the wells in the silicon template (figure. 4.2). Finally, a sacrificial PVA template is obtained by replicating the PDMS template. DPNs are made out of a mixture of poly(lactic-co-glycolic acid) (PLGA), polyethylene glycol diacrylate (PEG-DA), photoinitiator (PI), and the therapeutic or imaging agent of interest. For the preparation of DPNs, the polymer mixture of PLGA, PEG-DA, and PI is directly applied and spread over the PVA template to fill the multiple wells (Figure. 4.3). This loaded template is then exposed to UV-light for the polymerization of PEG-DA chains. The resulted PVA templates spread with the polymeric mixture are shown in figure 7c by confocal images. Eventually, the PVA film is immersed in an aqueous solution and dissolved after stirring (Figure 4.3) to release the DPNs. The final steps, including centrifugation and filtration, are used to remove residual PVA fragments. Figure 7c presents confocal fluorescent images of a PVA template loaded with a mixture of PLGA/PEG and Lipid Rhodamine (LP-Rhod). A uniform distribution of ‘red dots’ within the structure can be appreciated. These ‘red dots’ correspond to the DPNs before the dissolution of the PVA template and are loaded quite uniformly with LP-Rhod, returning the reddish color.

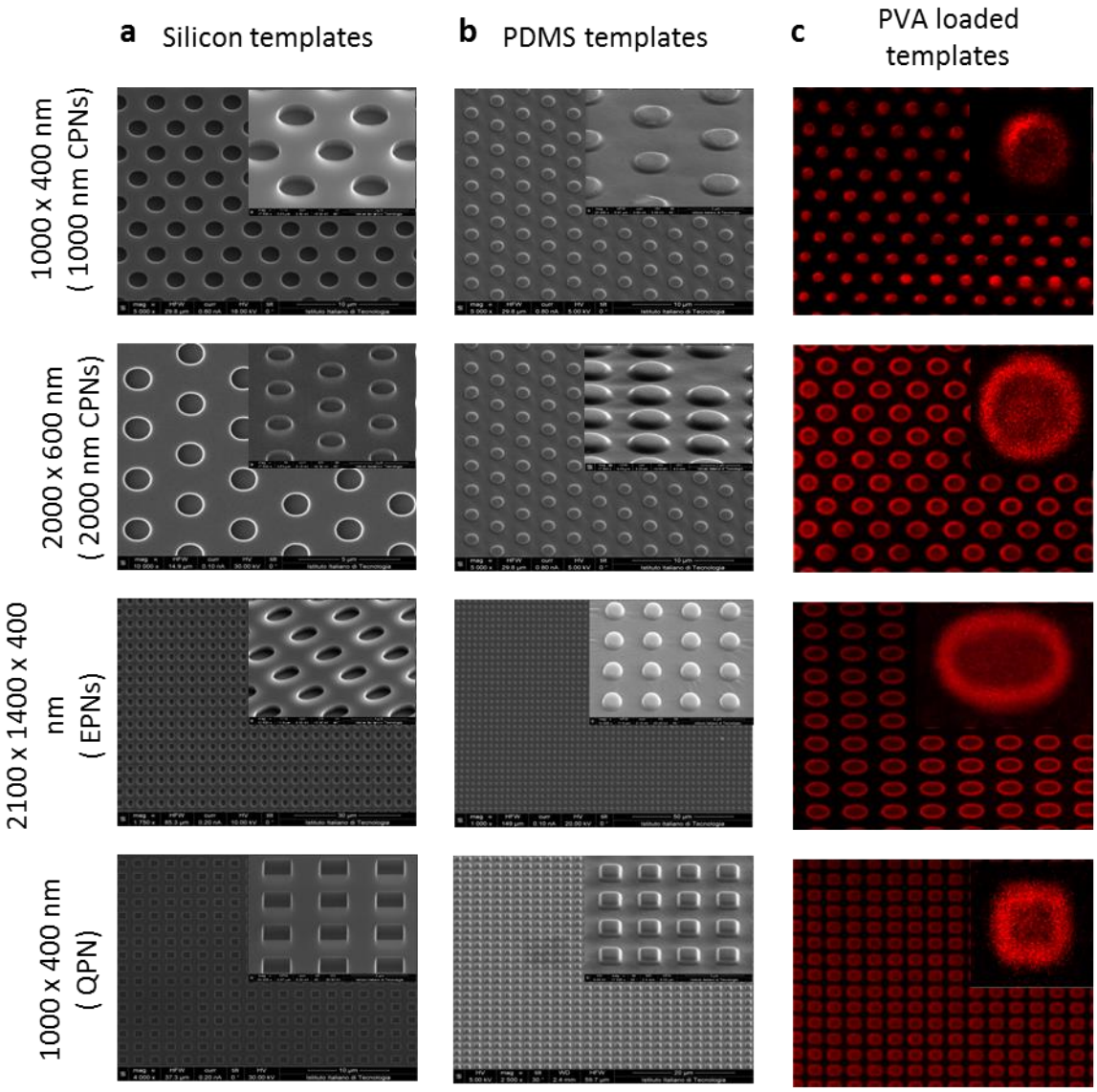

Figure 7. *a) SEM images of the silicon templates; b) SEM images of the PDMS templates; c) Confocal microscopy images of the PLGA/PEG mix-loaded into PVA templates.*

Table 1. Dimensions of circular 1000 x 400 nm CPN, circular 2000 x 600 nm CPN, elliptical EPN and squared QPN silicon master templates.

	1000 x 400 CPN	**2000 x 600 CPN**	**EPN**	**QPN**
Dimensions (nm)	Diameter 1340,3 ± 18,6 Thickness 439,14 ± 30,5	Diameter 1945,7 ± 19,2 Thickness 610,97 ± 33,2	Minor axis 1374,87 ± 18,6 Minor axis 2156 ± 19,5 Thickness 425,14 ± 20,4	Side 1035 ± 32,2 Thickness 605,02 ± 26,2

2.3. Physico-chemical characterization of DPNs

In this work, it is reported the production of four different types of nanoconstructs and each phase of the fabrication process has been thoroughly monitored. The figure 7a shows the silicon templates that are currently in use to obtain the four nanoconstructs configurations; in the upper right is displayed a zoom of the tilted wells into the pattern. The figure 7b shows the SEM images from the PDMS replicas, in the upper right a zoom of the tilted wells is also displayed; figure 7c reports the confocal images from the PVA templates loaded with the polymeric mixture in the four different configurations. On the different templates a careful statistical analysis of the dimensions was made which reported a good size homogeneity. In particular, the electron microscopy images show the actual geometry of DPNs that exhibits: an average diameter of 1,250 ± 19.36 nm and a height of 469.14 ± 27.5 nm for the 1000 x 400 nm circular DPN (1000 nm CPN – fig. 7a); an average diameter of 1945,7 ± 19,24 nm and a height of 610,97 ± 33,21 for the 2000 x 600 nm circular DPN (2000 CPN – fig. 7b); an average of major axis x minor axis of 1374,87 ± 18,6 x 2156 ± 19,5 nm and a height of 425,14 ± 20,4 nm for the 2100 x 1400 x 400 nm elliptical DPN (EPN – fig. 7c); an average side of 1035 ± 32,21 nm anda height of 605,02 ± 26,21 nm for the 1000 x 400 nm squared DPN (QPNs - fig. 7d). The precise dimensions of each template are shown in table 1. The analysis shows that for each intended nanoconstructs the structure produced in each silicon template presents similar size with variations lower than 1%.

The precise geometry of each single particle coming from different templates was also monitored and analyzed. On figure 8, is displayed a close up by Confocal Microscopy where the side top view and side view of nanoconstructs; a 3D model reconstruction by Confocal Microscopy and a TEM tilted image for 1 µm circular shape nanoconstructs (8a); 2 µm circular shape nanoconstructs (8b); elliptical shape nanoconstructs (8c) and square shape nanoconstructs (8d). The TEM images of individual DPNs presented in Figure 8 offer details of the nanoconstruct edges, demonstrating the precise replica of the original template geometry.

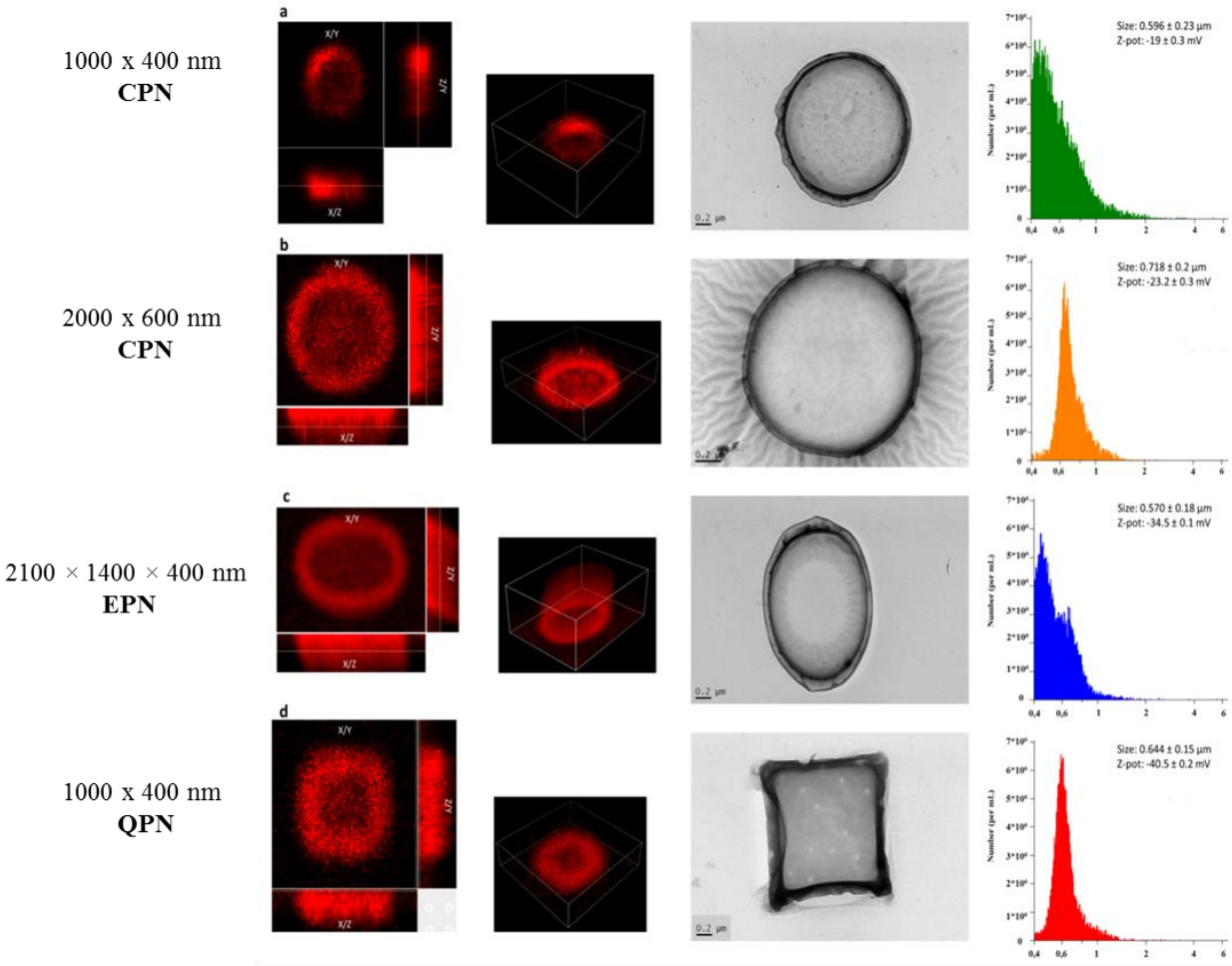

Figure 8. *Confocal Microscopy images of DPNs showing top, lateral and 3D reconstructed views (left); TEM tilted images of DPNs (center); Size spectrum as derived by a multisizer coulter counter analysis and characteristic surface electrostatic by dynamic light scattering analyses (right inset) for CPN 1000 nm (a), circular CPN 2000 nm (b), elliptical EPN (c), and squared QPN (d).*

The DPN concentration and size distribution profiles were performed through a multisizer and the ζ-potential was calculated using DLS (fig. 8 right inset). The analysis with the multisizer allowed us to quantify precisely the number of nanoconstructs as well as returning a characteristic size for the differently shaped DPNs. Note that, given the nonspherical shape of DPNs, a size distribution was returned with a sharp peak, which represents the characteristic geometrical dimension of DPNs for that instrument. This is a very powerful tool to assess the quality and reproducibility of the nanoconstruct geometrical features and for precisely counting the particles. Similar observations can also be extended to the DLS profiles. The characteristic size, resulting from the multisizer and DL machines, is summarized in figure 8 right inset together with the ζ-potential measurements.

2.4. Mechanical Characterization of Discoidal Polymeric Nanoconstructs.

Atomic force microscopy (AFM) analysis was used to determine the morphological and mechanical properties of DPNs (Figure 9).

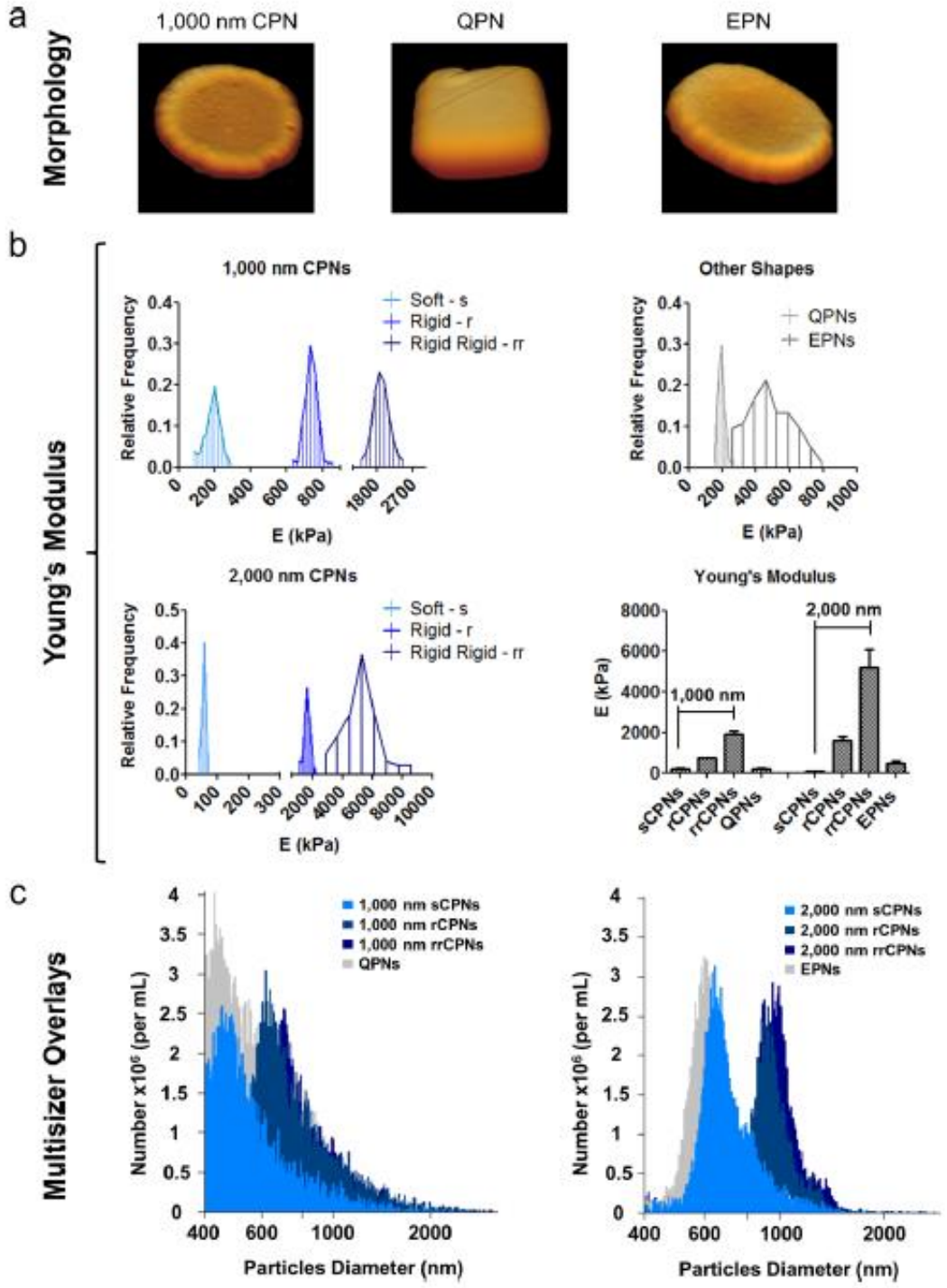

Figure 9. *Mechanical characterization of discoidal polymeric nanoconstructs. (a) Morphological analysis via atomic force microscopy documenting the size and shape of CPN, QPN, and EPN. (b) Distribution for the Young's modulus for the four DPN geometries (1000 and 2000 nm CPNs, QPNs, and EPNs). A direct comparison of the Young's modulus is provided in the summarizing bar chart in terms of mean ± SD. (c) Size spectrum of DPNs with different levels of softness as derived by a multisizer coulter counter analysis.*

A variation on the stiffness of the nanoconstructs was obtained, changing the composition of the polymeric matrix. An AFM analysis of Young Modulus and stiffness was performed on the polymeric nanoconstructs and on the film from which the different types of particles arise. The films were synthesized with the polymer proportions shown in paragraph 2.6. AFM Young Modulus/stiffness analysis of the Methodologies section, while the geometry of DPNs properly resembles that of the original silicon templates (fig. 7a). The DPN morphology was assessed using an AFM quantitative imaging mode under wet conditions. Figure 9a shows the size and shape of 1000 × 400 nm circular CPNs, 1000 × 400 nm square QPNs, and 2100 × 1400 × 400 nm elliptical EPNs. Still using atomic force microscopy, the Young's modulus of DPNs was estimated directly from multiple (>100) force−displacement curves, generated on over 10 particles per experimental group. In particular, the histograms in Figure 9b report the Young's modulus distributions for three differently shaped DPNs (1000 nm CPNs, QPNs, and EPNs) and DPNs with different mechanical properties (soft, sCPNs; rigid, rCPNs; and rigid−rigid, rrCPNs). The Young's modulus was E = 185 ± 35 kPa for the 1000 nm sCPNs, 195 ± 16 kPa for the 1000 nm QPNs, 56 ± 6 kPa for the 2000 nm sCPNs, and 476 ± 110 kPa for EPNs. Therefore, regardless of the size and shape, all soft DPNs returned a Young's modulus close to ∼100 kPa. Only EPNs present a slightly larger Young's modulus, which might be associated with its elongated shape and different polymerization rates. As the percentage of PEG in the original polymeric paste reduces, DPNs became stiffer and the Young's modulus grew correspondingly. Therefore, for rigid DPNs, it follows E = 737 ± 28 kPa for the 1000 nm rCPNs and 1606 ± 177 kPa for the 2000 nm rCPNs; for rigid−rigid DPNs, it results in E = 1907 ± 162 kPa for the 1000 nm rrCPNs and 5172 ± 902 kPa for the 2000 nm rrCPNs. As summarized in the bar chart of Figure 9b, the Young's modulus grows steadily moving from soft to rigid and rigid−rigid DPNs, regardless of their size. Interestingly, the change in rigidity of DPNs is also reflected in size distribution measurements performed with the multisizer (Figure 9c). Note that, in this instrument, particles dispersed within an isotonic solution are forced to flow across a small 20 μm capillary where each single passage is counted as an event. Rigid and rigid−rigid DPNs present a smaller variation in size distribution exhibiting quite sharp peaks and less broad distributions as compared to soft DPNs. This could be related to the DPN deformability under flow, whereby softer particles would deform more and take different orientations in the flow thus leading to a broader size

distribution as compared to stiffer particles. Potentially, this could be used as a high-throughput approach to qualitatively assess the nanoconstruct deformability.

It should be pointed out that through a new versatile microfabrication method and fine characterization, the size, shape, and surface properties of nanoparticles have been modified. The effect of nanoparticle size, shape, and surface properties on cellular uptake has been extensively investigated for its basic science and translational implications. This systematic work was done in order to modulate recognition and subsequent internalization by phagocytic cells into the following work of the group (97). Recently, softness is emerging as a design parameter for modulating the interaction of nanoparticles with cells and the biological microenvironment. In fact, Palomba et al. (97) demonstrated, regardless of the size and shape, that softer nanoconstructs evade cellular uptake up to 5 times more efficiently, by bone-marrow-derived monocytes, as compared to rigid nanoconstructs. Soft circular and quadrangular nanoconstructs are equally uptaken by professional phagocytic cells (<15%); soft elliptical particles are more avidly internalized (<60%) possibly because of the larger size and elongated shape, whereas over 70% of rigid nanoconstructs of any shape and size are uptaken.

2.5. Loading therapeutic and imaging agents into DPNs

The dispersion of functional molecules, such as therapeutic and/or imaging agents, within the polymeric structure of DPNs (Figure 10A) was achieved following two different strategies: a "direct method", where the agent is dissolved in the organic solvent and directly mixed with the PLGA and PEG prior to deposition over the PVA template; an"absorption method", where the agent is dispersed in a higher concentrated water solution, which is then exposed to the lyophilized powder of DPNs. In direct loading, the agent needs to be soluble and stable in an organic solvent whereas, for the absorption method, the agent needs to be soluble in water without forming micellar structures at high concentrations. As such the different loading methods work with different functional agents. DSPE-CY5-A was the first compound to be loaded into DPNs (Figure 10B). The Cyanine5 (Cy5) has the advantage of easy detection via fluorescent imaging and can be used in vivo too as a fluorescent imaging probe. DSPE-CY5-A was synthesized by reacting 1,2-distearoyl-sn-glycero-3phosphoethanolamine-N-amino (DSPE-NH2) with Cy5 pre-activated with N-Hydroxysuccinimide (NHS) on the terminal carboxylic acid. The compound DSPE-CY5-A resulted in being less hydrophobic than the

free Cy5-A. A more hydrophobic Cy5, which lacks the sulfoxide groups, increased, even more, the hydrophobicity of the compound and was used to prepare DSPE-CY5-B (Figure 10B).

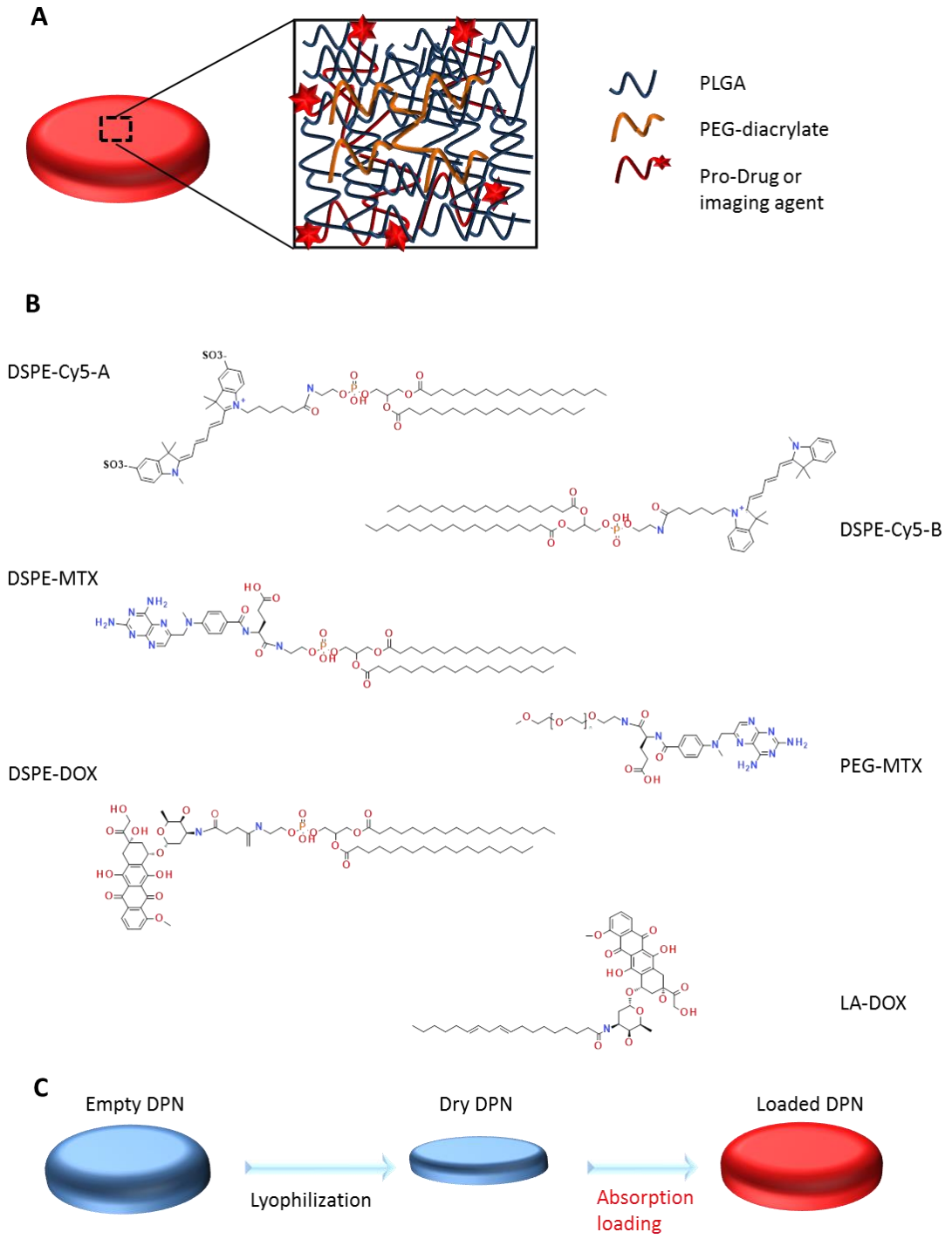

Figure 3

Figure 10. Schematic representation of Discoidal Polymeric Nanoconstructs and prodrugs. *A. Schematic representation of DPNs, highlighting their porous structure and entanglement of PLGA and PEG chains. B. Structural representation of the six synthesized pro-drugs. C. Schematic representation of the "absorption loading" method for the encapsulating prodrugs into DPNs.*

The same protocol was used for the synthesis. Then, methotrexate (MTX) was considered. This is a therapeutic molecule originally developed as an anticancer drug that also exhibits strong anti-inflammatory properties. A similar protocol, as per the Cy5, was used to prepare the prodrug DSPE-MTX (Figure 10B). MTX was pre-activated with a mixture of DCC and NHS, before conjugation with DSPE-NH2. With MTX, the hydrophobicity of the resulting compound was modulated by changing the lipid chain DSPE with PEG 1 kDa (Figure 10B), to increase the hydrophilicity of the resulting MTX prodrug. The synthesis protocol was the same as described above. Then, Doxorubicin (DOX) was also considered. This molecule was used for its red fluorescent signal as well as for its well-known cell cytotoxic activity. In this case, the protocol to generate the DOX prodrug was modified, in that DOX has no carboxylic acid group available, but rather an amine group. Therefore, first, the hydrochloride form of DOX was neutralized with a solution of sodium bicarbonate. Then, linoleic acid was pre-activated with EDC and NHS, and added to the solution.

Given the low water solubility of the resulting compound, it was collected via precipitation. The same procedure was used for the preparation of the DSPE-DOX (Figure 10B), replacing the linoleic acid with the DSPE-succinic acid. After preparing all these compounds and prodrugs, the loading steps were performed. "Direct loading" is the most straightforward procedure. The main requirement for the agent to be directly loaded is its solubility and stability in organic solvents, like dichloromethane (DCM), chloroform (CHCl3), or acetonitrile (ACN). The compound is directly mixed with the original polymeric past forming the DPNs and applied over the PVA template. A drawback of this straightforward loading procedure is the low encapsulation efficiency (EE), which is due to the yielding in the preparation of DPNs and the hydrophilicity-hydrophobicity ratio of the loaded agent.

As per the yielding, it should be noted that a portion of the loaded agent and polymeric paste are wasted during the deposition into the PVA wells. As per the hydrophilicity-hydrophobicity ratio, it should be noted that more hydrophilic compounds (lower LogP) tend to rapidly escape the DPN polymeric matrix during the purification and collection steps that occur in water. "Absorption loading" consists in exposing a concentrated aqueous solution of the agent to the initially lyophilized DPNs. During the rapid re-hydration phase, DPNs avidly recall, within their polymeric structure, water enriched with the molecules of the therapeutic/imaging agent. A fine balance between compound hydrophilicity and

hydrophobicity is required for this loading strategy. Note that, after absorption, the higher molecular-weight hydrophobic prodrugs would tend to stay more trapped within the core of the DPNs as compared to their free counterparts, thus limiting their interaction with the aqueous environment.

2.6. Optimizing the "absorption loading" into DPNs

Based on the above reasoning, the encapsulation efficiency (EE) into DPNs would vary for each prodrugs and loading strategy. In the "direct loading", EE can be optimized by improving the filling of the wells in the PVA template and limiting the losses of polymeric paste out of the wells. This optimization process is out of the scope of this work. As per the "absorption loading", three independent parameters can be systematically modified to modulate EE. These parameters are: the exposure time of the lyophilized DPNs to the aqueous solution (rehydration time); the mass of prodrug in the aqueous solution; the volume of the aqueous solution. For studying the influence of the rehydration time, lyophilized DPNs were exposed to a 20 µL concentrated solution of 1 mg/mL of DSPE-Cy5-B for 1, 3, 6 and 10 minutes. After exposure, water was added to the mixture followed by a centrifugation step to remove the non-absorbed DSPE-Cy5-B. This was quantified via UV-Vis spectroscopy. The results showed that Cy5 loading stayed around 75% and no variation with the exposure time was observed (Figure 11A, left column). Also, DPNs size and z-potential did not change during the process demonstrating no damage following the rehydration step (Figure 11A, right column). Based on this data, one minute of rehydration time was sufficient to load a significant amount ofDSPE-Cy5-B. "Absorption Loading" is also affected by the volume of the aqueous solution and the concentration of the therapeutic agent. Therefore, after fixing the volume of DSPE-Cy5-B solution (20 µL) and the exposure time (1 min), the agent concentration was reduced from 1 to 0.9, 0.75, 0.5, and 0.25 mg/mL. Even in this case, the compound concentration did not significantly affect the loaded amount of DSPE-Cy5-B, which stayed around 75% (Figure 11B, left column). A modest change in DPNS size was observed with a decreasing concentration of the compound (Figure 11B, right column). At low concentrations, DPNs acquired a larger size (860 nm, at 0.25 mg/ml) compared to the higher concentrations (720 nm at 1 mg/mL). This could be related to the intercalation of the compound within the DPN polymeric matrix that would pull it towards the core resulting in a slightly smaller and more compact structure. The last independent parameter to be analyzed was the volume of rehydration. In this case, the compound concentration (1 mg/ml of DSPE-Cy5-B) and the exposure time (1 min) were fixed, whereas the volume varied between 10, 20,

30, 50, 100 μL. Results show that with an increase of the volume, the loading of the DSPE-Cy5-B decreases (Figure 11C, left column). Indeed, lower volumes mean more DSPE-Cy5-B located in the vicinity of the DPN surface, thus leading to higher loading upon absorption. DPN size and z-potential were not affected by the volume variation (Figure 11C, right column).

Summing up, optimal loading via absorption can be realized by minimizing the rehydration volumes and maximizing the mass of the compound. Importantly, the compound should be sufficiently hydrophilic to be dispersed in water and moderately hydrophobic to stay within the DPN matrix upon exposure to the aqueous environment. Thus, for this loading strategy, it is crucial to realize prodrugs with the right hydrophilic-hydrophobic ratio and molecular weight. The bar chart in Figure 11D summarizes the results obtained in terms of EE for the different loading strategies and compounds. The DSPE-Cy5 A and B present high EE under the absorption loading strategy, reaching encapsulations as high as ~ 80%. Because of the DSPE derivation, these compounds are slightly less hydrophilic and have a larger molecular weight as compared to the original free probes (Cy5 A and B). These two features favor their loading into the DPNs during the absorption phase and limit their rapid release during the purification steps. This ideal combination of hydrophobicity/hydrophilicity ratio and the proper molecular weight is not achieved with the MTX prodrugs. The DSPE-MTX is significantly hydrophobic, with a LogP of 13.84, and cannot be efficiently resuspended in water returning an EE= 1.2%. On the other hand, the 1 kDa PEG-MTX has a LogP of -3.31, which allows efficient resuspension in water. However, the large molecular weight of the resulting compound opposes absorption during the DPN rehydration, thus returning a moderate EE of ~ 3. The beneficial effect of identifying the right hydrophobicity/hydrophilicity ratio is presented by the DOX case. LA-DOX is significantly hydrophobic with a LogP of 6.59. This leads to an EE of ~ 7, which, incidentally, is higher than that obtained for the more hydrophobic DSPE-MTX. Notably, DSPE-DOX has a LogP of - 14.42 returning an EE of ~ 40%. Figure 11D also shows how direct loading, in the current configuration, is far less efficient than absorption loading. This data confirms that the hydrophobicity/hydrophilicity ratio and molecular weight of the prodrug are critical features to optimize loading.

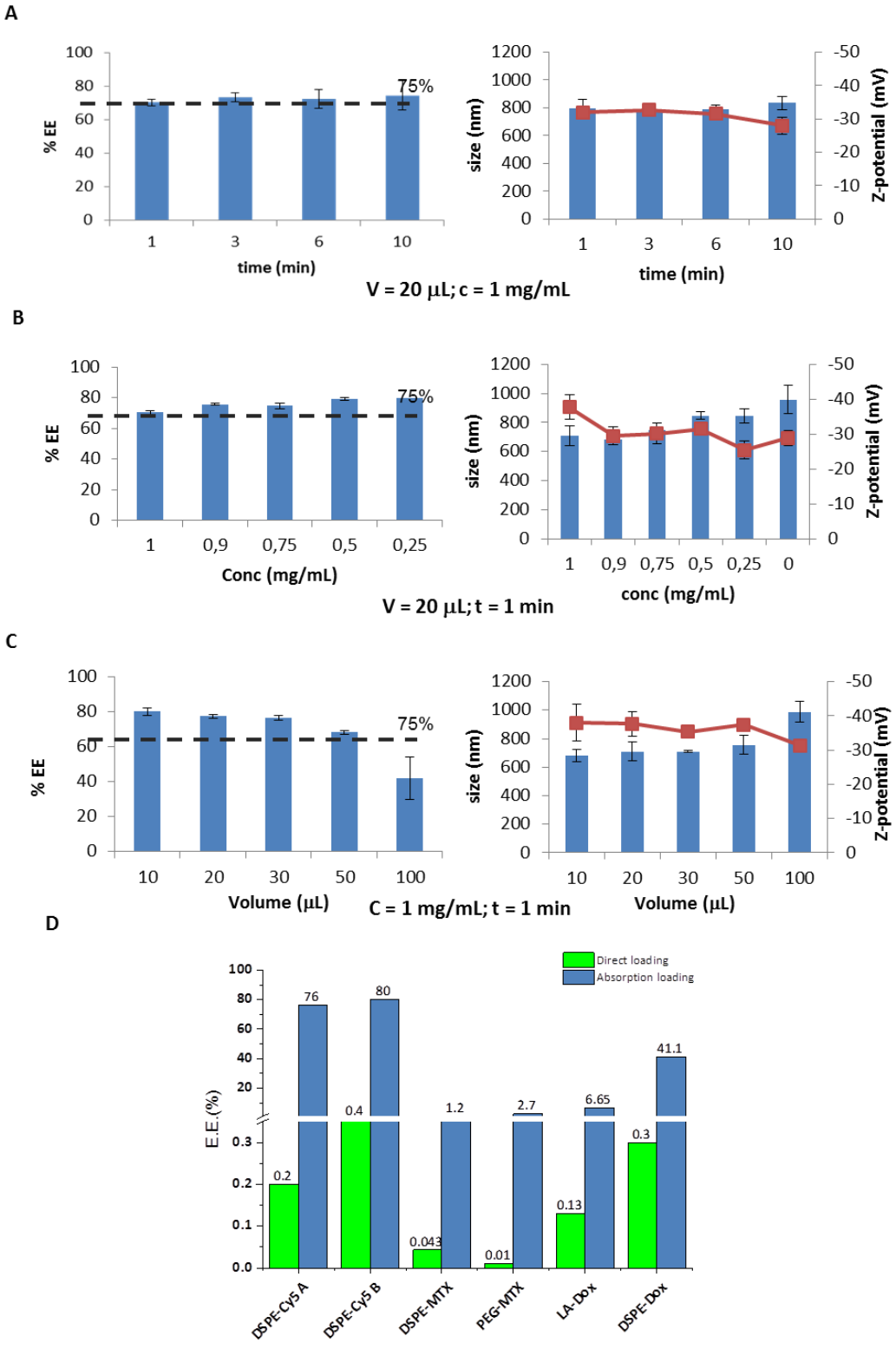

Figure 11 Optimization of Absorption Loading and Ecanpsulation Efficiency into Discoidal Polymeric Nanoconstructs. *Variation of the encapsulation efficiency and DPN size and z-potential with A. the rehydration time; B. the pro-drug mass; and C. the volume of the rehydration solution. D. Encapsulation efficiencies for the six different pro-drugs and two different loading methods ("direct method" and "absorption method").*

2.7. Release profile of prodrugs from DPNs

Release studies were conducted for all loaded prodrugs under the sink condition by exposing a known amount of DPNs to a 4 L aqueous solution. Starting with DSPE-Cy5-A (Figure 12A), an initial huge burst was observed over the first 10h with 70% and 60% of the agent released for the absorption and direct methods, respectively. At 72h, the DSPE-Cy5-A loaded via the absorption method was fully released out of DPNs as compared to a 90% release for the direct method. Indeed, the DSPE-Cy5-A suffers of a high water solubility, which would justify the observed rapid release profile. Moreover, in the absorption method, most of the DSPE-Cy5-A molecules are likely trapped near the DPN surface, which indeed facilitates their release in the surrounding aqueous environment. On the other hand, the direct loading of DSPE-Cy5-A favors its uniform distribution within the DPN polymeric matrix, thus slowing the release rate. A different behavior is observed for the more hydrophobic compound DSPE-Cy5-B (Figure 12B). Over the first 10h, only 35% and 12% of the loaded DSPE-Cy5-B are released out of DPNs for the absorption and direct methods, respectively. At 72h, these two values become 60% and 35%, respectively. The slower release of DSPE Cy5-B as compared to DSPE Cy5-A should be ascribed entirely to the different hydrophobic/hydrophilic ratio, which is in favor of the Cy5-B compound. Notably, the direct method is still characterized by a lower release rate, possibly because of the uniform distribution of the compound within the DPN polymer matrix. The release profiles for DSPE-MTX and PEG-MTX are presented in Figure 12C and Figure 12D, respectively. A different behavior is observed as compared to DSPE-Cy5 due to the different hydrophobicity. The release of DSPE-MTX was characterized by an initial burst over the first 6h with 50% of the drug being released for both loading methods. Interestingly, the release of DSPE-MTX was observed to plateau around 60% at about 24h. A similar observation applies for PEG-MTX but only for the direct method loading. For the absorption loaded PEG-MTX, the compound leaked out of the DPN matrix in a sustained fashion over the whole period of observation. Note that DSPE-MTX is the most hydrophobic compound realized in this work and, as such, prefers to stay associated within the PLGA/PEG matrix. This would explain the plateau observed in Figure 12C. Interestingly, the value of the plateau is similar for both direct loaded DSPE-MTX and 1kDa PEG-MTX, thus confirming the role of compound hydrophobicity. On the other hand, the absorption loaded 1kDa PEG-MTX, which is mostly confined to the DPN surface given its significant molecular weight, escapes the particle matrix just as DSPE-Cy5-B.

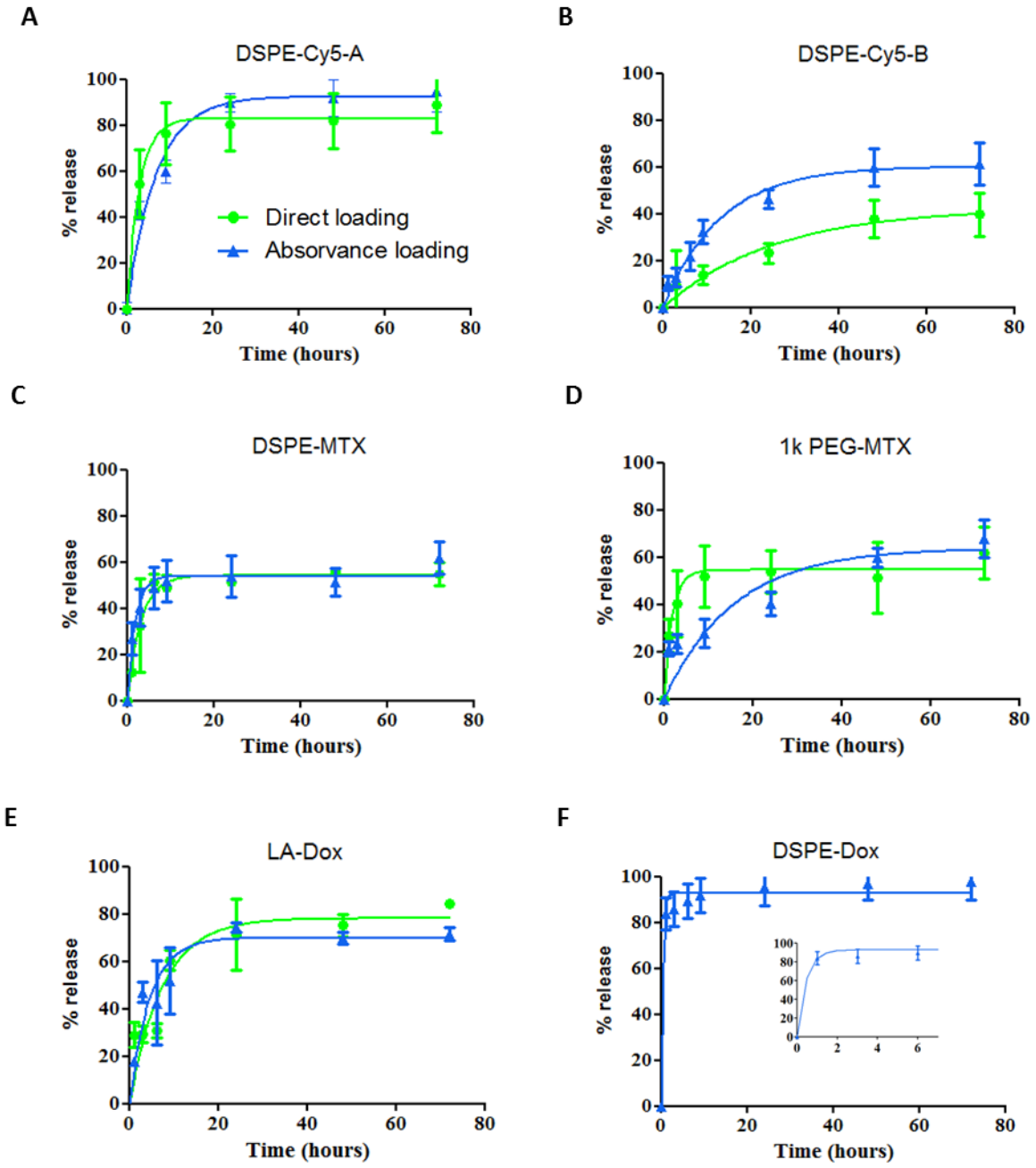

Figure 12 . Release profiles of the prodrugs from DPNs. *Release profiles for A. DSPE-CY5-A; B. DSPE-CY5-B; C. DSPE-MTX; D. PEG-MTX ; E. LA-DOX; and F. DSPE-DOX, which have been loaded via the "direct method" (•) and the "absorption method" (▪).*

The LA-DOX release is documented in Figure 12E. The release profiles for the direct and absorption loaded compound are quite similar to a moderate burst release within the first 24h. Indeed, this initial burst was lower than for the MTX as, over the first 10 hours, 55% and 50% of the LA-DOX was released via the absorption method and direct method, respectively. Then, a total of 70% and 65% DA-LOX was released at 24 hours, respectively. The DSPE-

DOX (Figure 12F) was only loaded through the abortion method, given its hydrophilicity. After the first hour, 80% of DSPE-DOX was already released out of DPNs. Note that DSPE-DOX is more soluble in water than DA-LOX, and this would explain the faster release rates documented for the first compound as compare to the second compound. This data confirms that the hydrophobicity/hydrophilicity ratio and molecular weight of the prodrug play a critical role also in optimizing the release profiles.

2.8. Cell viability studies for the DPNs and related prodrugs

Using the MTT cell proliferation assay, the cytotoxicity of DPN and its prodrugs were tested on MDA-MB-231 breast cancer cells at 24, 48, 72 and 96 hours. Free MTX and PEG-MTX manifested a modest cytotoxicity potential, which is in line with the existing literature. On the other hand, DSPE-MTX presented a much lower IC50 following in the verge of a few tens and a few μMolar concentrations, from 24 to 72h of incubation (Supplementary Figure 10A-C). However, the moderately low cytotoxicity associated with the low encapsulation efficacy returns an insufficiently high cell killing activity for the MTX loaded DPNs (Supplementary Figure 10D). Consequently, the cell viability analysis focused on the DOX prodrugs. In general, the LA-DOX prodrug treatments were associated with a delayed response as compared to free DOX. Specifically, at 24h, the IC50 decreased from 17.8 μM of free DOX to 34.01 μM of LA-DOX (Figure 13A-C). This trend was documented for all tested conditions and it should be ascribed to the hydrolyzation of the amide bond between DOX and oleic acid, which indeed require times. Importantly, the loading of LA-DOX into DPNs did not further reduce the cell-killing potential. Only at 24h, the IC50 values associated with LA-DOX DPNs were higher than for free LA-DOX (Figure 13C). As per DSPE-DOX, the loss in activity was even higher. At 24h, the IC50 decreased from 17.8 μM for free DOX to 196 μM for DSPE-DOX (Figure 13C). Even at 96h, there was a reduction in IC50 of about 50 times as compared to DOX and 5 times as compared to LA-DOX. However, the IC50 values for the DSPE-DOX and LA-DOX loaded DPNs were documented to be quite similar at 48, 72 and 96h of incubation (Figure 13C).

In order to characterize the drug uptake by the breast cancer cells, MDA-MB-231 were incubated with free DOX, prodrugs (DSPE-DOX and LA-DOX) and DPNs loaded with the prodrugs for 24, 48, 72 and 96h. Representative confocal fluorescent images are provided in Figure 13B). Both free DOX and free LA-DOX were observed to rapidly enter the cell and

distribute within the cytosol around the cell nuclei. This process was also observed for the DSPE-DOX and the DPNs loaded with DSPE-DOX and LA-DOX. However, in these latter three cases, cell internalization was significantly delayed in time because of the lower efficiency of DSPE-DOX in entering the cell, as compared to DOX and LA-DOX, and the time required to release the prodrugs from DPNs.

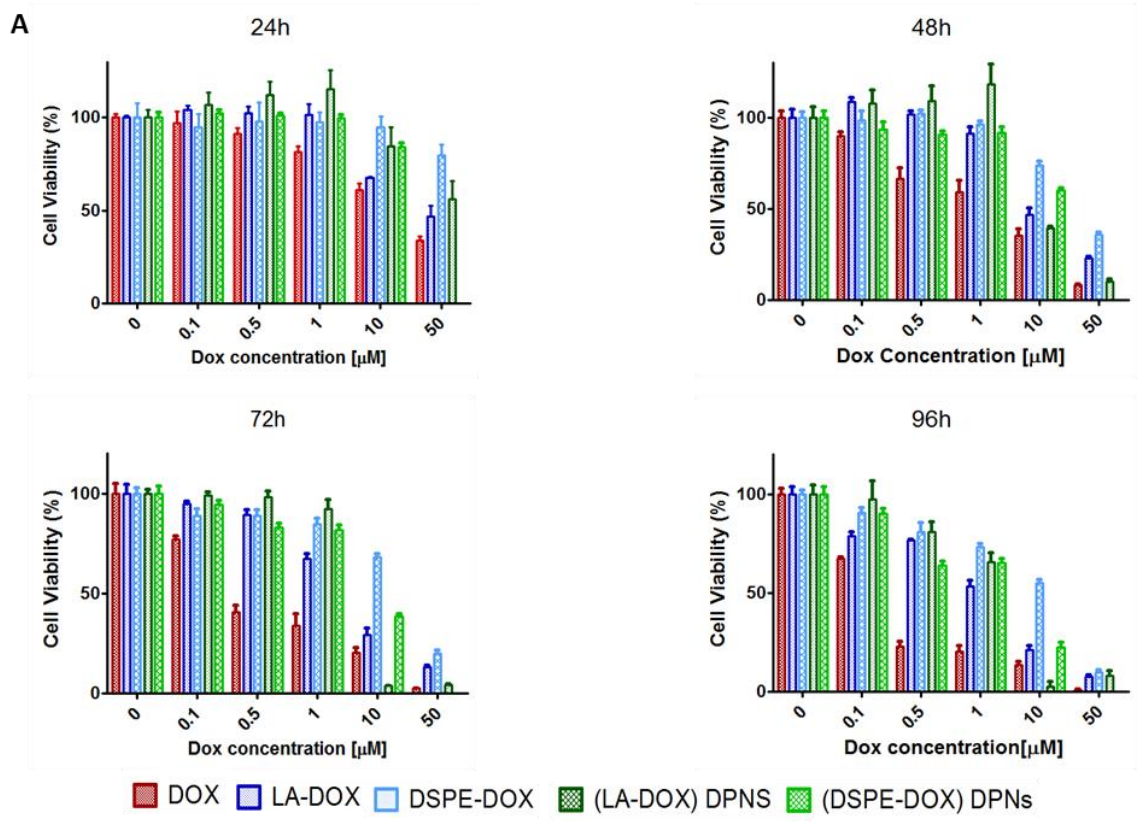

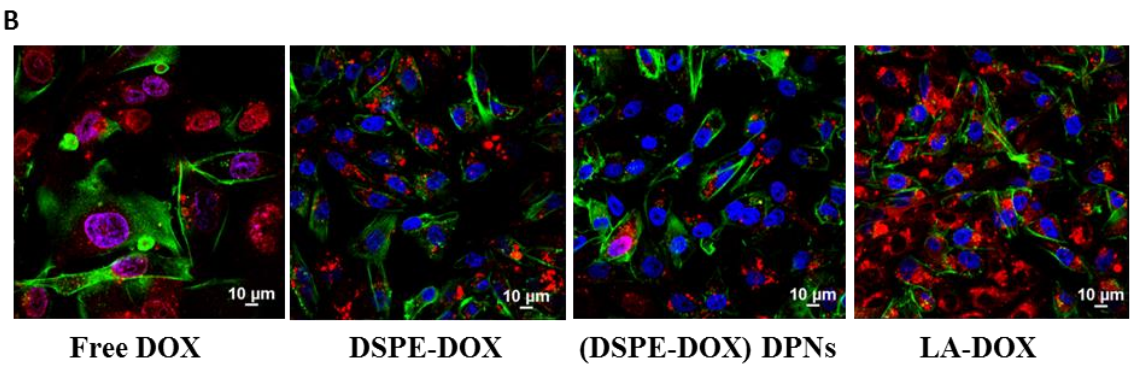

C

IC50 (mM)	24h	48h	72h	96h
Free - DOX	17.87 ±0,037	1.641 ± 0.050	0.4107 ± 0.033	0.1947 ± 0.026
LA-DOX	34.01 ± 0.033	10.61 ± 0.030	3.202 ± 0.029	1.336 ± 0.035
(LA-DOX) DPNs	65.35 ± 0.067	9.595 ± 0.076	3.324 ± 0.062	1.710 ± 0.034
DSPE-DOX	196 ± 0.059	28.31 ± 0.015	15.93 ± 0.038	7.760 ± 0.053
(DSPE-DOX) DPNs	54.53 ± 0.028	14.21 ± 0.031	5.129 ± 0.025	1.507 ± 0.031

Figure 13. Cytotoxic activity of DOX prodrugs and DOX-loaded DPNs. *A. Cell viability analysis of free-DOX, DSPE-DOX, DSPE-DOX DPNs and LA-DOX at 24, 48, 72 and 96h of incubation on triple negative breast cancer cells (MDA-MB-231). B. Representative confocal microscopy images of free-DOX, DSPE-DOX, DSPE-DOX DPNs and LA-DOX in MDA-MB-231 at 96h. C. Summarizing table listing the IC50 values for free-DOC, DSPE-DOX, DSPE-DOX DPNs and LA-DOX onto MDA-MB-231 at 24, 48, 72 and 96h of incubation.*

2.9. Pre-clinical biodistribution studies for the DPNs

DPNs directly loaded with DSPE-Cy5-B were administered into black mice via the tail vein injection. The accumulation of DSPE-Cy5-B DPNs in the different organs was assessed longitudinally by using a

whole animal, near infra-red fluorescent (NIRF) imaging system(Figure 14A). Representative images were taken at 0.5, 1, 2, 6, 24, and 48h post tail vein injection. Also, at 48h, the major organs such as the liver, spleen, kidneys, heart, lungs and brain, were harvested and imaged ex-vivo (Figure 14B). Given the absence of tumor mass or any other diseased tissues, DPNs were observed to accumulate within the abdominal cavity over time (Figure 14A). The lack of fluorescence signal in the bladder during the experimental observations would confirm a not significant leakage of DSPE-Cy5-B from DPNs during circulation. However, it should be highlighted that a moderate reduction in the Cy5 signal is observed in the abdominal cavity (Figure 14A), which would suggest a modest but sustained release of Cy5 from DPNs in agreement with the release studies of Figure 12B for the directly loaded molecule. The insets of Figure 14B confirm that the DPN accumulation in the liver. Indeed, this was expected given the lack of any diseased tissue.

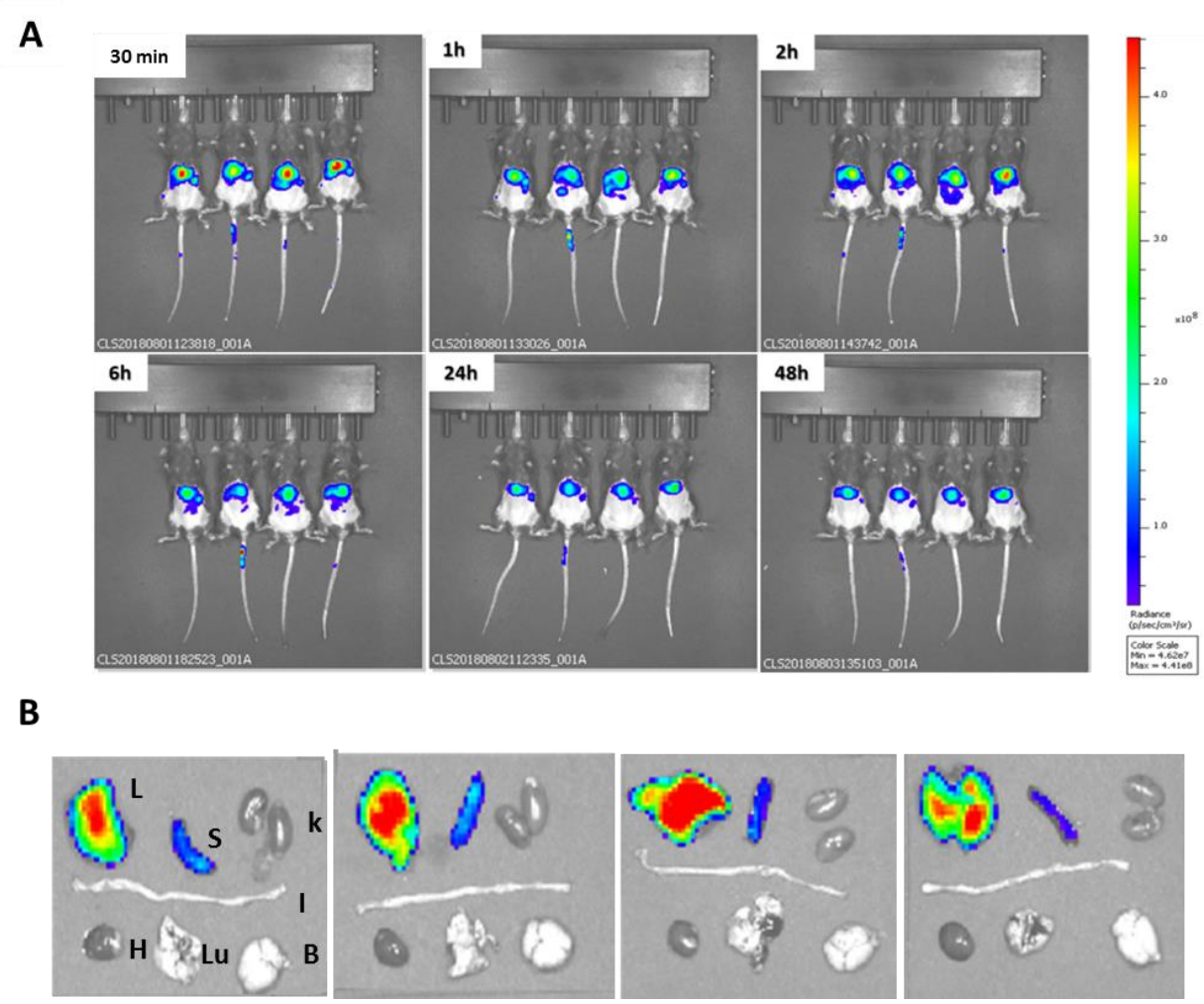

Figure 14. Polymeric Nanoconstructs Biodistribution at 30 min, 1h, 2h, 6h, 24 and 48 h Post Injection*. Representative ex vivo fluorescence images of the harvested liver (L), spleen (S), kidneys (K), intestine (I), heart (H), lungs (LU) and brain (B) from DSPE-Cy5-B DPNs injected wild type C57BL/6 mice. [n = 4]*

3. Conclusions

Although a variety of compositions and formulations of materials have been tested for nanomedicines, the design paradigm has not changed and is still mostly based on the EPR effect. the majority of nanoparticles described in the open litterature are spherical with an average diameter ranging from tens to a few hundred nanometers. They are the simplest to realize and given the size, they seem easily reach the target. However, following the biological inspiration, deformable non-spherycal nanoparticles with a characteristic submicrometric or even micrometric sizehave been shown to resist the sequestration of professional phagocytic cells, circulate for long time and efficiently deposit within the tortuous tumor microvasculature. Furthermore, model-based microfabrication strategies allow the development of polymeric nanoconstructures whose dimensions, shape, surface properties, mechanical rigidity and useful loads can be systematically and independently modified during the synthesis process. This supports the creation of a broad spectrum of polymeric nanoconstructs. One goal addressed in this work was the creation of a simple, reproducible, quick and efficient method for DPNs production with an enhanced yielding. In order to scale up the DPNs production, this study was first dedicated to the microfabrication process optimization. The first step of the fabrication, modified silicon-template approach through the use laser writer and electron beam lithography, allows us to control 2 of the 4S parameters (Size and Shape). The analysis was specifically focused on: the pattern design step; the defocus and dose parameter on the laser writing step; and the PDMS replica molding step. The pattern with nanometric structures has been reproduce on large areas, dozens of centimeters, leading to the production of an high number of particles (billions) in just a few hours. The conditions necessary to produce four different Nanoconstructs configurations (1µm circular shape, 2µm circular shape, elliptical and squared shape) were set up with the intent to study their in vitro and in vivo different behaviors.

Besides, this work involves for the first time the use of the DLW lithographic technique to fabricate a silicon master template presenting a so large array with structures in the limits of resolution.

Changes in polymer amount led to the creation of DPNs with different mechanical stiffness (s-DPNs, r-DPNs and rr-DPNs). These particles were used to dissect the influence of mechanical stiffness together with size and shape on macrophage nanoparticles

internalization. An atomic force microscopy analysis under wet conditions was performed to determine the morphological and mechanical properties of DPNs.

Moreover, the geometrical properties of all DPN configurations were plenty characterized using multiple, different techniques including confocal fluorescent microscopy, transmission electron microscopy, multisizer coulter counting, and dynamic light scattering.

Two different loading strategies were documented to encapsulate hydrophobic and hydrophilic imaging and therapeutic compounds within the polymeric matrix of the Discoidal Polymeric Nanoconstructs (DPNs). Two near-infra red imaging molecules were considered, namely Cy5A and Cy5B, together with two therapeutic molecules, methotrexate (MTX) and doxorubicin (DOX). The hydrophobicity/hydrophilicity ratio and molecular weight of these molecules were modulated by conjugating them directly with lipid (DSPE) and polymeric chains (PEG 1kDa). In the straightforward "direct loading" method, the compounds were first dissolved in the polymeric paste forming the DPNs and then, together with this paste, applied to the PVA template. This approach suffered of the current sub-optimal fabrication yielding of DPNs returning encapsulation efficiencies lower than 1%. In the "absorption method", the compounds were resuspended in water at high concentrations (1 mg/ml) and dragged inside the polymeric matrix of DPNs upon their rehydration. This approach required a fine tuning between the compound hydrophobicity and molecular weight and returned encapsulation efficiencies as high as 80%. In addition, direct loading was associated with lower release rates as compared to absorption loading, for a given compound. This was ascribed to the fact that the compounds in the absorption loading are mostly confined in the vicinity of the DPN surface and are therefore more rapidly released into the surrounding aqueous environment. Differently, in direct loading, the compounds are uniformly distributed within the polymeric matrix.

Collectively, these results demonstrate that the pharmacological properties of DPNs can be finely tuned during the fabrication process by changing the loading strategies (direct vs absorption) and compound properties (hydrophobicity and molecular weight). Future studies will focus more on further optimizing the loading and release conditions and pre-clinically demonstrate the therapeutic and imaging performance of this drug delivery platform in different disease models.

Finally, the DPN fabrication process can be integrated with roll-to-roll and roll-to-plate industrial technologies, which allow scaling up in concert with good manufacturing practices

3. Chapter: Mechanical-control of chemotherapeutic drug efficacy

The goal of this part of my PhD is to investigate the impact of mechanical stress on drug efficacy. We studied different mechanical perturbations that may contribute to a mechanical-form of drug resistance. We investigated different types of mechanical stresses: mechanical compression (3D level), osmotic stress (3D level) and rigidity (2D level). Compressive stress is the least studied of mechanical stresses. To achieve these goals, we developed a new experimental strategy to exert a well-defined mechanical stress on multicellular tumor spheroids for over 20 days. Essentially, we used two strategies to apply mechanical compressive stress at the 3D level: dextran osmotic stress and agarose confinement. We then tested the drug efficacy of common pancreatic cancer chemotherapeutics, Gemcitabine and docetaxel. The basic growth curves that we had display d(t)/d0, the spheroid diameter d(t) normalized by the initial diameter of the spheroid d0. Since the geometry is spherical, diameter measurement gives as much information as volume measurement.

3.1. Context

3.1.1. Cancer progression: role of mechanical stress

Cancer progression occurs in several phases: schematically, the tumor grows locally, then typically invades the nearby tissue called stroma composed of extracellular matrix, fibroblasts, immune cells and capillaries. Proliferation during the early stages of the tumor is controlled by three macro-elements: gene mutations, biochemical and mechanical parameters imposed by the micro-environment. Biochemical and mechanical factors are difficult to isolate *in vivo* to measure their respective importance. The idea that mechanical stresses in tumor development can play a key role is increasingly supported (98) (99) (100) (101) (102) (103). In most solid tumors, the growth occurring in constrained environments entails a competition for space and this requires that cells physically push onto their surrounding environment and to create space to be able to divide (fig. 15a). This is a physical force that cells exert on their microenvironment. The competition for space results in a mechanical coupling between the tumor and the stroma: the expanding neoplastic tissue compresses the stroma which accumulates and stores an internal stress. Moreover, stromal elements can participate in mechanical stress build up. For instance, myofibrobalasts, the contractile component of the stroma, as well as high deposition of hyaluronan can exert mechanical compressive stress on the tumor (fig. 15b) (104).

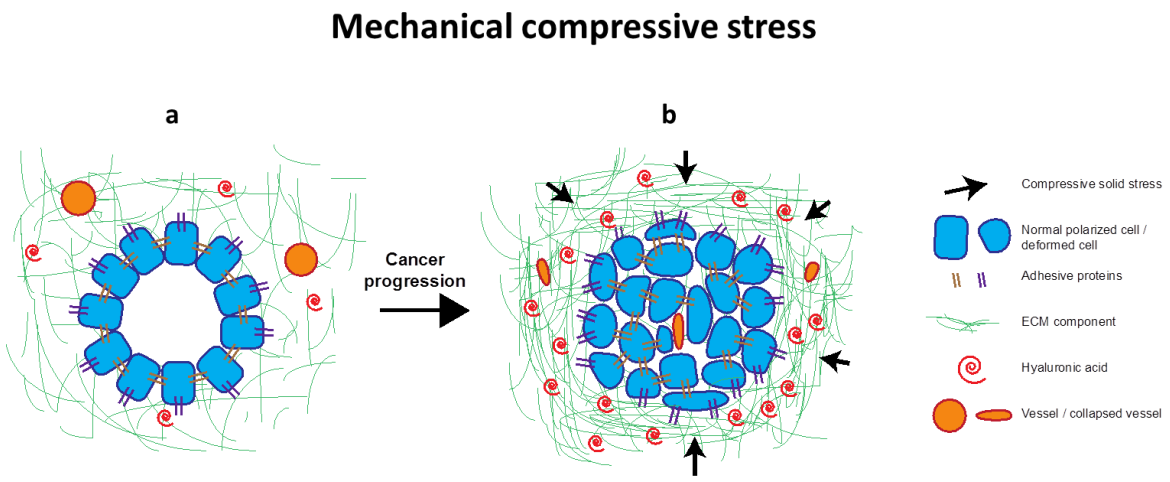

Figure 15. Mechanical compressive stress accumulating during tumor growth*. (a) In most solid tumors the growth occurring in constrained environments entails a competition for space ; (b) the neoplastic cells physically push their surrounding environment and the stroma accumulates and thus stores an internal stress (this pressure could lead vessels collapse).*

It has been shown that mechanical stress leads to a reduction of tumor cell proliferation (105) (106) (107) (108) and induces mitochondrial apoptosis (cellular suicide) (5) (109) (110). Despite these experimental evidences, the role of the microenvironment and its interactions with the tumor is not yet clear (13). Probably, a quantitative analysis is difficult because large tumors are polyclonal, their shapes are often poorly defined, they are heterogeneous and biochemical signaling interferes with mechanics (111) (112). However, a quantitative knowledge of the mechanical properties of tissues is of paramount importance for understanding tissue growth and invasion.

3.1.1.1. Tensile and compressive mechanical stresses

Mechanical stresses can be divided into two main groups: tensile and compressive stresses. Tension naturally emerges from cell–cell and cell–substrate adhesion, and has been shown to affect cell proliferation, cell death, cell migration, and even cell differentiation (113) (114) (115) (116) (117). Mechanical compressive stresses arise in a spatially limited environment and can also modulate cell division and migration (105) (106) (118). For instance, tumor multicellular aggregates growth can be inhibited when embedded in an elastic agarose gel (110). In particular, the stiffer the agarose gel, the stronger the inhibition. Agarose gels are deformed by the growing aggregate. As a consequence, they mechanically react by applying an increasing stress to the spheroid. Above a certain stress, spheroid growth stalls.

Tensile stresses have been extensively studied and much is known about their molecular integration (119). On the contrary, relatively little is known about the molecular determinants responding during mechanical compression. Tensile stresses mostly concern cells of the outer layer of the tissue that interact with the external microenvironment through adhesive proteins, instead the compressive stresses, even if in different ways, affect any cell into the tissue. Despite these qualitative observations, the precise mechanisms linking mechanical forces to tumorigenesis remain unknown. One reason why progress in understanding the role of mechanical stress did not follow the pace of biochemical studies is the lack of adequate tools to measure *in vivo* or *in vitro* forces in 3D culture models. The cells constantly receive various physical forces associated with the tissues, including hydrostatic pressure, shear stress, solid compression and tension, and among these we are able to precisely measure only a few. Moreover, dissociating the combined effect of these stresses is important to assess them properly.

3.1.2. Mechanical forms of drug resistance

What are the mechanisms of drug resistance? Many past studies have identified key features which can eventually lead to drug resistance. Most studies have focused on the very inactivation of the drug by the host, the alteration of the drug target, the efflux of the drug from the cell, or DNA alterations that could create *de novo* resistance (120). All of these mechanisms are cell-centered, but there is an increasing realization that stromal components could also participate in the mechanisms of drug resistance. Incidentally, the lack of stromal components when investigating new therapeutic targets could explain the large fraction of drugs failing clinical trials.

As we mentioned above, cancer cells constantly interact with their mechanical environment and the whole tissue is confined and compressed by its surrounding. Compressive mechanical stress develops from cell proliferation and finally, the elevated mechanical stress could result in the clamping of blood vessels leading to increased interstitial fluid pressure (hydrostatic pressure) (Figure 15b). The consequent hypoperfusion and interstitial hypertension pose important obstacles to drug delivery and may exclude large intratumor areas from therapeutic agents of blood origin, which could lead to reduced efficacy of chemotherapy (8) (9). In this case the mechanical stress creates a real physical impediment to the drug to reach the tumor site or part of it (121). It is quite obvious to imagine that if the drug fails to reach the tumor it cannot work on it. However, what happens from compressed tumors with sufficient

perfusion? Such situation could arise for mechanical stress not high enough to collapse blood vessels, but large enough to have a physiological effect on tumor cells.

While some recent studies show that mechanical stresses, tensile (122) (123) (124) compressive (104) (125), or shear (125) (126) (127) are associated with drug resistance, the mechanisms leading to such resistance are still elusive. Most of the drugs tested and current chemotherapeutic strategies require cells to proliferate in order to work: for instance, Gemcitabine is a DNA incorporating agent promoting irreversible error during DNA replication leading to cell death, and docetaxel prevents normal breakdown of microtubules during division, also leading to cell death. Consequently, if a cell does not proliferate, these drugs would not work. We and others have shown that tensile or compressive have been linked to a cell cycle arrest (106) (128), which can be a potential additional form of drug resistance. The idea that quiescence can be a dominant mechanism leading to drug resistance is appreciated (129), but its relationship with mechanical stress has not yet been demonstrated.

Although remaining an underexplored axis of research, the mechanisms coupling drug resistance to mechanical stress could bridge the gap between the cell-oriented research and the impact of the mechanical environment, which could both inform on approaches to better delineate chemotherapeutic strategies and design new high-throughput screening platforms.

We propose that mechanical perturbations of the tumor microenvironment may contribute substantially to the mechanism of Gemcitabine drug resistance.

3.1.3. Gemcitabine: metabolism and molecular mechanism of action to treat pancreatic cancer.

Gemcitabine is a nucleoside analog that has been used as a chemotherapeutic agent for more than 15 years (130). Proliferating cells are the target of Gemcitabine where it replaces cytidine during DNA replication. This process decrease tumor size, as new nucleosides cannot be attached to the "faulty" nucleoside, resulting in apoptosis.

Gemcitabine has become the standard treatment choice for locally advanced and metastatic pancreatic cancer, for which there have been few treatment advances.

Gemcitabine (2',2'-difluoro-2'-deoxycytidine) is a deoxycytidine analog with multiple modes of action inside the cell (figure 16a). The basics of Gemcitabine metabolism is illustrated in Fig. 16b. Gemcitabine is a prodrug that requires cellular uptake and intracellular phosphorylation in order to exert its action (Figure 16b) (131) (132).

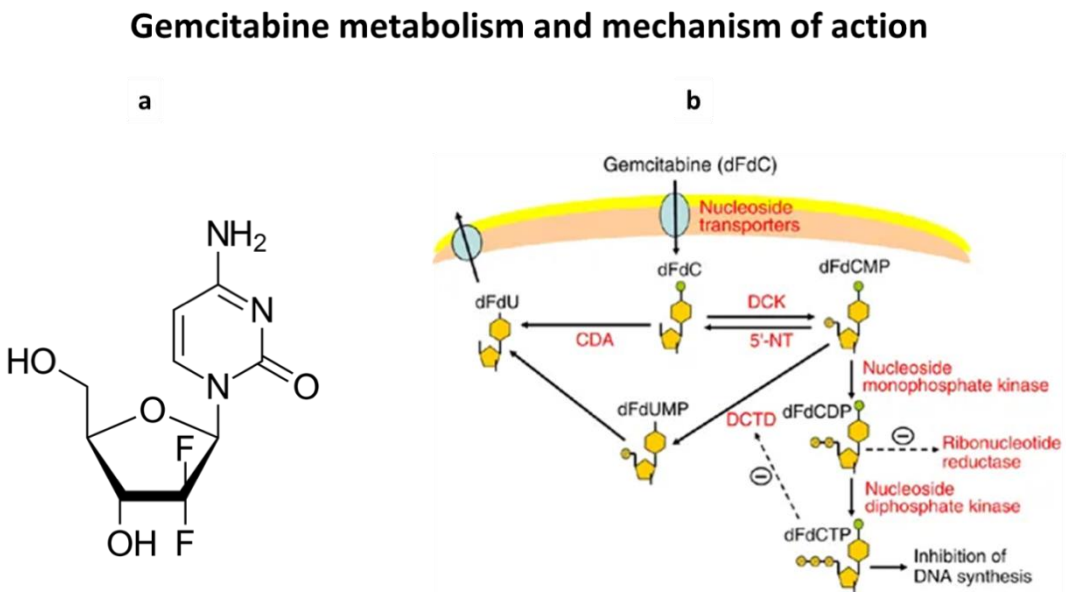

Figure 16. *(a) (2',2'-difluoro-2'-deoxycytidine ; (b) Gemcitabine metabolism and mechanism of action (133).*

Once administered, Gemcitabine is transported into cells by nucleoside transporters. Gemcitabine is then phosphorylated into Gemcitabine monophosphate (dFdCMP) by deoxycytidine kinase (DCK), and dFdCMP is subsequently phosphorylated to Gemcitabine diphosphate (dFdCDP) and Gemcitabine triphosphate (dFdCTP) by nucleoside monophosphate (UMP/CMP) and diphosphate kinase. The most important mechanism of action of Gemcitabine is inhibition of DNA synthesis (134). When dFdCTP is incorporated into DNA, a single deoxynucleotide is incorporated afterwards, preventing chain elongation (135). This non-terminal position of Gemcitabine makes DNA polymerases unable to proceed, in a process known as 'masked chain termination', which also inhibits removal of Gemcitabine by DNA repair enzymes (134). Moreover, it is known that Gemcitabine has a unique mechanism of action known as 'self-potentiation' (136). For example, dFdCDP potently inhibits ribonucleotide reductase, resulting in a decrease of competing deoxyribonucleotide pools necessary for DNA synthesis. Again, dFdCTP suppresses inactivation of dFdCMP by inhibiting deoxycytidine monophosphate deaminase (DCTD). On the other hand, more than 90% of administered Gemcitabine is converted, and thus inactivated, by cytidine deaminase (CDA) into 2′-deoxy-2′,2′-difluorouridine (dFdU). Phosphorylated metabolites of Gemcitabine are reduced by cellular 5′-nucleotidase (5′-NT), and dFdCMP is also converted, and inactivated, by DCTD into 2′-deoxy-2′,2′-difluorouridine monophosphate (dFdUMP).

Like many other drugs used in cancer chemotherapy, resistance to Gemcitabine may be intrinsic, but it can also be acquired by individual patient during treatment cycles. Several mechanisms have been reported in the literature; however, as many of these processes are complex, it can be difficult to understand the precise roles and, indeed, consequences in chemoresistance. Anyway the only strong correlations with gemcitabine sensitivity are DCK activity and dFdCTP pools, with a potential important role for ribonucleotide reductase. These mechanisms have been extensively reviewed (137) (138) (139).

It is not known exactly why Gemcitabine is active against pancreatic cancer while other chemotherapeutic agents are not. However, the tumor environment is thought to be important. This malignancy is characterized by deficient vascularization and dense stroma, which is therefore difficult to penetrate by many drugs as well as the immune system. In fact, among all epithelial tumors, pancreatic cancer is known to possess an extensive desmoplastic reaction, which may account up to 90% of the tumor volume (140). Thus, desmoplastic results in poor drug delivery and intrinsic chemoresistance.

The introduction of Gemcitabine triggered several exploratory studies of its combination with other therapeutic agents. In particular Gemcitabine and Docetaxel were combined into advanced pancreatic cancers (Phase II or III) as second line therapy (141) (142) (143) (144). From these studies came out that Gemcitabine and docetaxel had encouraging activity in patients with advanced pancreatic cancer.

3.1.4. Pancreatic cancer as a model cancer to study a mechanical-form of resistance

Pancreatic ductal adenocarcinoma (PDAC) is one of the deadliest human neoplasms with extremely poor prognosis when diagnosed and no efficient treatment available (145). PDAC development is characterized by excessive deposition of extracellular material during which strong modifications of the mechanical environment arises. In particular, the deposition of negatively-charged hyaluronic acid leads to electroswelling of extracellular matrix and subsequent compressive stress experienced by tumor cells (146). The local growth of cancer cells in an elastic environment also leads to build-up of solid stress through a process known as growth-induced pressure (3) (147). Pain in the abdomen or back is common in pancreatic cancer. Pancreatic tumors can grow large enough and quickly begin to feel the pressure of nearby organs, causing pain (148). PDAC tumors are extremely compressed, within the kPa range (149).

These physical forces could compress the blood vessels causing poor and heterogeneous tumor perfusion. Moreover, these mechanically-induced changes could create a barrier to the delivery and efficacy of chemotherapeutics (150).

In fact, the rapid clinical decline commonly observed in patients with pancreatic cancer has been attributed both to the aggressive biological nature of PDAC and to the ineffectiveness of systemic therapies available for patients with advanced disease (151) (152). After surgical resection of PDAC, the nucleoside analogue Gemcitabine has been widely used for many years as standard treatment based on the results of the European Study Group study for Pancreatic Cancer-3 (ESPAC-3) (153). Over the years many combination therapies of Gemcitabine and other drugs have been introduced (141) (154), in particular Gemcitabine with nab-paclitaxel has been shown to have a beneficial effect on patient survival (155). Although these chemotherapeutic drugs gave a great improvement in pancreatic cancer, the median survival rate remained small (145). An explanation for the poor response of patients to systemic therapies was provided in an accurate PDAC mouse model from the demonstration that chemotherapy is poorly delivered to PDAC tissues due to a lack of vascularization (156). This vascular deficiency was related to the presence of the dense stromal matrix which constitutes the mass of tumors of the PDAC (figure 17). The stromal cells contained in the PDAC tumor microenvironment are therefore an additional component of neoplastic cells that should be critically evaluated for optimal therapeutic development.

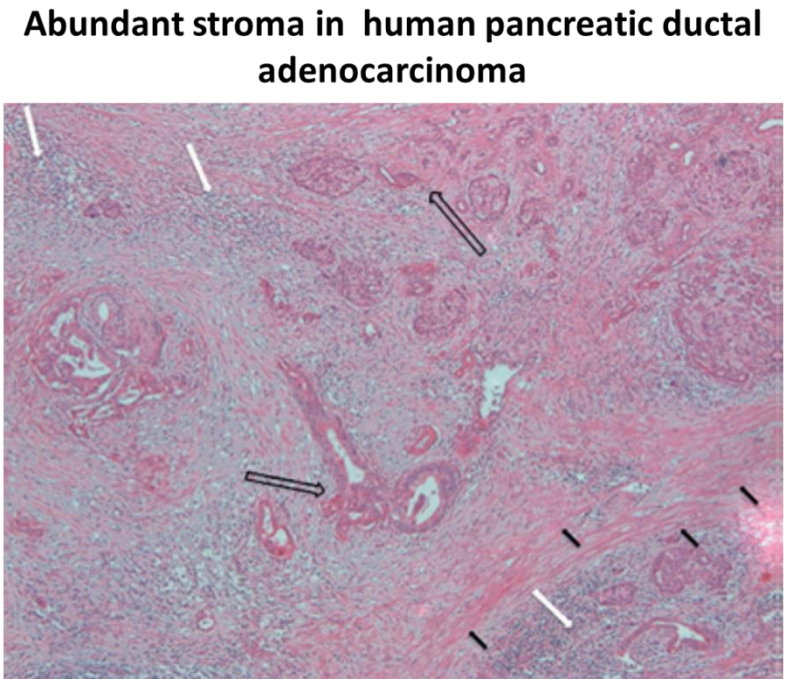

Figure 17. Stain of human pancreatic ductal adenocarcinoma *showing a prominent desmoplastic reaction (black arrows) neoplastic ductal cells (arrows) and inflammatory cells (white arrows) (140).*

In the past, the stroma was considered as a spectator during pancreatic carcinogenesis. Pancreatic cancer was understood as a multistage process characterized by the accumulation of genetic alterations accompanied by typical morphological and histological changes in pancreatic ductal cells. Activating mutations in the Kras oncogene occur early during malignant transformation, followed by subsequent somatic mutations involving the tumor suppressor genes p16, p53 and DPC4 (157) (158). Classical molecular biology concepts are increasingly replaced by complex multidisciplinary approaches that address stromal determinants and their interplay in PDAC. Based on recent sequencing studies and transcriptional profiling analyses on PDAC, it is acknowledged that the tumor microenvironment plays a pivotal role during pancreatic carcinogenesis and therapeutic resistance (140) (159).

Pancreatic cancer is characterized by a pronounced desmoplastic and hypovascular microenvironment. The development of fibrosis is a dynamic phenomenon where ECM formation takes place in the interstitial spaces and in areas where the exocrine compartment, mainly acinar cells, is damaged (160). PDAC stroma consists of activated fibroblasts, Pancreatic stellate cells, infiltrating immune cells, all cells produce key molecules during fibrosis collagen types I, IV, and V, and fibronectin, laminin, matrix metalloproteases (MMPs) and their inhibitors, tissue inhibitors of metalloproteinases (TIMPs), and TGFβ. Since in the last years, different studies have concluded that the tumor stroma modifications promote PDAC progression and mediate therapeutic resistance, strategies have been setup in order to target tumor stroma components and pathways. In particular, the targeting of the stromal cells results in an increased intratumoral perfusion and therapeutic delivery of Gemcitabine if used in combination with drug targeting ECM rigidity (156). However, these studies were mostly done *in vitro* or in transplanted immune deficient *in vivo* models, without taking into consideration the real complexity of pancreatic cancer microenvironment. Indeed, clinical trials with the matrix metalloproteases inhibitors marimastat/BAY1295-66 failed. The disappointing clinical outcome of these and others studies based on increase drug delivery strategy led to the understanding that the role of the stroma as PDAC promoting or suppressor is dependent on tumor stage, tissue context and others microenvironment component (159). This is supported by interesting works showing that in different genetic engineered mouse models (GEMMs), the depletion of carcinoma associated fibroblasts, which are a driver for desmoplastic stroma formation, accelerates pancreatic cancer (161). Interestingly one

effective approach in clinic to address the stroma seems to target non-cellular components. Preclinical studies in GEMMs demonstrate that the drug PEGPH20, a recombinant hyalurodinase able to degrade hyaluronic acid (HA), induce an increased tumor blood vessels perfusion and delivery of chemotherapeutic agents (162).

Even though drug resistance stemming from mechanical stress may be general to any cancer, we propose to investigate the role of mechanical stress on pancreatic ductal adenocarcinoma (PDAC). This cancer, as we explained above, presents strong modifications of stromal components, a higher matrix rigidity and a subsequent abnormal solid stress in comparison to healthy tissue which contribute to cancer progression and resistance to current treatments, making it a perfect candidate to study the impact of compressive stress. How mechanical stress affects PDAC development and treatment remains elusive. Note that in this study we decided to not consider the potential drug resistance due to hypoperfusion of tumor tissues under mechanical compression.

We propose that mechanical perturbations of the tumor microenvironment may contribute substantially to the mechanism of drug resistance.

3.2. Focus of the work

The goal of this work is to understand the impact of mechanical stress on drug efficacy. We tested the mechanical stress on pancreatic cancer progression *in vitro*, and in that context, the efficacy of Gemcitabine chemotherapy. We measure the effect of a compressive mechanical stress on the growth of multicellular spheroids over time scales longer than the typical time scales of cell division or apoptosis. A good candidate for such studies is the multicellular spheroid (MCS), introduced by Sutherland et al. (163) as a tumor model system: three-dimensional cellular aggregates that remarkably mimic the relevant *in vivo* physiological gradients of mitogens, oxygen, or glucose. They have been extensively used as model system for the study of drug delivery, cell proliferation or even angiogenesis (164). Although their mechanical properties may differ from those of tumors, for many purposes, MCS can be seen as a tumor subunit. Since they have no biochemical crosstalk with their environment, MCS are ideal for assessing the impact of mechanical stress on tumor growth (165) (166). We prepare PDAC cell spheroids derived from mouse A338 K-Ras^{G12D} constitutively mutated cell line.

Growth of a tumor occurs through an abnormal proliferation program of cells (167) (168), which as a consequence induce growth-induced compressive stress accumulation at the tumor–stroma interface. In order to study the spheroid growth response to compressive mechanical stress we use an agarose gel as a highly simplified stroma. Several groups have been seeding gels with cell aggregates (110) (166) (5) (6): during growth, the cell aggregate has to distort the gel resulting in an elastic stress (figure 18). The stiffer the gel, the smaller the growth rate of the aggregate and its final size at steady state. In other hands, tumor multicellular aggregates growth can be inhibited when embedded in an elastic agarose gel (110). In this work we use a new experimental strategy to exert a physical mechanical compressive stress onto the whole multicellular tumor spheroid for a period of time which can exceed 20 days (figure 18).

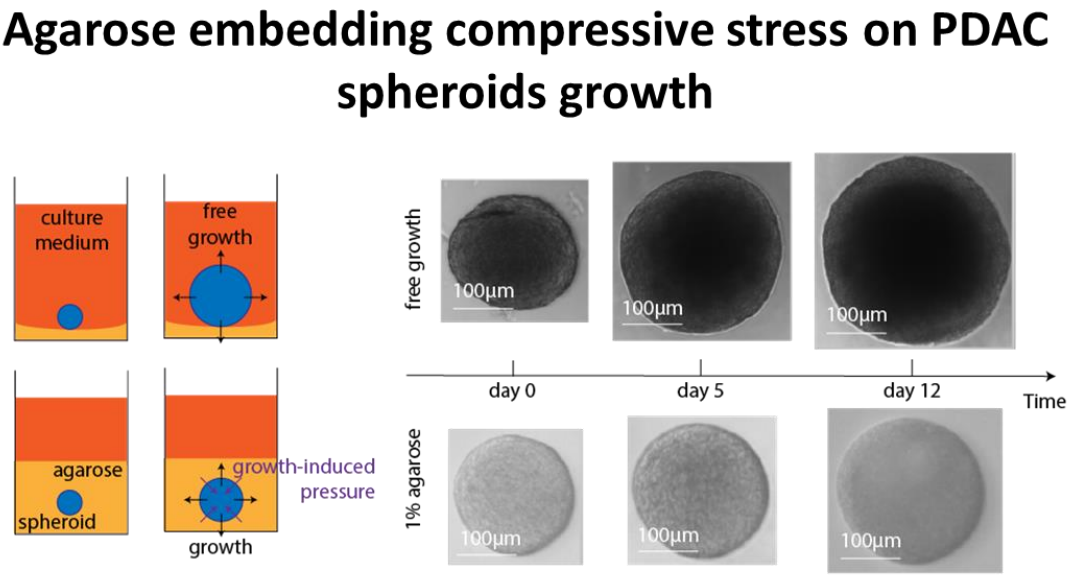

Figure 18. (Left) free and agarose embedding spheroids growth scheme*: because the spheroid growth (arrows to outside) the agarose mechanically reacts by applying an increasing stress to the spheroid (arrods to inside) ;* ***(Right) Free and embedded spheroids size evolution.***

Subsequently, we tried to make consistent the the tumor growth mechanical stress dependence, testing other mechanical stresses. For this purpose we used a high molecular weight Dextran to induce an osmotic compressive stress on the spheroid. The dextran has been shown in previous works to reduce the growth of colon carcinoma cell spheroids (169) (170) (105) (106). This polymer is known to be neutral and is not metabolized by mammalian cells (169). Unlike more physiological osmolytes, such as glucose or ions (Na+, Mg2+, etc), dextran macromolecules are not internalized by cells, and do not infiltrate the intercellular.

Thus, they exert a constant osmotic stress onto the whole spheroid and induce a water efflux from the spheroid (171) (107), probably from the matrix components (172). Moreover, it has been observed that such a small osmotic pressure has no long term effect on proliferation or death for cells cultured in 2D (107). We used a stress of 0.5 kPa, 1kPa and 2kPa and it is worth noticing that even 5 kPa is a rather small stress corresponding to the osmotic pressure exerted by 1 mM NaCl (107). We investigated the similarities between agarose mechanical and dextran osmotic stresses.

Cancer cells due to their growth in a rigidity-changing environment are subjected to a tensile stress mediated by the substrate stiffness. The stiffness and the geometry of the substrate on which cells grow have indeed a strong impact on cell division (173), migration (174) and differentiation (175). Starting from these considerations we wanted to confirm further our hypothesis of tumor progression in dependence on mechanical stress. We investigated the role of substrate stiffness as a source of mechanical stress: we performed a 2D-experiment with 2 specific rigidity plates with Young moduli of 0.5 kPa and 64 kPa.

Once we saw a reduction in growth as a function of different mechanical stress, we wondered whether that meant even reduction of cell division and proliferation. Therefore, we performed an *ad hoc* capillary Western blot analysis and, when we could, immunostaining of sections.

Once we understood which was the stress-mediated proliferation within the compressed spheroids we investigated what was the efficacy of a proliferation-based chemotherapy. We evaluated the growth evolution of spheroids treated with Gemcitabine under progressive compressive agarose stress and under constant osmotic stress of dextran.

3.3. Methodologies

3.3.1. Cell line and 3D culture

Pancreatic ductal adenocarcinoma (PDAC) cell line model was used in this work because of the strong modifications of the mechanical environment during progression of this cancer (104). For this study, we used immortalized PDAC murine cell lines: a constitutively active $Kras^{G12D}$ mutant (oncogene mutated in 95% of pancreatic cancer (176)), A338. Kras mutation is present in 95% of cases and is a gene involved in proliferation and invasion pathways (176). Our collaborators in the group of Julie Guillermet-Guibert (CRCT - Centre de Recherche en Cancérologie de Toulouse) derived this cell line from mice pancreatic cancer lesions. The cells were cultured with Dulbecco's Modified Eagle Medium (DMEM) containing 10% FBS (Gibco, Thermo Fisher Scientific, USA), 1% penicillin/streptomycin (Sigma-Aldrich, USA), under a controled atmosphere (37°C, 5% CO2, 95% air).

Given the complexity of the tumor systems, uncoupling the effect of biochemical and mechanical interactions is a daunting challenge. A good candidate for such studies is the multicellular spheroid (MCS) as a tumor model system: three-dimensional cellular aggregates which remarkably mimic the relevant in vivo physiological gradients of mitogens, oxygen, or glucose (163). They have been extensively used as tumor model systems (164) for the study of drug delivery (177), and three-dimensional cell proliferation (178). Although their mechanical properties might differ from those of tumors, for many purposes, MCSs can be viewed as a tumor subunit. Because they do not have any biochemical crosstalk with their environment, MCSs are ideal to evaluate the impact of mechanical stress on tumor growth (165) (166).

We make spheroids using a classical agarose cushion protocol (179) : an agarose pad of 200 µl of agarose 2% is prepared first into a well of a 48 multiwell plate, then 600 µl of 1800 cells/ml suspension are placed on the agarose pad and the spheroid is formed (figure 19a). The the spheroid is formed in the center of the well following the curvature of the agarose in less than 24h (169) (170) (106) (fig. 19a).

3.3.2. Chemotherapeutic drugs

Gemcitabine, Docetaxel and the smart drug SPNs–Docetaxel were used against the pancreatic cancer spheroid progression.

Gemcitabine is a nucleoside analog used as chemotherapy. The drug replaces cytidine during DNA replication of S-phase cells creating an irreversible error. The process arrests tumor growth, as new nucleosides cannot be bound to the "faulty" nucleoside, resulting in apoptosis. Gemcitabine is used in various carcinomas: non-small cell lung cancer, pancreatic cancer, bladder cancer and breast cancer (130). When 10μM of Gemcitabine is added to pancreatic cancer spheroids, we observed a progressive decrease of its volume over time, until all the cells eventually die out at a 10 μM concentration.

Docetaxel is of the chemotherapy drug class; taxane, is a chemotherapy medication used to treat a number of types of cancer. This includes breast cancer, stomach cancer, prostate cancer, non-small-cell lung cancer and second-line therapy in patients with advanced pancreatic cancer (180). The cytotoxic activity of docetaxel is exerted by promoting and stabilizing microtubule assembly, while preventing physiological microtubule depolymerization / disassembly in the absence of GTP. This leads to a significant decrease in free tubulin, and results in inhibition of mitotic cell division preventing further cancer cell progeny (181). We used the same drug concentration (10μM) to compare the effect with the Gemcitabine.

Spherical Polymeric Nanoconstructs (SPNs) are ideal for targeting solid tumors via the enhanced permeability and retention (EPR) effect (182). Moreover, the SPNs had been biologically and chemically characterized *in vitro* and their *in vivo* therapeutic and imaging efficacy in mouse cancer cells heve been proven (182). This platform consist of a hydrophobic poly(lactic- co –glycolic acid) (PLGA) polymeric core stabilized by an external monolayer of phospholipids and poly(ethylene glycol) (PEG) chains. The hydrophobic core contains docetaxel (DTXL) and fluorophore Lipid-Cy5. The SPNs were made out of the same materials as DPNs but were obtained via an emulsion/nanoprecipitation approach (182) returning a spherical shape with a diameter of 172.4 ± 0.1 nm (PDI = 0.115 ± 0.03) and $\zeta = -44.6 \pm 1.14$ mV. The Nanocontructs Docetaxel drug loading were verified by HPLC analysis and the Docetaxel concentration used was always 10μM.

3.3.3. The growth of multicellular spheroid embedded in agarose gel

To investigate the role of mechanical compression on cell physiology we developed a new protocol consisting in embedding multicellular spheroids inside an agarose gel. Rather than

embedding single cells as it was previously performed (110) the whole spheroid was embedded, which enables an easier tracking in time. The new embedding method proposed in this study is reported in the fig. 19 b. It essentially consists in mixing a 2/3 days-old spheroid with a low melt agarose matrix at 37°C and then induce a fast polymerization of the agarose on ice to avoid that the spheroid sediments at the bottom and is not fully embedded in 3D. After that the spheroid is allowed to grow under confinement for 2 more days and is then treated with the chemotherapeutic drug.

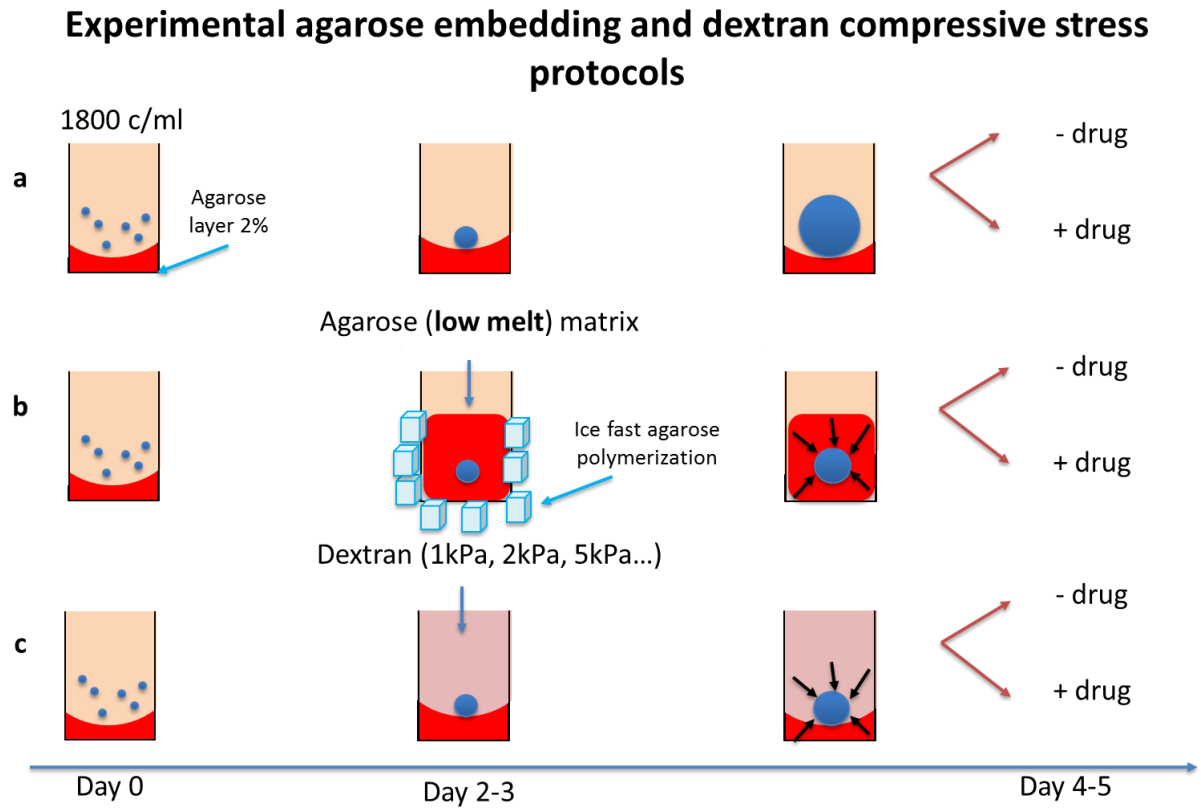

Figure 19. Experimental agarose embedding and dextran compressive stress schematic protocols. (a) growth of control spheroids without mechanical stress : at the day 0 the cells are seated into the well to make spheroid, at the day 4 or 5 in one case was added the chemioterapic. (b) growth of spheroids with agarose embedding compressive stress : at the day 0 the cells are seated into the well to make spheroid, at the day 2 or 3 the spheroid was embedded into an agarose matrix by ice fast polymerization at the day 4 or 5 in one case was added the chemioterapic - The black arrows rapresent the emergency growth induced compressive stress ; (c) growth of spheroids with dextran compressive osmotic stress : at the day 0 the cells are seated into the well to make spheroid, at the day 2 or 3 the medium was replaced with medium – dextran solution, at the day 4 or 5 in one case was added the chemioterapic – the black arrows rapresent the osmotic compressive stress on the spheroid.

More precisely, a 48 multiwell plate is placed on ice and in the same time a low melt agarose suspension at double-concentration (2X) is prepared. Then, 400 µl of medium is carefully removed from the well containing a 2/3 days old spheroid. The remaining 200 µl of medium, that should contain the spheroid, is mixed with 2X low-melt agarose matrix. Then, the resulting 400 µl of agarose + spheroid + medium is placed in the 48 multiwell plate on ice to induce a rapid agarose polymerization and subsequent spheroid embedding in the central

position of the well. At this point the spheroid is allowed to grow under confinement in the polymeric matrix of agarose and as it grows it develops a growth-induced pressure from polymer that confines it. After 2 days 10 µM of drug was added and the spheroid growth was followed for several days.

The agarose concentrations used to induce a growth induced compressive stress are 1% and 0.5%. Careful rheological measurements on the stresses associated with different agarose matrices were performed by collaborators from the ILM lab in Lyon, France to calibrate the amount of growth-induced pressure and asses in which condition we can use it.

3.3.4. Multicellular spheroids growth in osmotic stress Dextran

A high molecular weight Dextran (Dextran from Leuconostoc spp. 100kDa – Sigma Aldrich) was used to compress multicellular spheroids: spheroids were cultured in a medium supplemented with dextran polymer (169) (fig 19a and 19c). Dextran macromolecules are not internalized by cells, and do not infiltrate the intercellular space of spheroids (169) (105) (170) (106). In this protocol, 300 µl of medium is removed from the well containing a 2/3 days old spheroid and 300 µl of 2X dextran solution is added. As in the previous case, the spheroids grow under compressive osmotic stress, and after 2 days the drug is added. The concentrations of dextran and the corresponding osmotic stresses have been previously calibrated (183) (184). In this work, the dextran osmotic stresses used were 0.5 kPa (12.5 g/L), 1kPa (20.5 g/L) and 2kPa (32 g/L).

3.3.5. Capillary Western Blot

We investigated how drug and compressive stress could affect cell proliferation. Since the traditional western blot does not have sensitivity sufficient to detect the protein quantity present in a single spheroid, capillary Western blot on spheroids compressed by dextran were performed to reduce the number of spheroids needed.

At the end of the experiment the spheroids have to be lysed. 400 µL of medium was removed from every well, then the spheroids from the same experimental condition were gathered together in a Falcon tube, spun down by soft centrifugation (200 g) and washed with cold PBS three times (5 minutes each). It is important to remove most of the liquid from the spheroids: the excess liquid would risk diluting the lysis buffer in the next steps. At this point, the dried samples could be frozen at -80 ° C or lysed directly. A lysis buffer is prepared with 150mM NaCl, 50 mM Tris, 1mM EDTA, 1% Triton; 2 mM of Dithiothreitol (DTT), 2mM of NaF

(Serine/Threonine phosphatase inhibitor), Sodium Orthovanadate (Tyrosine Phosphatase inhibitor) 4mM and a tablet of complete Roche proteases inhibitor cocktail were added just before lysing. Spheroids were then incubated on ice with 200 µl of lysis buffer and vortexed regularly for 15 minutes. Then, the samples are centrifuged 5 minutes at 9500 g - 4°C and the supernatant is transferred to an Eppendorf tube. It is not possible to make a protein dosage before the western blot because the protein content of the spheroids is below the detectability threshold.

The machine Automated Western Blot from Protein Simple Company (Wes) and its corresponding preparation kits were used for a high performing capillary Western blot. It is a new automatic protein separation and immunodetection based on the application of the Protein Simple capillary immunoassay (Wes) method, a gel- and blot-free. In Wes, proteins are size separated in capillaries, where they are incubated with primary and (HRP-conjugated) secondary antibodies and finally with Luminol/peroxidase. The produced chemiluminescence is detected at multiple exposure times and automatically quantified by the Compass software.

In particular the first step was the preparation of the EZ Standard Pack reagents (3 minitubes): DTT (clear tube), Fluorescent 5X Master Mix (Pink tube) and Biotinylated Ladder (clear tube with pink pellet). Each minitube foil was pierced with pipette and 40 µL of deionized water was added into the DTT tube to make a 400 mM solution, 20 µL of 10X sample buffer (Protein Simple company) and 20 µL of prepared DTT solution were added into the Fluorescent 5X Master Mix tube, and in the end, 20 µL of deionized water was added into the Biotinylated Ladder tube.

The samples are appropriately diluted with 0.1 X sample buffer. Then, 1 part 5X Fluorescent Master Mix with 4 parts diluted lysate in a microcentrifuge tube (final concentration 0.4 mg/ml for chemiluminescence) was combined producing enough diluted sample volume required for assay. The samples were denatured in a specific hot plate at 95°C for 5 minutes.

ERK (Extracellular signal Regulated Kinase) was used as proliferation marker (185), cyclin dependent kinase inhibitor 1B (p27) was used to identify proliferation inhibition (106) and cleaved-caspase 3 was used as an apoptosis marker (185). The loading quantity was controlled by the total volume of analyzed spheroids.

Specifically, the antibodies used were: anti-rabbit ERK 1-2, anti-rabbit Phospho-ERK 1-2 (pERK 1-2) and anti-cleaved-caspase 3 from Cell Signaling Technology, and anti-rabbit p27

from Santa Cruz Biotechnology. The antibodies were diluted 1:50 with the antibodies buffer (Protein Simple company). The solution volume is chosen based on the samples number to be analyzed in the assay. At the last, was prepared the solution luminol-peroxide with the ratio 1:1, always.

Protein samples, blocking reagent, washing buffer, primary antibodies, secondary antibodies, and chemiluminescent substrate were dispensed into the assay plate according to the manufacturer's protocol. Assay plate was then loaded into the instrument, and proteins were separated into individual capillaries. Protein separation and detection was performed automatically on the individual capillaries. The data were analyzed by Compass software.

3.3.6. Analyze the Effect of Matrix Stiffness/Rigidity

We used the CytoSoft® Elastic Modulus Plates in order to study the effect of different rigidity on Gemcitabine efficacy. The plates have to be coated with an extracellular matrix protein prior cell addition: after several tests (gelatin, collagen, poly-L-lysin), we decided to use fibronectin at the concentration 5 µg/mL, the other coating proteins not giving satisfying attachment of the cells. Rigidities of 0.5 kPa, 64 kPa and ~70 GPa (glass Young modulus) have been tested.

For the control experiment with the glass, a circular cover-slip was used. The cover-slip was first cleaned by Plasma Oxygen and then placed into a 6 multiwell plate and washed with 2 mL of ethanol for 15 minutes. The ethanol was aspired and replaced with PBS that was used to wash other 3 times the glass (5 minutes each). The surface, at this point, was functionalized with 3 mL of 5µg/mL fibronectin solution (in PBS) for 2 hours, then washed with PBS two times (5 minutes each). 60000 cells (3 mL of 20000 cells/suspension) were seeded into the well and after 24 hours the cells are treated with a 10 µM Gemcitabine concentration and monitored by Cytonote 6 wells (Iprasense). This is a holographic microscope which enables time-lapses at high resolution of 6-well culture plates.

The same experimental protocol we followed with 0.5 kPa and 64 kPa rigidity plates.

3.3.7. Live dead assay

The LIVE/DEAD assay was used to estimate cell viability of spheroids treated with chemotherapeutics under osmotic stress. The LIVE/DEAD assay provides a two-color readout: the calcein AM is well retained within live cells, producing a green fluorescence (ex/em ~495 nm/~515 nm), while EthD-1 enters cells with damaged membranes and

undergoes an enhancement of fluorescence upon binding to nucleic acids, thereby producing a bright red fluorescence in dead cells (ex/em ~495 nm/~635 nm).

20 µL of the supplied 2 mM EthD-1 stock solution (Component B) were added to 10 mL of sterile, tissue culture–grade D-PBS, vortexing to ensure thorough mixing. This gives an approximately 4 µM EthD-1 solution. Then, the reagents were combined by transferring 5 µL of the supplied 4 mM calcein AM stock solution (Component A) to the 10 mL EthD-1 solution. We vortex the resulting solution to ensure thorough mixing. The resulting approximately 2 µM calcein AM and 4 µM EthD-1 working solution is then added directly to the spheroids previously washed in PBS three times for 5 minutes each.

3.3.8. Transparization protocol

The imaging of 3D cell cultures is highly challenging due to its high thickness, which results in a light-scattering phenomenon that limits light penetration. The ability to resolve and segment individual cell nuclei in 3D culture models is a necessary prerequisite to distinguish different cell subpopulations into the spheroids (186).

Here we present a protocol for nuclear clearing / transparization in spheroid models.

Essentially, we first perform the live-dead assay before following the transparization protocol: blocking the spheroids into a low-melt 2% agarose matrix and fixing with Paraformaldehyde 3.7%, permeabilisation with Triton-x (TX) and block with Bovine serum albumin (BSA) solutions, then transpirize in Glycerol solution overnight.

More specifically, the spheroids after the LIVE/DEAD assay were washed with PBS three times 5 minutes each, immobilized into an agarose pad and fixed with Paraformaldehyde 3.7% for 40 minutes and then washed again as above. At this point the spheroids immobilized into the agarose pad were gradually permeabilized: 20 minutes with PBS + 0.5% Triton-x (TX), 3 times with PBS + 0.1% TX 10 minutes and PBS + 2% BSA (bovine serum albumin) + 0.1% TX 40 minutes and then washed as above. Finally the PBS was replaced with glycerol solution in PBS (80/20) overnight at 4°C.

3.4. Results

3.4.1. The growth rate of multicellular spheroid embedded in agarose gel

The multicellular spheroids were embedded in agarose gel in order to develop a progressive controlled growth-induced compressive stress. The spheroids size evolution was followed over several days.

In a first attempt to obtain spheroids embedded in an agarose matrix, we directly mixed the cell suspension with the unpolymerized low-melt agarose matrix as suggested in the protocol of Helmlinger and colleagues (110). When the agarose polymerized, the cells remained trapped into the matrix and from each single cells or small cell aggregates a spheroid was formed. In this way, however, given the quantity of spheroids that formed in each well, it was impossible to follow the evolution of the same spheroid, so we calculated at every time point an average size from all the visible spheroids. With this method we obtained spheroids of too variable dimensions coming from aggregates with different cells number. It is obvious to understand that to evaluate a phenomenon at best you must have as few variables as possible, so we looked for a strategy to have MCSc with comparable size and to track them over time. For this reason, rather than embedding single cells as it was previously performed, a new protocol to trap the whole spheroid was developed and to track it more easily in time. The new embedding method proposed in this study is reported in the fig. 19a-b. It essentially consists in mixing a 2/3 days-old spheroid with a low melt agarose matrix at 37°C and then to induce a fast polymerization of the agarose on ice. After that the spheroid is allowed to grow under confinement for 2 more days and is then treated with the drug.

Before this protocol, we tried different strategies to embed the spheroid: at the beginning we simply covered the spheroid with low melt agarose, but that embedding was not optimal. We noticed that in most cases, the spheroid in the liquid polymeric matrix tended to sediment at the bottom of the well in less than one minute. Considering that at room temperature the agarose needs about ten minutes to polymerize, the spheroid would eventually be at the bottom when the agarose is solid. Such embedding is not fully 3D: spheroids would not to feel the same compressive stress on its entire surface. For instance, some cells escape the spheroids and start to grow in 2D on the bottom of the contacting well. In fact, the key step of this is the rapid ice polymerization necessary to trap the spheroid into the polymer matrix

before it sediments by gravity. Polymerization on ice did not affect the spheroid. The control was subjected to similar ice conditions and grew well.

Moreover, the agarose hydrogel remains a poorly characterized material, and that one has to be careful with the mechanical stress calculation when performing such experiments. Our colleagues in Lyon perform rheological measurements on the agarose hydrogel and using this calibration, we were able to extract growth-induced pressure curves for embedded spheroids. In particular they found a rough linear increase of normal stress applied onto the spheroid during growth as shows the figure 20.

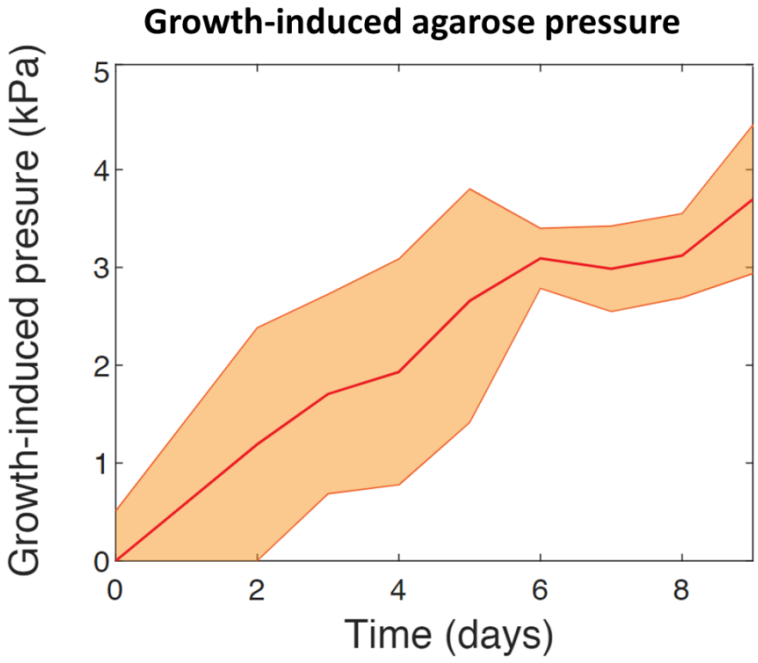

Figure 20. Growth-induced pressure as a function of time *extracted through the growth of spheroids in 1% low-melt agarose. Mean values are plotted, shading corresponding to ±SD over N ≥10 spheroids.*

The figure 21a shows the growth trend in 8 days of spheroids growing in 0.5% (red line) and in 1% (blue line) of agarose versus their correspondent control spheroids (black line). We report in this graph the spheroid's mean radius normalized to initial radius as a function of time in days. The increase of agarose matrix concentration progressively reduces spheroid growth. A representative picture of an agarose 1% compressed spheroid and its size is reported in the figure 21b (right): it can be seen how the size of the spheroid is smaller than its control (20b – left). In particular compared to the control, a spheroid under 7 days of 1% agarose compressive stress grows about 40% less. The results are consistent: the errorbar is calculated with the Standard Deviation (SD) of at least 10 experiments ($N \geq 10$).

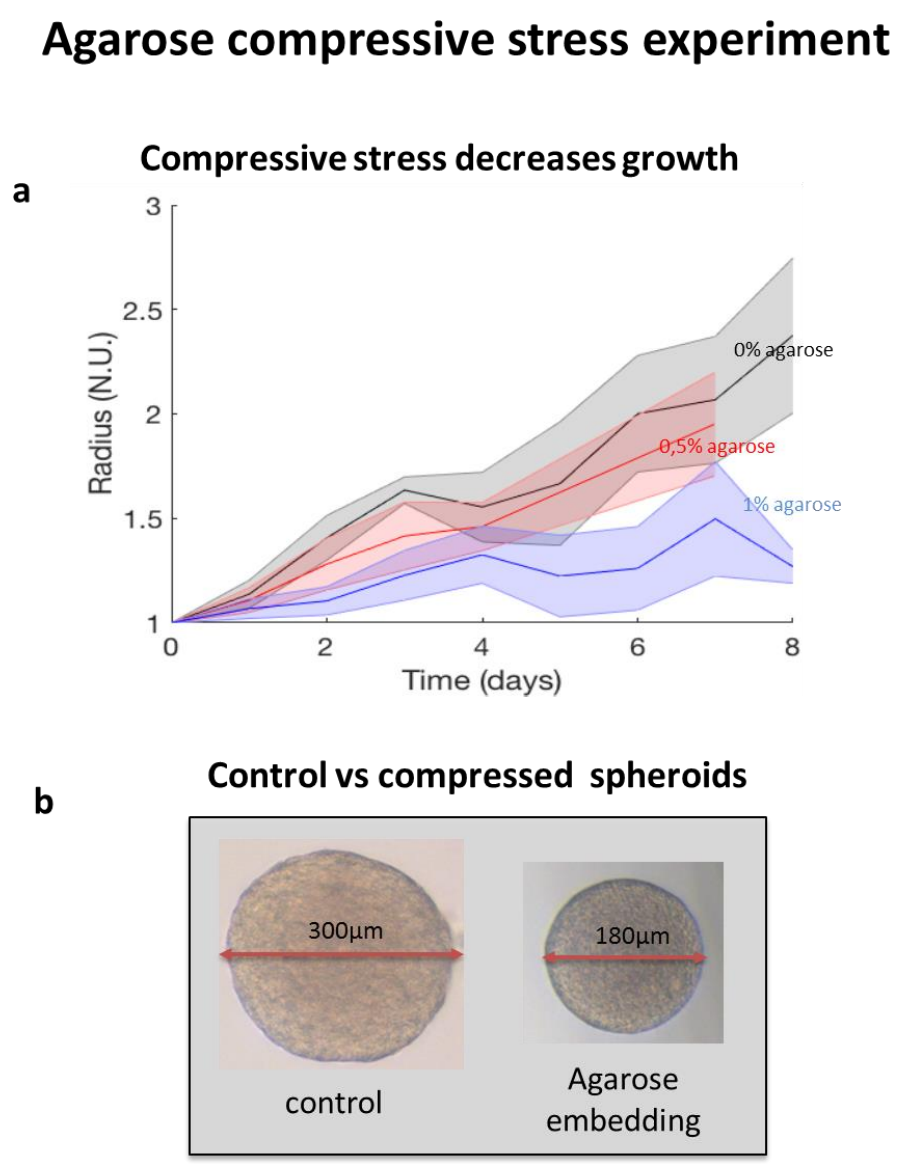

Figure 21. Compressive agarose embedding stress decrease spheroids growth. *(a) agarose 1% (red) and 0.5% (blue) embedded spheroids growth curves versus their control (black) – x axis : time (days) ; y axis : unit normalized mean radius - Mean values are plotted, shading corresponding to ± SD over N ≥10 spheroids. b) Representative size of control and agarose embedded stressed spheroids after 7 days under compression.*

3.4.2. Dextran osmotic effect on multicellular spheroid growth rate.

In order to exert a mechanical stress, a biocompatible polymer, Dextran (MW = 100 kDa) was added to the culture medium after the formation of the spheroids. Unlike more physiological osmolytes, such as glucose or ions (Na+, Mg2+, etc), dextran macromolecules are not internalized by cells, and do not infiltrate the intercellular space of spheroids if large enough (several tens of kDa) (107). It has been demonstrated in a previous paper that dextran does not penetrate the spheroid. Accordingly, the same osmotic effect on the spheroid growth is shown with a dialysis membrane interposed between the spheroid and the dextran molecules (169).

The effect we observe is not a direct osmotic effect on single cells, as is often described in the literature for high osmolarity shocks. The compressive stress can be seen as a network stress that tends to reduce the volume occupied by the MCS (106). In this regime, dextran is not affecting component concentration of single cell but rather of spheroid. Thus, they exert a constant osmotic stress onto the whole spheroid and induce an efflux of water from the spheroid, probably from the matrix components (107) (171). The stresses used are 0.5 kPa, 1kPa and 2kPa and it is worth noting that these are small stresses even 5 kPa is a rather small stress and it correspond to the osmotic pressure exerted by 1 mM NaCl.

Interestingly, for a stress of 5kPa, the spheroids decrease their volume: some cells probably die because of the high dextran concentration.

In the figure 22a we show the evolution of spheroids size under compressive osmotic stress of 1kPa (red line) and 2kPa (blue) in comparison with their control (black line). The results are comparable to those in agarose: in both cases, an increase of compressive stress reduces proportionally the growth rate of multicellular spheroids. A representative picture of a 1kPa osmotically-compressed spheroid and its size is reported in the figure 22 b (right): it can be seen how the size of the spheroid is smaller than its control (22 b – left). In particular compared to the control, a spheroid under 7 days of 1 kPa dextran compressive stress grows about 33% less.

It is important to underline that, although in this case we have obtained an inhibition of the growth of the spheroid under stress, we are dealing with a different stress than the one agarose-induced. In particular, both of these are compressive stresses, but the one mediated by agarose is growth-induced, while the dextran is osmotic and constant. We observed that osmotically compressed spheroids restricted cell proliferation to the outermost layers. The results are consistent: the errorbar is calculated with the SD of at least 10 experiments ($N \geq 10$).

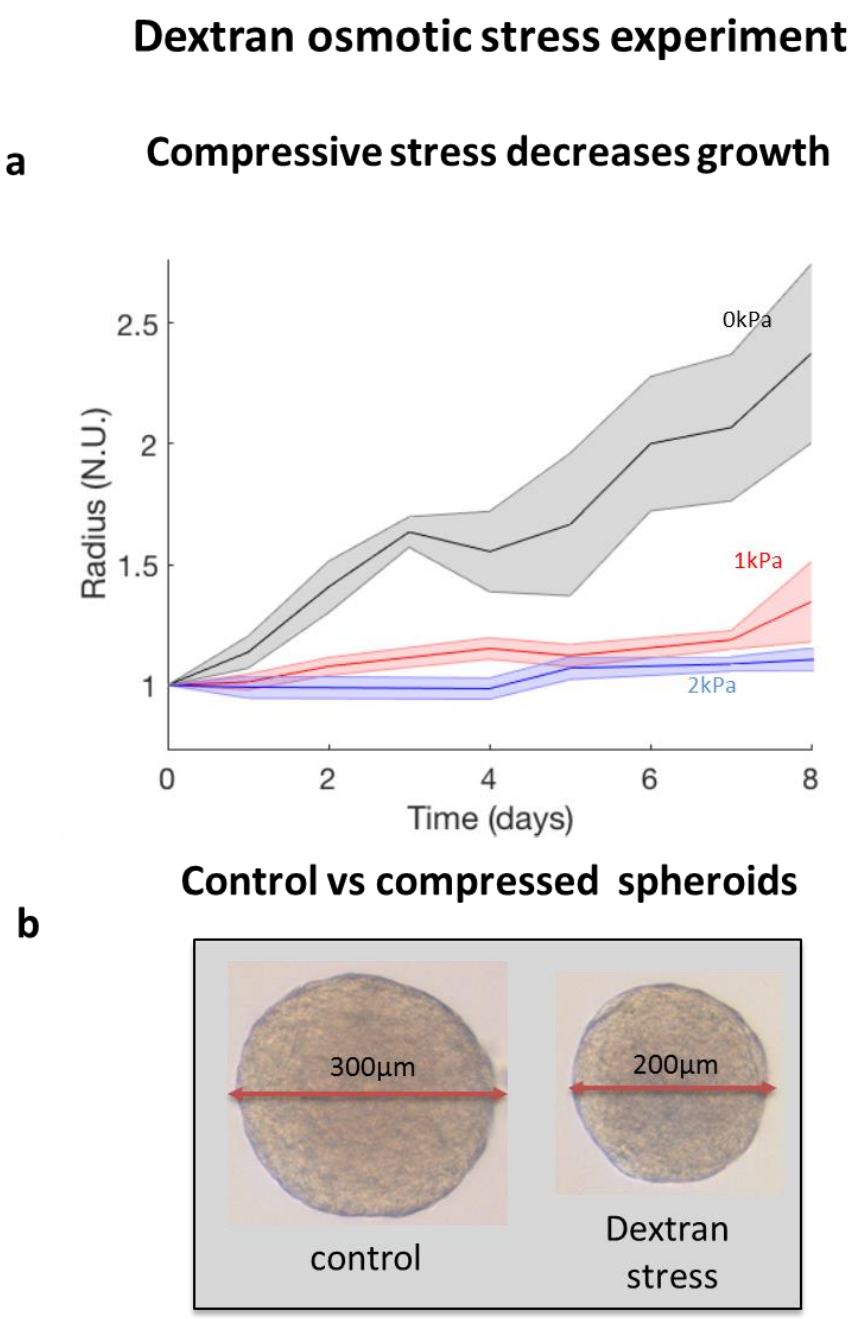

Figure 22. Osmotic dextran stress decrease spheroids growth. *(a) osmotic dextran 1kPa (red) 2kPa(blue) stressed spheroids growth curves versus their control (black) - x axis : time (days) ; y axis : unit normalized mean radius - Mean values are plotted, shading corresponding to ± SD over N ≥10 spheroids. b) Representative size of control and osmotic stressed spheroids 1kPa after 7 days under compression.*

3.4.3. Cryosection and immunofluorescence biological characterization

In addition we performed immunostaning of paraffin-embedded spheroids section to evaluate the compressive stress effect on the proliferation and cells death (figure 23). We analyzed the

spheroid grown under 1% agarose and 1kPa dextran compressive stresses for 4 days and their corresponding control. To label cell division we used the antibody against Ki67 and to label apoptosis the antibody against cleaved-caspase-3. As can be seen in the figure 23, into the spheroid there is a gradient of cell proliferation from the inside out but this gradient is reduced under compressive stress. Compressive stress reducing cell proliferation and subsequently S-phase entry. Moreover, we do not observe any significant apoptosis at the surface or in the inner layer of the spheroid where the compressive stresses are exerted.

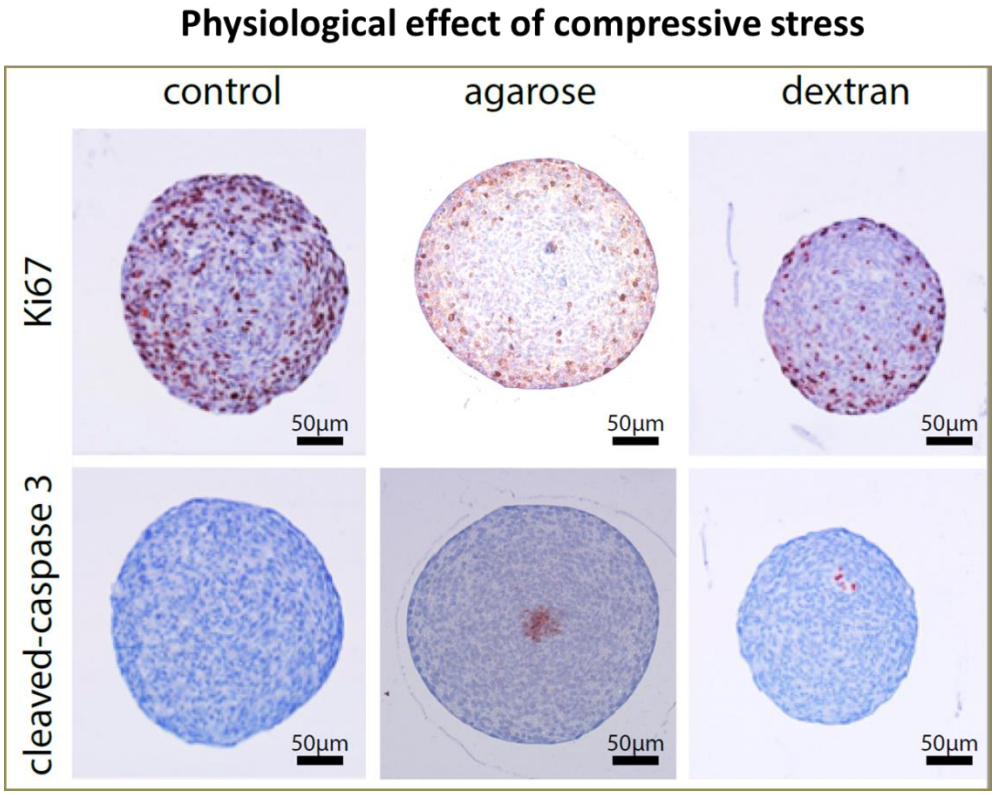

Figure 23. Effect of stress on the distribution of proliferation and apoptosis. *Cryosections and immunofluorescence of the spheroids are used to label the cell divisions [antibody against Ki-67 purple- first line] and apoptosis [antibody against cleaved Caspase-3 in dark red – second line)]. (Left) Spheroid grown in a normal medium for 4 days. (Middle) Spheroid grown with a stress of1% of agarose (right)and 1 kPa dextran for 4 days.*

3.4.4. A compressive stress reduces proliferation of pancreatic cancer multicellular spheroids: capillary Western blot results.

We investigated whether the reduced growth rate due compressive stress affected proliferation. Since the sensitivity of a traditional western blot requires a "considerable" amount of proteins (typically corresponding to about 20 spheroids), we decided to perform a capillary Western blot analysis, for which the protein quantity of about five spheroids is sufficient. This is certainly a huge gain of time; practically in the time of a single experiment

we could get 3 independent replicates. The capillary Western blots were performed on spheroids compressed by Dextran. Capillary western blotting is a new automatic protein separation and immunodetection based on the application of the Protein Simple capillary immunoassay (Wes) method, a gel- and blot-free. Wes requires less sample, antibody and time to run than conventional western blot assay. The machine Automated Western Blot from Protein Simple Company (Wes) and its corresponding preparation kits were used for a high performing capillary Western blot. In Wes, proteins are size separated in capillaries, where they are incubated with primary and (HRP-conjugated) secondary antibodies and finally with Luminol/peroxidase. The produced chemoluminescence is detected at multiple exposure times and automatically quantified by the Compass software. The chemoluminescent signal can be displayed as an electropherogram or as a virtual blot-like image. The electropherogram shows the intensity (per second) detected along the length of the capillaries, and shows automatically detected peaks, that can be quantified by calculation of the area under the curve (AUC).

ERK was used as proliferation marker. ERK is a mitogen protein kinase involved in many cellular programs, such as cell proliferation (185). The ratio phospho-ERK to total ERK is a marker of cell survival and proliferation. The cyclin dependent kinase inhibitor 1B (p27) was used to identify proliferation inhibition which controls the cell cycle and progression in G1 (106) and the cleaved-caspase 3 was used as an apoptosis marker (185). Generally in the western blots proteins such as actin, tubulin or histone H3, etc. are used as loading control, but in our case they could all change under pressure. So we tried to get around the problem loading a similar total volume of cells assuming cell density was roughly constant. For instance, we loaded 5 spheroids of the control of volume V_0, and 10 spheroids of dextran condition of volume $V_0/2$.

We report in figure 24a the assay plate and manufacturer's loading protocol. In the first line the samples are loaded, and the same sample is repeated every time it has to be analyzed with a new antibody, the sample will then be found in the column corresponding to the antibody with which it must be checked. The primary antibodies are loaded in the C row, the secondary ones in the D row and the luminol-peroxide in the E line.

It is essential to calibrate well the sample dilutions to remain within the instrument's range of detectability. Often the same sample dilution cannot be used with different antibodies because the protein expression is different: for example, in comparison to p27, for the same sample, pERK and ERK have to be diluted 3 times.

Figure 24b shows the pERK/ERK and p27 protein expression in the osmotic compressed spheroids compared with their control (dashed line).

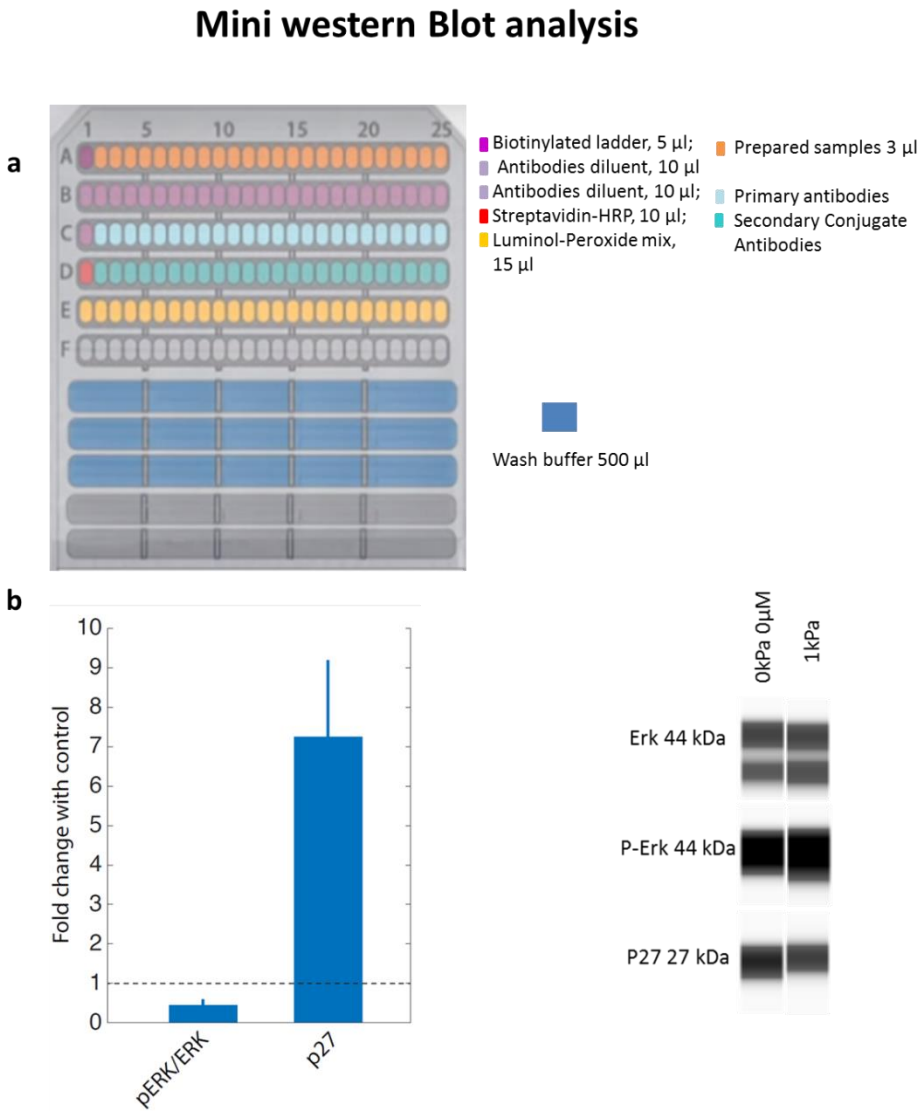

Figure 24. Capillary Western blot analysis (Wes) : *(a) assay plate and manufacturer's loading protocol ; (b) p-ERK/ERK and p27 expression into dextran osmotic compressed spheroids.*

A decrease of pERK/ERK and an increase of p27 expression in osmotically stressed spheroids suggests that the reduction in growth rate of compressed pancreatic cancer spheroids is accompanied with/is the consequence of a decrease in single cell proliferation within the spheroid, consistent with the immunostaining.

3.4.5. What happens to the efficacy of a proliferation targeting drug when the proliferation is reduced by compressive stress?

We treated freely growing multicellular spheroids with gemcitabine to investigate the nominal effect of this chemotherapeutic. Perhaps not surprisingly, we found that spheroids subjected to 10µM gemcitabine decreased in size (Fig. 25 a). The decrease was apparent after an average of 1 day post drug addition, consistent with the fact that only S-phase cells are sensitive to the drug.

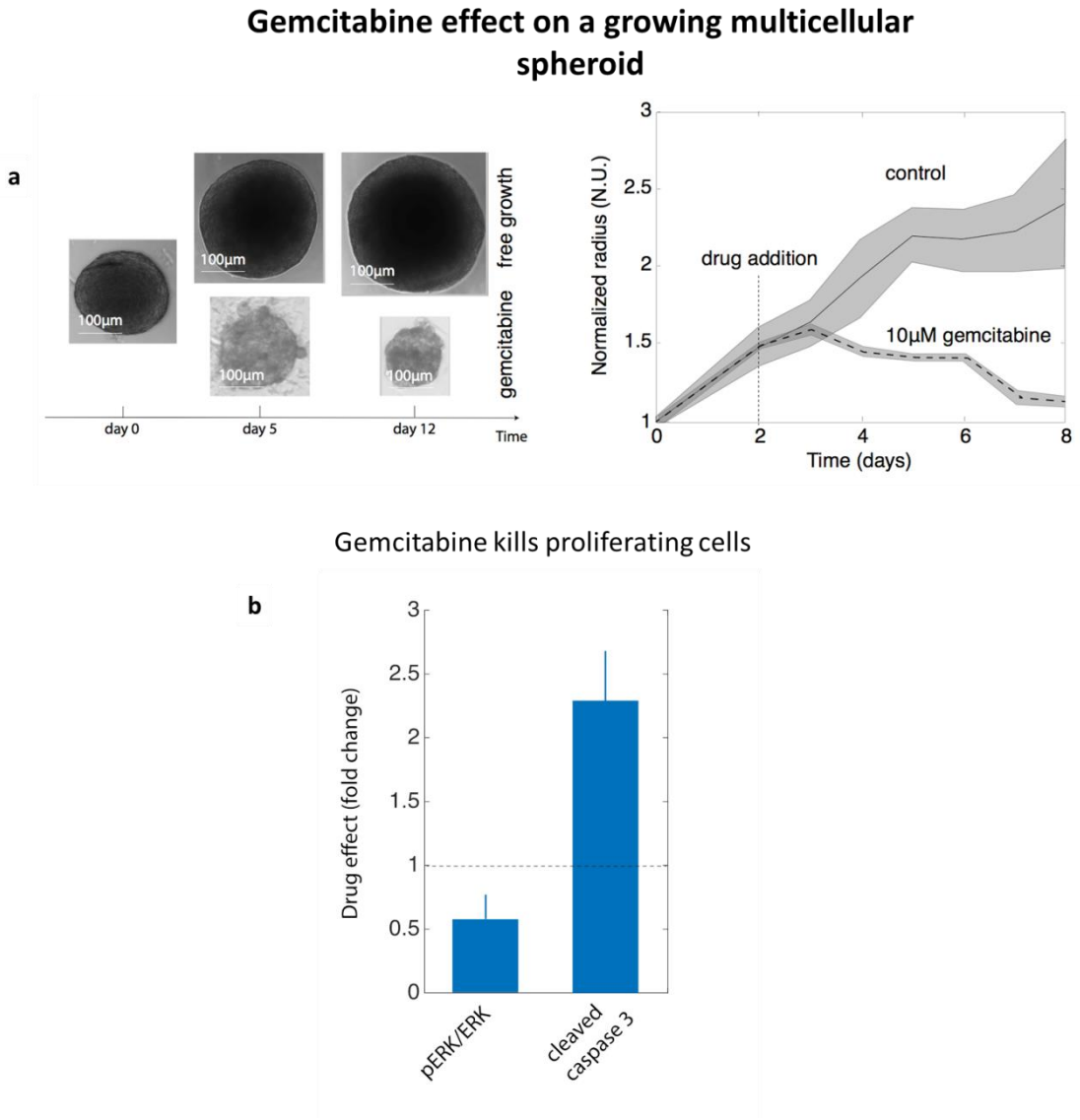

Figure 25. Effect of gemcitabine on the free growth of spheroids*. a. Representative pictures of freely growing pancreatic spheroids and exposed to gemcitabine (left). Drug was added after two days of growth. Growth quantification over time. Mean values are plotted, shading corresponding to ± SD over N ≥ 10 spheroids (right). b. capillary Western blot analysis of spheroids. Phosphorylated form of ERK (pERK) normalized to total ERK is used as a proxy for the amount of cell proliferation, and cleaved-caspase 3 as a proxy for the amount of dying cells. The data under gemcitabine treatment are normalized to the control.*

We performed capillary western blots to investigate the changes in proliferating and dying cells under gemcitabine treatment. We measured the ratio between a phosphorylated form of ERK (pERK) over total ERK as a proxy for cell proliferation and the amount of cleaved-

caspase 3 as a proxy for cells undergoing programmed cell death (Fig. 25 b). A considerable increase in the cleaved-caspase 3 expression in Gemcitabine treated spheroids tells us that the drug is working with its maximum efficacy increasing cellular apoptosis. We observed that, as the amount of proliferating cells decrease under drug treatment, the amount of dying cells increased by roughly, in agreement with gemcitabine preferentially killing proliferating cells..

We next sought to investigate the impact of compressive stress pressure on the efficacy of Gemcitabine. After compressing the cells for 2 days, either mechanically with agarose or osmotically with Dextran, we treated the spheroids with 10µM Gemcitabine, and measured the evolution of the spheroids' size over time (figures 26a and 26b). We compared the results with the correspondent controls: free spheroid and free spheroid + Gemcitabine.

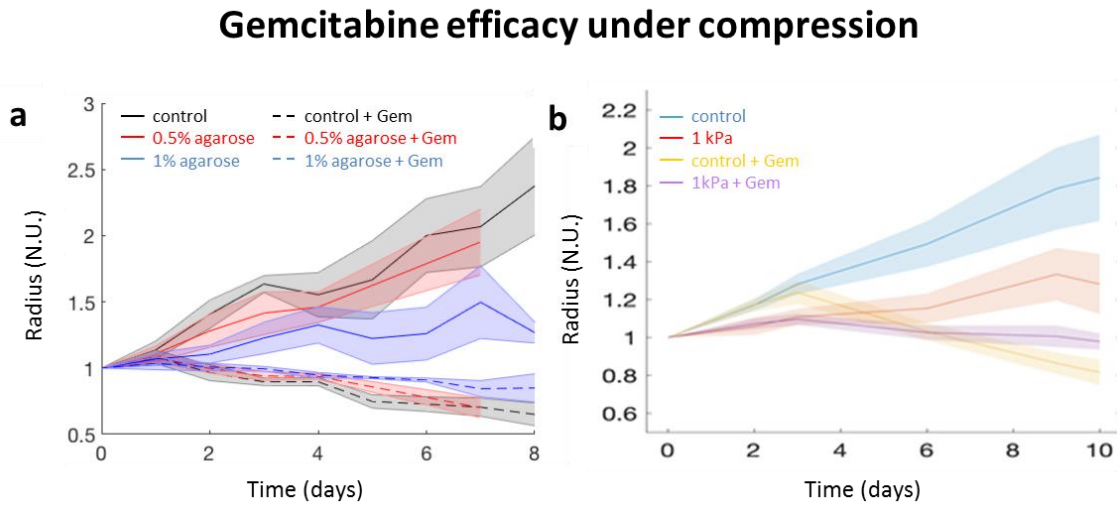

Figure 26. (a) Compressive agarose embedding stress decrease spheroids growth and the chemioterapic drug efficacy. *agarose 1% (red) and 0.5% (blue) embedded spheroids growth curves versus their control (black) ; Gemcitabine (Gem) 10 µM efficacy into agarose 1% (red) , 0.5% (blue) embedded and control spheroids (black) – complexive chart on the left – x axis : time (days) ; y axis : unit normalized mean radius.* ***(b) Osmotic dextran stress decrease spheroids growth and the chemioterapic drug efficacy****. Osmotic dextran 1kPa stressed spheroids growth curves (red) versus their control (blue); Gemcitabine 10 µM efficacy into dextran 1 kPa (osmotic stressed (violet) and control (yellow) spheroids— x axis: time (days); y axis: unit normalized mean radius.*

We found that the drug was less efficient under compressive stress: compressed spheroids are less sensitive to the drug than unconfined/uncompressed ones, their size reducing much slower as compression increased.

Figure 27a shows the agarose-embedded spheroids evolution at 6 time points: Time 0 (the day when the agarose mechanical stress is applied), 1 day, 4 days, 7 days, 8 days, 12 days. There are 4 conditions: control, control + Gemcitabine, 1% agarose embedding and 1% agarose embedding + Gemcitabine. Two cases are shown for the 1% agarose embedding + Gemcitabine: the case where the spheroid is still fully embedded in the agarose and the case

where the spheroid's size decreased below the initial size at embedding and is not confined anymore.

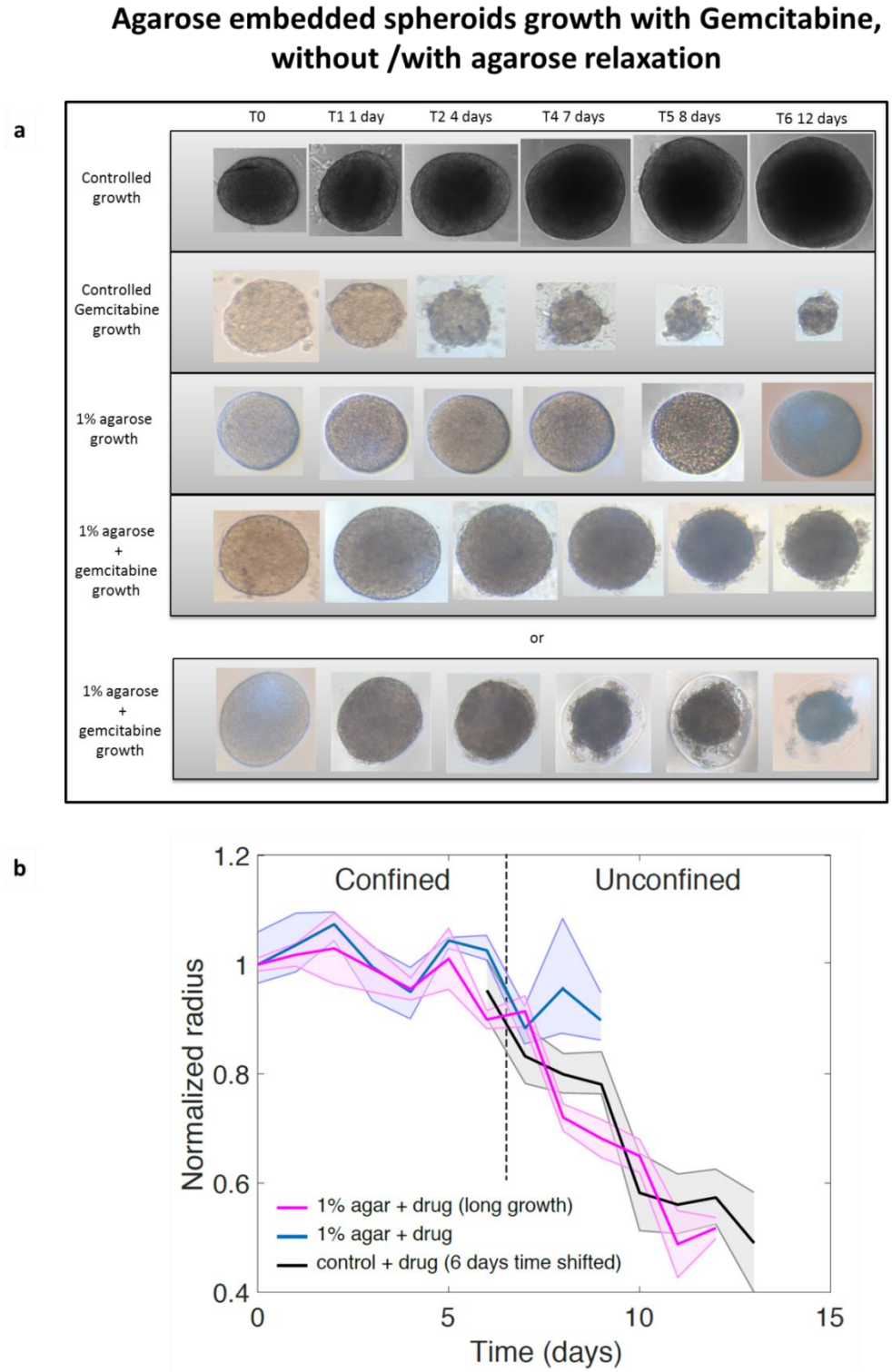

Figure 27. Agarose embedded spheroids + Gemcitabine evolution. *(a) microscope pictures of controlled, controlled + Gemcitabine, 1% agarose and 1% agarose + Gemcitabine spheroids growth without agarose relaxation (fourth row) and with agarose relaxation (fifth row) ; (b) size evelotion of controlled + Gemcitabine spheroids 6 days shifted (black), 1% agarose + Gemcitabine spheroids without agarose relaxation (blue) and 1% agarose + Gemcitabine spheroids with agarose relaxation (pink). Beyond the dashed line the spheroids are not confined by agarose.*

So, in the first case the agarose exerts on the spheroid a growth induced compressive stress as explained above but, in the second case, at some point, such stress disappears. After relaxation, it seems that the spheroid resumes its normal proliferative capacity and when this happens Gemcitabine regains its nominal efficacy. We consider as nominal the efficacy that Gemcitabine has with a spheroid not subject to any compressive stress (control + Gemcitabine condition). In the figure 27b we compared with the respective control shifted for 6 days (black line) the two conditions with (pink line) and without (blue line) agarose relaxation. The dashed line indicates the time point at which the confinement relaxes on average. After 5-6 days of drug treatment under confinement of spheroids which did not grow much initially, the reduction of the radius was such that the spheroids were not confined anymore and as such did not experience any compressive stress. The behavior with Gemcitabine of the embedded spheroid in the case of agarose relaxation is totally comparable with the free spheroid and in agreement with our hypothesis. Quiescent cells would re-enter the cell cycle, proliferate faster, and consequently die faster. This is what we found experimentally: a slow initial death rate during compression, followed by a faster one in the unconfined phase. Moreover, it is interesting to note that this experiment suggests that the proliferative capacity of the spheroid, reduced by compression, is perfectly reversible. This mechanism makes two hypothesis: If the efficacy of a proliferation-based chemotherapeutic is decreased because of a mechanical modulation of cell proliferation, then the observed modulation of efficacy (i) should not depend on the type of mechanical stress applied, but rather on the fact that mechanical stress could decrease cell proliferation (as we demonstrated with Dextran) and similarly, (ii) should not depend on the type of drug used, but rather on the fact that the chemotherapeutic drug targets proliferating cells.

3.4.6. Agarose embedding spheroid growth with Docetaxel

Our results suggest that the mechanical stress decreases the efficacy of the drug by acting on specific signaling pathways linked with cell proliferation. Then, probably the effect that we see is not Gemcitabine-dependent, but another drug acting on proliferation, as Gemcitabine, could also see its efficacy decrease as a function of mechanical stress. We tested this prediction with docetaxel, acting during mitosis by stabilizing mitotic spindle.

First, we made a comparison of the efficacy of Gemcitabine, Docetaxel and the specialized nanocarrier SPNs carrying Docetaxel (fig. 28). In this *scenario* we decided to test the SPNs, because, as we mention above, is well-known their potential to target solid tumors (182).

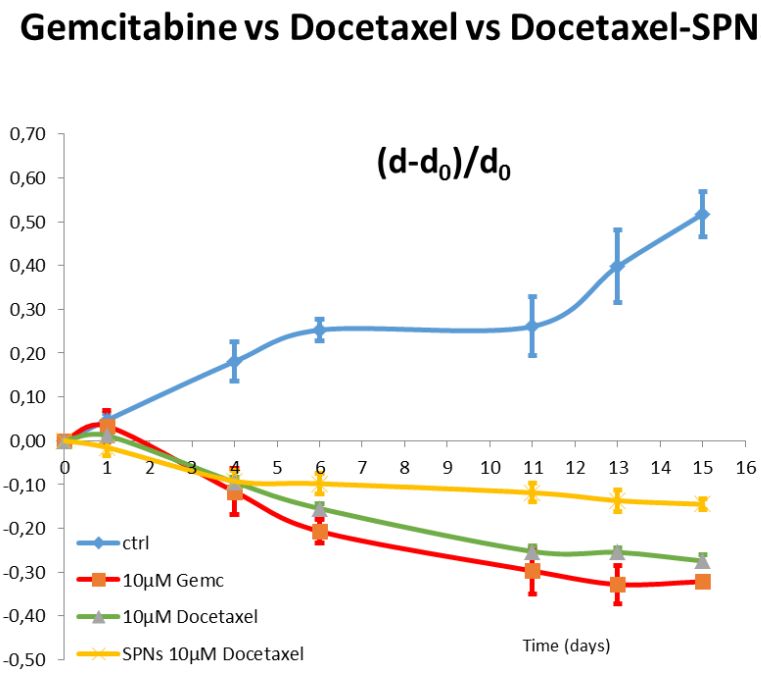

Figure 28. Gemcitabine vs Docetaxel vs Docetaxel-SPNs. *Control spheroids (blue line), Gemcitabine treated spheroids (red line), docetaxel treated spheroids (green line) and SPNs-Docetaxel treated spheroids (yellow line).*

In the treatment of pancreatic cancer, Gemcitabine certainly appears to be more effective, although Docetaxel is well known as second-line chemotherapy on PDAC cells (180). The nanoconstructs are spherical in shape with a characteristic diameter of about 100 nm, which is ideal for targeting solid tumors via the enhanced permeability and retention (EPR) effect. However, from the analysis of the spheroid diameter, the particles would seem to be the least effective, but given their adhesive capacity, they tend to release big quantity of the drug in the innermost part of the spheroid destroying not only superficial cells but also internal cells. This implies that a quantification of the evolution of the spheroid radius is not sufficient to quantify the real effect of these nanoconstructs. These are only preliminary results that should be further explored.

Finally, we sought to investigate on our second hypothesis, explained above, i.e. the effect of mechanical on the drug efficacy should not depend on the type of drug used, but rather on the fact that the chemotherapeutic drug targets proliferating cells.

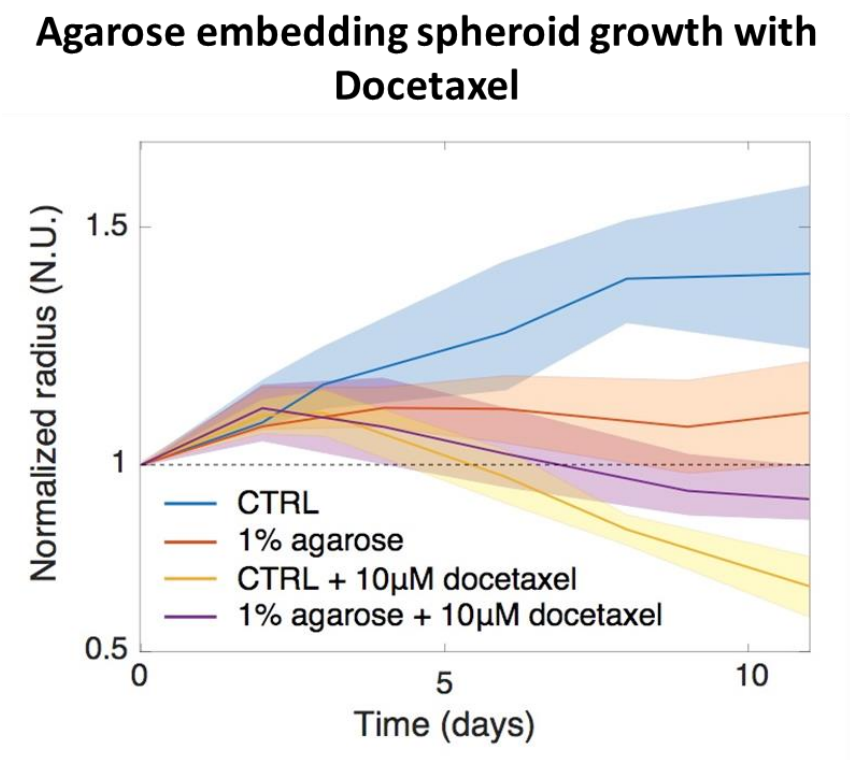

Figure 29. Experimental consistency demostration of the agarose embedding experiment with Docetaxel.

We confined spheroids in 1% agarose gel similarly to what we previously described, and treated the compressed spheroid after 2 days under mechanical compression with 10 µM docetaxel. Preliminary data suggest that indeed mechanical compressive stress of agarose reduces the efficacy of this other chemotherapeutic drug, docetaxel, consistent with our prediction (fig 29).

3.4.7. Biological Characterization: Clearing of spheroids by transparization and live-dead assay

We developed an imaging strategy to compare the effect of Gemcitabine and docetaxel, and to localize SPNs: the transparization assay. Along with this, we used a LIVE/DEAD assay to estimate the cell viability into the spheroids. In particular we applied first the live/dead assay because the transparisation test involve cell fixation and therefore cell death.

The LIVE/DEAD assay provides a two-color fluorescence cell viability assay that is based on the simultaneous determination of live and dead cells with two probes that measure

recognized parameters of cell viability intracellular esterase activity and plasma membrane integrity. The molecular probes are calcein AM and ethidium homodimer (EthD-1). The calcein is well retained within live cells, producing a green fluorescence, while EthD-1 enters cells with damaged membranes and undergoes an enhancement of fluorescence upon binding to nucleic acids, thereby producing a bright red fluorescence in dead cells.

The imaging of 3D cell cultures is highly challenging due to high thickness, which results in a light-scattering phenomenon that limits imaging. Unfortunately, light scattering prevents confocal imaging beyond a typical depth 50 μm in tissues (186). The ability to resolve and segment individual cell nuclei in 3D culture models is a necessary prerequisite for performing high spatial resolution measurements and quantitation of microenvironment effects: in other hands should be possible to distinguish different cell subpopulations into the spheroids.

Herein we present a protocol for cell clearing / transparization in spheroid models (full explanation in the session *Transparization protocol* of the Methodologies).

The figure 30 shows the resulting confocal pictures from a control, a Docetaxel treated and a Docetaxel – SPNs (DTXL-SPNs) treated spheroid (fig. 30a).

We are perfectly able to recognize live cells from dead cells within the spheroid but it is not possible to make a real quantification of the dead cells: dead cells would hardly stay confined in the spheroid. Anyway, live/dead assay suggests that cell death is located at the inner area for the control, at the periphery for the Docetaxel treated and in both areas for the DTXL-SPNs treated spheroid. This is consistent with the fact that spheroids are stratified with an outer rim of proliferating cells that is the chemotherapeutic target. Moreover, the particles, as it explained above, given their adhesive capacity, tend to release big quantity of the drug in the innermost part of the spheroid destroying not only superficial cells but also internal cells.

The figure 30b is a confocal bright-field picture from a cleared spheroid: it is possible to distinguish the nuclei from both inner and peripheral spheroid areas, and the genetic material can even be seen inside (small white dots). This means that method has been successful: cell membranes have been completely degraded, and light scattering phenomenon eliminated (186).

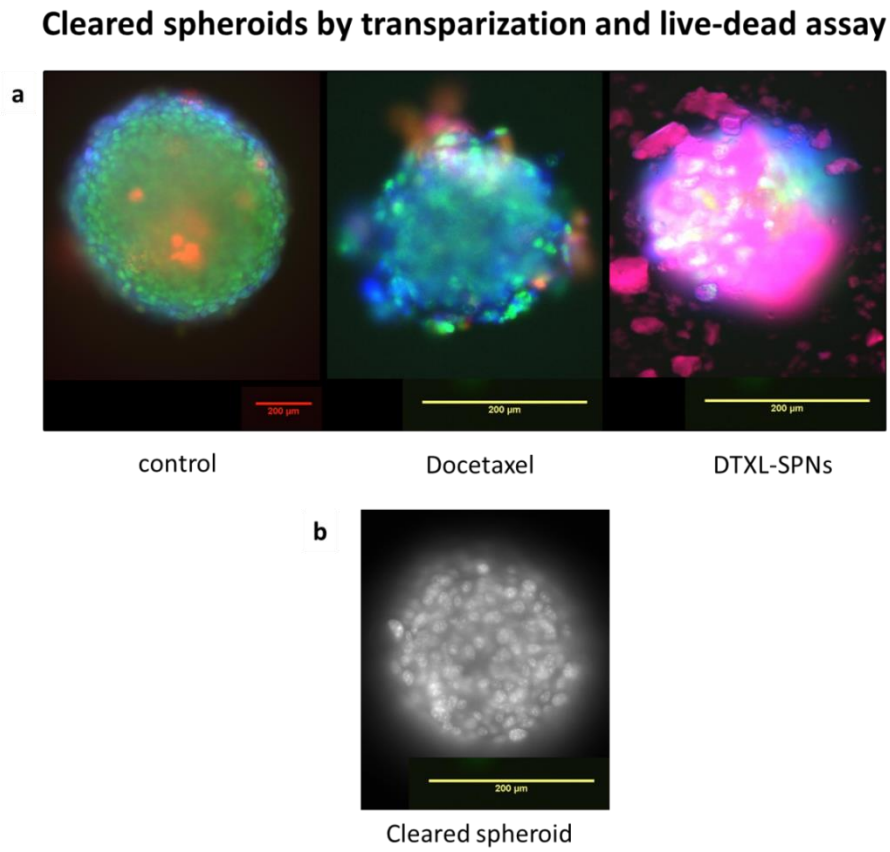

Figure 30. Confocal pictures of cleared spheroids by transparization and live dead assay. *(a) live-dead / transparization assay result from control, Docetaxel treated and Docetaxel – SPNs (DTXL-SPNs) treated spheroids. In green living cells, in red dead cells, in blue cells nuclei and in Magenta DTXL-SPNs. (b) bright-field picture of cleared spheroid by transparization assay protocol.*

Quantitation of microenvironment effects in 3D cultures is essential, as cells within tissues may have different drug responses. Herein we present a protocol for high-throughput nuclear segmentation in spheroid models. This is an integrated tool to distinguish and quantify the different spheroid cellular subpopulations.

3.4.8. Effect of Substrate Stiffness/Rigidity on cells drug sensitivity.

Cells reside in various matrix stiffnesses throughout the body. Tissue culture plastic wares have an elastic modulus of 1 X 107 kPa whereas tissues/organs have much lower values ranging from 0.1 to 100 kPa (187) (188) (189) (190) (191) (192) (193) (194) (195) (bones excepted). Cells in the body interact with their local 3D microenvironments, which can vary based on tissue location and disease states. The CytoSoft® Elastic Modulus Plates were used to tested the Gemcitabine efficacy in more relevant in vitro cell models: these substrates more closely represent native tissue rigidities (0.2 – 64 kPa). We investigated the role of substrate stiffness as an additional source of mechanical stress that can modulate cell proliferation.

The plates must be coated with an extracellular matrix protein prior to cell addition. For this reason we tested the cell adhesion proteins poly-L-lysine, gelatin, collagen and fibronectin (fig. 31a). Cells growing on all substrata but fibronectin seem to create aggregates, which then limit the 2D assay we wish to investigate; for this reason, we choose to use fibronectin as a coating of the plates.

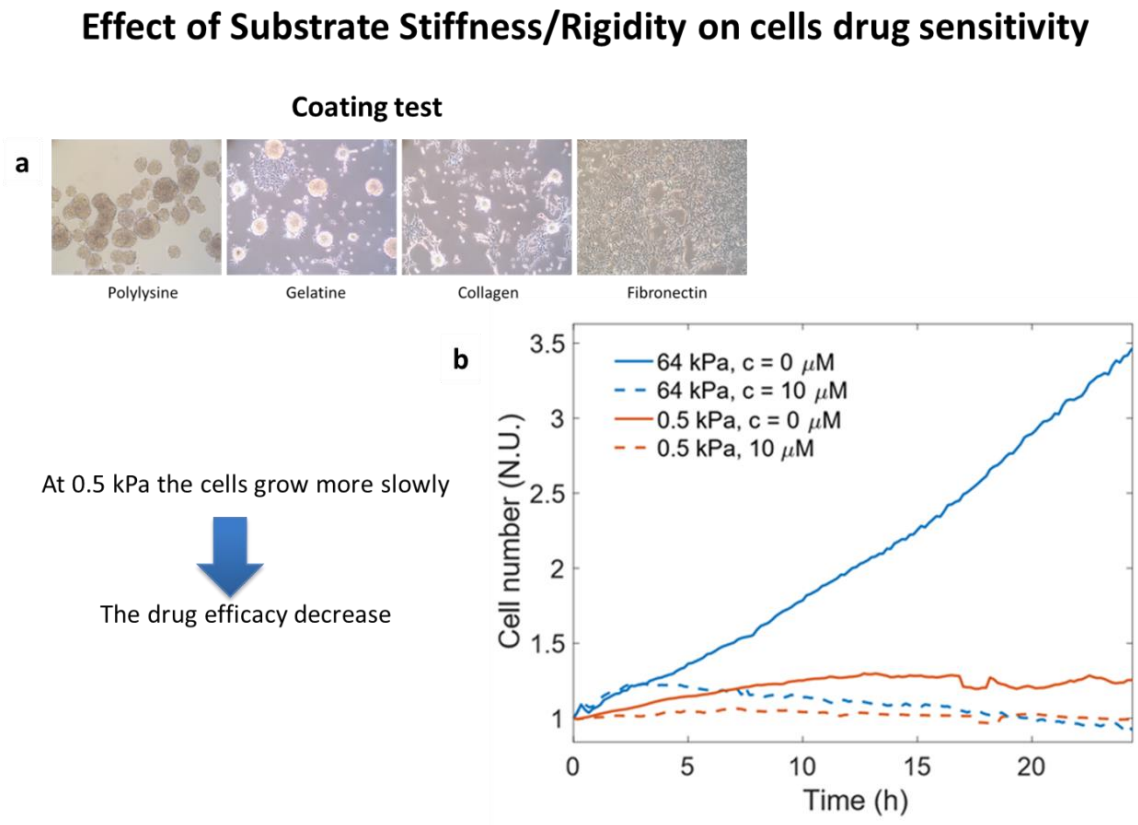

Figure 31. Effect of Substrate Stiffness/Rigidity on cells drug sensitivity. *(a) Rigidity plate coating test with Polylysine, Gelatine, Collagen and Fibronecti ; (b) Cytonote time lapse analysis of the Gemcitabine efficacy at 0.5 kPa and 64 kPa of rigidity.*

We analyzed the growth of cells with two different stiffnesses (64kPa and 0.5 kPa) and evaluated the efficacy of Gemcitabine 10µM (fig 31 b). At 0.5 kPa the cells seem to grow more slowly than at 64 kPa. This is accompanied with a decrease in the efficacy of drug. This set of data is consistent with the fact that mechanical stress can affect the efficacy of a proliferation-based chemotherapeutics by modulating the very cell proliferation index.

Using the substrate stiffness/rigidity stress we have confirmed once again the previous result: the mechanical stress influences cell proliferation and therefore chemotherapy activity.

3.4.9. A mathematical model perfectly predicts the effect of compressive stress on drug efficacy.

Pietro Mascheroni, a theorist collaborator, developed a mathematical framework to model the chemotherapeutic efficacy under dextran and agarose compressive stresses (see insert for detailed calculation). In brief, we consider a spheroid as a stratified three-dimensional structure, with cells proliferating in the outer rim, and quiescent in the center.

We assume that the total number of cells in the spheroid varies according to cell proliferation, drug-induced death and apoptosis. In particular, cell proliferation is exponentially distributed over the spheroid radius, with a characteristic length L. Cell death induced by the drug acts on proliferative cells, whereas apoptosis takes place over the entire spheroid radius. We observed that cell death induced by the drug is not instantaneous. Indeed, in order for the drug to be effective the cells must be in the proliferative state. The waiting time for the cell to enter the proliferative phase can be assumed to be exponentially distributed, giving a delay for the drug to be effective of about 24 hours. Assuming (i) that the characteristic proliferation length L is smaller than the spheroid radius and (ii) that the experiments are performed over a timescale in which apoptotic death is not fully developed, we can write the temporal variation of the spheroid radius R as

$$\dot{R} = g - d\frac{g}{g_0}$$

where g is an effective growth rate (including the early effects of cell apoptosis) and d is the death rate induced by the drug, including the time delay (for more details, the reader is referred to the insert). In writing this equation we assumed that d is independent of the external pressure applied to the spheroid. The dependence on pressure is only considered for the growth rate g which takes the value g_0 in control conditions (i.e. no compression and no drug).

We use the experimental data to fit the various parameters of the model: $g=g_0$ is fitted through the control experiment, $g=g_c$ is obtained from the spheroid growing under compression, and the drug induced death rate $d=d_0$ is calibrated when the drug is administered to the spheroid in the absence of pressure. Using the fitted parameters, we use the model to predict the combined effect of compression and drug action, and find a good agreement with the experimental data (Fig. 32).

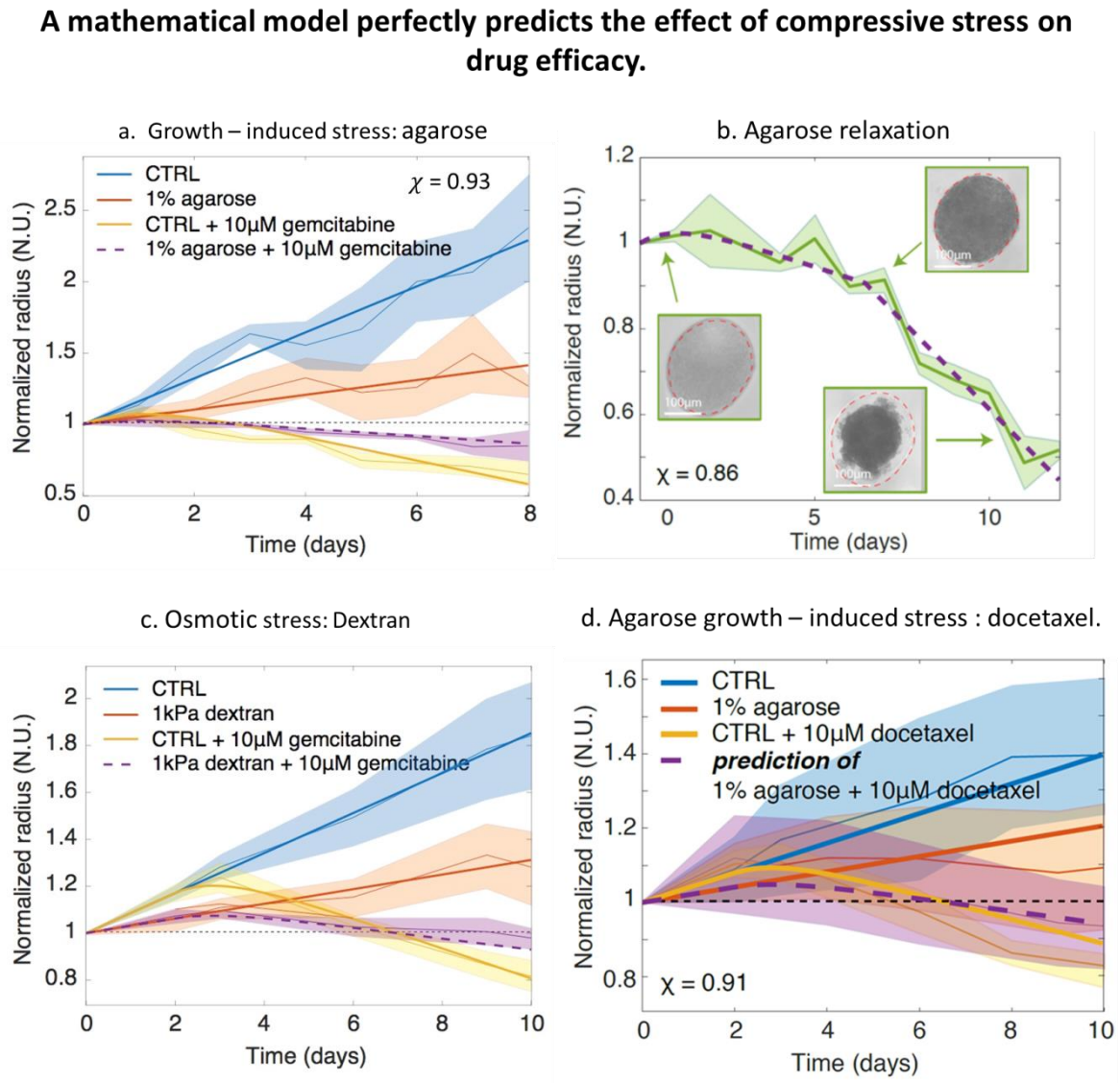

Figure 32. Model results for the growth of spheroids under different external conditions*. Model calibration is represented by solid lines, whereas the dashed line represents model prediction.* ***(a) Agarose embedding stress; (b)*** *Spheroids exposed to gemcitabine can eventually be smaller that the initial inclusion size, and are subsequently unconfined (pictures in inset). The model is able to capture the* ***effect of gemcitabine*** *in this case****, switching from efficacy of confined cells before 6 days, to efficacy of unconfined cells after 6 days. (c) dextran compressive constant stress.(d) agarose confined spheroid growth with docetaxel*** *In all cases, mean values are plotted, shading corresponding to ± SD over N ≥ 10 spheroids.*

This model was able to predict the effect of compressive stress on Gemcitabine drug efficacy into mechanical agarose compression (32a), also in the case of agarose relaxation (32b). Moreover it predicted the spheroids growth under osmotic Dextran compression (32c) and confirmed the effect of the other chemotherapy that we tested, such as docetaxel (figure 32d).

The excellent prediction of the model with the experimental data is consistent with a mechanism where mechanics would decrease chemotherapeutic efficacy through a modulation of cell proliferation independent of stress and the drug used (in the model we

assume that effect of the drug effect and the mechanical stress are not coupled). The rigidity/substrate effect experiments cannot be fitted with this model but in any case seem to be consistent and confirm what we reported with the other stresses.

3.5. Conclusions and perspectives

3.5.1. Conclusions

In this work we investigated the impact of mechanical stress in the efficacy of drug treatment and we arrived at three main conclusions.

1. **Reduction in growth rate of compressed pancreatic cancer spheroids.**
   We performed a new strategy to embed whole PDAC spheroid in an agarose matrix. The agarose represents a good candidate to mimic the elastic stroma behavior during the tumor progression, because such as the stroma, accumulates an elastic stress during tumor progression and, in function of it, elastically reacts.
   In this work, a strong reduction of PDAC spheroid growth in the presence of stress was reported and we demonstrated that spheroids growth decreases with increase stress.
   We decided to give a greater value to these results by testing another mechanical compressive stress: osmotic stress mediated by a high molecular weight Dextran. It is known that the Dextran is non-toxic with mammalian cells and, given its size, is not able to penetrate either the cell or the spheroid inducing a constant osmotic stress to the whole spheroid. The effect on the tumor spheroid growth, even in this case, resulted inhibitory but it must be pointed out, that the dextran stress is constant and agarose is a progressive compressive mechanical stress. For further demonstration of these results we tested the rule of mechanical tensile stress in 2D confirming the main idea that mechanical effects can have strong implications in cancer progression.
2. **The lower growth rate of a spheroid is a consequence of a decrease in single cell proliferation.** The previous observations suggest that the growth rate reduction after the application of the compressive stress controls the proliferation of the MCS.
   With the use of the high-performance mini-Western blot technique we analyzed the protein expression of spheroids under stress. In particular, the expression of pERK and p27 were evaluated. It was evident from the massive increase in the expression of p27

in compressed spheroids that compressive stress inhibits the proliferation of individual cells in the spheroid. Therefore we can conclude that our results show that direct mechanical effects can have strong implications in cancer proliferation.

3. **Evidence that the mechanical stress affect the efficacy of a proliferation-based chemotherapeutics.**

   Once we understood that the reduction of growth rate indicated even a reduced proliferative index we investigated what was the efficacy of a proliferation-based chemotherapy. We found a Gemcitabine efficacy decrement when spheroids proliferate less because of agarose compression. Then, we confirmed the agarose result with another mechanical stress, such as the dextran osmotic stress, and the Gemcitabine result with another chemotherapic, such as docetaxel.

   Until now, drug-resistance have been studied from a cell-centered point of view not considering the surrounding environment but our results proved that stromal components could also participate in the mechanisms of drug resistance. In addition, they could explain the large fraction of drugs failing clinical trials but passing the pre-clinic. The mechanisms coupling drug resistance to mechanical stress could both inform on approaches to better delineate chemotherapeutic strategies and design new screening platforms.

   Therefore, although stromal subtyping is still in its infancy, it may turn out to be an important stratification tool for future therapies.

To conclude this work it is still necessary to confirm the data with tensile stress and to investigate more on the spheroids protein expression especially on the agarose compressed spheroids. To analyze the spheroids embedded in agarose with the capillary Western blot there are some practical impediments: for instance, the spheroid has to be removed from the agarose matrix, which could lead biological perturbations. Therefore, in parallel we are looking to develop an innovative cryosection and immunostaining protocol.

In addition, it would also be nice to check the Docetaxel delivery from the SPNs (Spherical polymeric Nanoconstructs) particles in this solid system that allows us to tune the mechanical stress on the tumor progression. The SPNs already proved in vivo the targeting of solid tumors. Actually we have just some preliminary results, and to this regard, the transparization assay has proved to be a valid analysis tool.

3.5.2. Discussion and future perspectives

Compressive mechanical stress can affect any cell population that proliferates in a space-limited environment (196). However, until now, the study of compressive mechanical stress has been limited owing to the experimental difficulty of imposing a controlled compressive stress.

Our results suggest that increasing the concentration of agarose reversibly decreases pancreatic cancer spheroids volume growth. Comparison of spheroids response to chemotherapy under each condition showed that increasing the concentration of agarose decreases the spheroids growth and the single cell proliferation rate, and consequently decreases the chemotherapy responses. The combination of results suggests that limiting growth due compressive stress leads to a drug-resistant phenotype. Mechanical compression results in diminished drug responsiveness and spheroids in high stiffness of agarose are less responsive to chemotherapy. A mechanical-form of drug resistance exists: the efficacy can be directly altered by a mechanical-control of cell proliferation. The theoretical prediction of the experimental data, with the assumption that mechanical stress and pharmacological activity are decoupled, strongly supports this mechanism. The idea that quiescence can be a dominant mechanism leading to drug resistance is appreciated (197), but has never been linked to mechanical stress. Our data can potentially explain the reduced effect of chemotherapeutics of mechanically stressed cells (198) (199), although it remains to be demonstrated.

In addition, from a pharmacological point of view, we can say that a drug dose that is effective in reducing tumor volume for stress-free conditions does not work as well in a mechanically compressed environment. As an extrapolation, the extensively used drug screening system needs to be revalued and redesigned.

The tumor stroma, including its diverse cellular and non-cellular components, affects cancer progression and tumor response to therapy in multiple ways. Classical therapies of cancer focused on the transformed clonally expanded cell as the primary target for tumor detection and targeted intervention. Over the last years it became clear that the tumor microenvironment offers additional targets for detection and therapy. Tailoring such treatment to the patient requires effective means for analysis of such targets and for detection of the efficacy of intervention. An in vitro system like ours could fill this gap. However, it is clear that we have just begun to reveal the rich and rapidly changing landscape of the tumor stroma, and thus many challenges remain.

More work has to be done on the solid mechanics of cancer, opening new avenues for future basic or translational research. As regards basic research, a more detailed mechanical characterization of the surrounding solid tumors and host tissues is necessary. As regards the areas of translational research, first priority should be given to the definition of specific rules for stress reduction strategies. This involves the re-use of clinically approved drugs or the development of new drugs that can be used as stress alleviating agents. This should lead to the derivation of specific dose protocols, which, given the highly heterogeneous and dynamic nature of cancer, should be different among tumors and give rise to patient-specific protocols.

For instance, an enzyme is currently under clinical trial, such as the hyaluronidase in its pegylated-form, that digests hyaluronic acid reducing matrix swelling and, in combination with gemcitabine, increases chemotherapeutic efficacy (200). As we have seen, one of the key characteristics of PDAC progression is overproduction of hyaluronic acid and this solution has shown good potential. It is thought that the promising results are due to a reduction in solid stress that restores the tumor perfusion or part of it. However, it remains unclear how the hyaluronidase and Gemcitabine really work. Based on our results, for example, we could think that hyaluronidase, in addition to improving tumor perfusion, could mechanically modulate cell proliferation.

Collectively, in the antitumor battle, another goal to look for could be enforcing the tumor mechanical-dependent proliferation to increase its chemotherapy response.

4. Global Conclusions and prospective

In the first part of this study, the methods to develop more effective nanomedicines within the tumor system were evaluated. We have seen how the physical characteristics of the particles, such as shape, size, polymeric composition, loading and release capacities, could influence their success. Specifically, we focused our attention on some specific general features of the tumor, such as EPR effect, reduced blood flow in tumor vessels, red blood cell behavior and immune response But, the tumor system is highly heterogeneous and the tumor microenvironment is constantly evolving, then the optimal design of nanoparticles should likely be disease specific or tumor stage specific. In fact, in the second part of this work we discovered the importance of mechanical stress in compressed pancreatic tumor. It was seen that compressive mechanical stress reduced the proliferation of individual cells of a tumor spheroid and that this led to a reduced action of a proliferation-based drug.

The phenomena listed above are fundamental for the development of nanovectors, but if the cells in the tumor site were not reactive to chemotherapeutic drugs, what use would the efforts to develop nanovectors so efficient in reaching the target site and release the drug? That is, if the problem was not the efficiency of the nanovectors but the cell reactivity?

Specifically, in solid tumors, which represent 90% of human tumors including carcinomas and sarcomas, cell proliferation is followed by a progressive stiffening of the tissue, eventually becoming stiffer than healthy tissue. This phenomenon explains why tumors are frequently detected through physical palpation as they appear as a rigid mass residing in healthy tissues. For instance, pancreatic cancer at some point develops a stress that may inhibit proliferation, and consequently, make tumor cells inactive towards chemotherapy in general. So, the nanomedicine and chemotherapy in general, in order to achieve better results, should act with a broader view of the phenomena that occur during malignant development, and incorporate the “physics of cancer”.

We saw in the literature how the mechanical phenomena, minimally explored up to now, are demonstrating an important role in the tumorigenesis and consequently in the anti-cancer therapy, to the point of developing a new science: physical oncology. All these physical hallmarks of cancer, although not fully understood, are inspiring new anticancer strategies aiming to target and normalize the physical anomalies of solid tumors, particularly in the field of nanomedicine.

In particular, an original paradigm shift as future aim of this work could be the design of nanomedicines that, based on the tumor microenvironment, bring agents that reduce the tumor pressure and rigidity. They should be activated on demand to achieve a tailored spatio-temporal modulation of the tumor microenviroment and alleviate the resistance to current treatments, if necessary (201). Having the physical cues of cancer in mind, it can be important to cross-fertilize the fields of physical oncology and nanomedicine.

Bibliography

1. *The Role of Mechanical Forces in Tumor Growth and Therapy.* **Jain, R. K., Martin, J. D., and Stylianopoulos, T.** 2014, Annu. Rev. Biomed. Eng.

2. *The Fluid Mechanics of Cancer and Its Therapy.* **Koumoutsakos, P., Pivkin, I., and Milde, F.** 2013, Annu. Rev. Fluid Mech.

3. *Solid Stress inhibits the growth of multicelular tumor spheroids.* **Helmlinger, G., Netti, P. A., Lichtenbeld, H. C., Melder, R. J. & Jain, R. K.** 1997, Nat. Biotechnol.

4. *Glioma Expansion in Collagen I Matrices: Analyzing Collagen Concentration-Dependent Growth and Motility Patterns.* **Kaufman, L. J., Brangwynne, C. P., Kasza, K. E., Filippidi, E., Gordon, V. D., Deisboeck, T. S., and Weitz, D. A.** 2005, Biophys. J.

5. *Micro-Environmental Mechanical Stress Controls Tumor Spheroid Size and Morphology by Suppressing Proliferation and Inducing Apoptosis in Cancer Cells.* **Cheng, G., Tse, J., Jain, R. K., and Munn, L. L.** 2009, PLoS One.

6. *Gene Expression Profiles in 3D Tumor Analogs Indicate Compressive Strain Differentially Enhances Metastatic Potential.* **Demou, Z. N.** 2010, Ann. Biomed.

7. *Mechanical Compression Drives Cancer Cells Toward Invasive Phenotype.* **Tse, J. M., Cheng, G., Tyrrell, J. A., Wilcox-Adelman, S. A., Boucher, Y., Jain, R. K., and Munn, L. L.** 2012, Proc. Natl. Acad. Sci.

8. *Delivering Nanomedicine to Solid Tumors.* **Jain, R. K., and Stylianopoulos, T.** 2010, Nat. Rev. Clin. Oncol.

9. *Delivery of Molecular and Nanomedicine to Tumors: Transport Barriers and Strategies.* **Chauhan, V. P., Stylianopoulos, T., Boucher, Y., and Jain, R. K.** 2011, Ann. Rev. Chem. Biomol. Eng.

10. *Tumor vascular permeability and the EPR effect in macromolecular therapeutics: a review.* **H. Maeda, et al.** 2000, J. of Controlled Release.

11. *Soft Discoidal Polymeric Nanoconstructs Resist Macrophage Uptake and Enhance Vascular Targeting in Tumors.* **Key J, Palange AL, Gentile F, Aryal S, Stigliano C, Di Mascolo D, De Rosa E, Cho M, Lee Y, Singh J, Decuzzi P.** 2015, ACS Nano.

12. *Deformable Discoidal Polymeric Nanoconstructs for the Precise Delivery of Therapeutic and Imaging Agents.* **Palange AL, Palomba R, Rizzuti IF, Ferreira M, Decuzzi P.** 2017, Molecular Therapy.

13. *Tumor Microenvironment and Metabolism.* **Yang., Li V.** 2017, International Journal of Molecular Sciences.

14. *The Nanomedicine Revolution.* **Ventola, C.L.** 2012, Pharmacy and Therapeutics.

15. *Nanomedicine.* **Jr., R.A.F.,.** 1999, Vol. Volume I: Basic Capabilities.

16. *Nanomedicine, nanotechnology in medicine.* **Boisseau, P., et al.,.** 2011, Comptes Rendus Physique.

17. *How interdisciplinary is nanotechnology?* **Porter, A.L., et al.** 2009., J Nanopart Res.

18. *Nanoparticle-based drug delivery: case studies for cancer and cardiovascular applications. .* **Galvin, P., et al.** 2012, Cell Mol Life Sci.

19. *Development of Multifunctional Nanoparticles for Targeted Drug Delivery and Non-invasive Imaging of Therapeutic Effect.* **Sajja, H.K., et al.** 2009, Curr Drug Discov Technol.

20. *Emerging nanomedicines for early cancer detection and improved treatment: current perspective and future promise.* **Bharali, D.J., et al.** 2010., Pharmacol Ther.

21. *Nanoparticles: Properties, applications and toxicities.* **Khan, I., et al.** 2017, Arabian Journal of Chemistry.

22. *Nanoparticle-based targeted drug delivery.* **Singh, R., et al.** 2009, Exp Mol Pathol.

23. *Targeting strategies for multifunctional nanoparticles in cancer imaging and therapy.* **Yu M.K., et al.** 2012, Theranostics.

24. *Cancer active targeting by nanoparticles: a comprehensive review of literature.* **Bazak, R., et al.** 2015, J Cancer Res Clin Oncol.

25. *Fluorescent nanoprobes dedicated to in vivo imaging: from preclinical validations to clinical translation.* **Merian, J., et al.** 2012, Molecules.

26. *Nanoparticle-mediated systemic delivery of siRNA for treatment of cancers and viral infections.* **Draz, M.S., et al.** 2014, Theranostics.

27. *Nanoparticle interaction with plasma proteins as it relates to particle biodistribution, biocompatibility and therapeutic efficacy.* **Aggarwal, P., et al.** Adv Drug Deliv Rev : s.n., 2009.

28. *PEGylation as a strategy for improving nanoparticle-based drug and gene delivery.* **Suk, J.S., et al.** 2016, Adv Drug Deliv Rev.

29. *Nanoparticle PEGylation for imaging and therapy.* **Jokerst, J.V., et al.** 2011, Nanomedicine (Lond).

30. *pH-Responsive nanoparticles for drug delivery.* **Gao, W., et al.** 2010, Mol Pharm.

31. *Discovery of dendrimers and dendritic polymers: A brief historical perspective.* **Tomalia, D.A., et al.** 2002, Journal of Polymer Science Part A: Polymer Chemistry.

32. *Biofunctional nanosystems based on dendritic polymers.* **Quadir, M.A., et al.** 2012, J Control Release.

33. *Dendrimers as drug carriers: applications in different routes of drug administration.* **Cheng, Y., et al.** 2008, J Pharm Sci.

34. *Improvement of drug safety by the use of lipid-based nanocarriers. .* **Lim, S.B., et al.,.** 2012, J Control Release.

35. *Carbon nanotubes: properties, synthesis, purification, and medical applications.* **Eatemadi, A., et al.,.** 2014, Nanoscale Research Letters.

36. *Gadolinium-conjugated gold nanoshells for multimodal diagnostic imaging and photothermal cancer therapy.* **Coughlin, A.J., et al.,.** 2014, Small.

37. *Liposomes as nanomedical devices.* **Bozzuto, G., et al.,.** 2015, Int J Nanomedicine.

38. *Stealth liposomes: review of the basic science, rationale, and clinical applications, existing and potential.* **Immordino, M.L., et al.,.** 2006, International Journal of Nanomedicine.

39. *Recent advances with liposomes as pharmaceutical carriers.* **Torchilin, V.P.,.** 2005, Nat Rev Drug Discov.

40. *Liposomal Formulations in Clinical Use: An Updated Review.* **Bulbake, U., et al.,.** 2017, Pharmaceutics.

41. *Nanoparticles in the clinic.* **Anselmo, A.C., et al.,.** 2016, Bioeng Transl Med.

42. *Biodegradable Polymers.* **Vroman, I., et al.,.** 2009, Materials.

43. *Poly Lactic-co-Glycolic Acid (PLGA) as Biodegradable Controlled Drug Delivery Carrier.* **Makadia, H.K., et al.** 2011, Polymers (Basel).

44. *Self-assembled lipid--polymer hybrid nanoparticles: a robust drug delivery platform.* **Zhang, L., et al.,.** 2008, ACS Nano.

45. *Nanocarriers as an emerging platform for cancer therapy.* **Peer D., et al.** 2007, Nat. Nanotechnol.

46. *Spherical polymeric nanoconstructs for combined chemotherapeutic and anti-inflammatory therapies.* **Lee A., et al.** 2016, Nanomedicine (Lond.).

47. *Engineering of self-assembled nanoparticle platform for precisely controlled combination drug therapy.* **Kolishetti N., et al.** 2010, Proc. Natl. Acad. Sci.

48. *Multifunctional nanoparticles for multimodal imaging and theragnosis.* **Lee D.E., et al.** 2012, Chem. Soc. Rev.

49. *A brain tumor molecular imaging strategy using a new triple-modality MRI-photoacoustic-Raman nanoparticle.* **Kircher M.F., et al.** 2012, Nat. Med.

50. *Multifunctional nanoparticles for drug delivery and molecular imaging.* **Bao G., et al.** 2013, Annu. Rev. Biomed. Eng.

51. *Nanotheranostics - application and further development of nanomedicine strategies for advanced theranostics.* **Muthu M.S., et al.** 2014, Theranostics.

52. *Lipid-based nanoparticles as pharmaceutical drug carriers: from concepts to clinic.* **Puri A., et al.** 2009, Crit. Rev. Ther. Drug Carrier Syst.

53. *Polyester-based micelles and nanoparticles for the parenteral delivery of taxanes.* **Gaucher G., et al.** 2010, J. Control. Release.

54. *Physical-chemical aspects of protein corona: relevance to in vitro and in vivo biological impacts of nanoparticles.* **Monopoli M.P., et al.** 2011, J. Am. Chem. Soc. .

55. *Long-circulating and target-specific nanoparticles: theory to practice.* **Moghimi S.M., et al.** 2001, Pharmacol. Rev. .

56. *Comparative biodistribution of PAMAM dendrimers and HPMA copolymers in ovarian-tumor-bearing mice.* **Sadekar, et al.** 2011, Biomacromolecules.

57. *Mouse positron emission tomography study of the biodistribution of gold nanoparticles with different surface coatings using embedded copper-64.* **Frellsen A.F., et al.** 2016, ACS Nano.

58. *Particle size, surface coating, and PEGylation influence the biodistribution of quantum dots in living mice.* **Schipper M.L., et al.** 2009, Small.

59. *microPET-based biodistribution of quantum dots in living mice.* **Schipper M. L., et al.** 2007, J. Nucl. Med.

60. *The architecture and biological performance of drug-loaded LbL nanoparticles.* **Morton S. W., et al.** 2013, Biomaterials.

61. *Iodine-125 radiolabeling of silver nanoparticles for in vivo SPECT imaging.* **Chrastina A., et al.** 2015, Int. J. Nanomedicine.

62. *Analysis of nanoparticle delivery to tumours.* **Wilhelm S., et al.** 2016, Nat. Rev. Mater. .

63. *Delivery materials for siRNA therapeutics.* **Kanasty R., et al.** 201, Nat. Mater. .

64. *Multifunctional and stimuli-sensitive pharmaceutical nanocarriers.* **Torchilin V., et al.** 2009, Eur. J. Pharm. Biopharm. .

65. *PLGA-lecithin-PEG core-shell nanoparticles for controlled drug delivery.* **Chan J.M., et al.** 2009, Biomaterials.

66. *The dawning era of polymer therapeutics.* **Duncan, et al.** 2003, Nat. Rev. Drug Discov.

67. *Block copolymer micelles for drug delivery: design, characterization and biological significance.* **Kataoka K., et al.** 2001, Adv. Drug Deliv. Rev. .

68. *Dendrimers in biomedical applications--reflections on the field.* **Svenson S., et al.** 2005, Adv. Drug Deliv. Rev.

69. *Nanoshell-mediated near-infrared thermal therapy of tumors under magnetic resonance guidance.* **Hirsch L.R., et al.** 2003, Proc. Natl. Acad. Sci.

70. *Designed synthesis of uniformly sized iron oxide nanoparticles for efficient magnetic resonance imaging contrast agents.* **Lee N., et al.** 2012, Chem. Soc. Rev.

71. *Effects of erythrocyte deformability and aggregation on the cell free layer and apparent viscosity of microscopic blood flows.* **Zhang J., Johnson P.C., Popel A.S.** 2009, Microvasc. Res. .

72. *Traffic signals on endothelium for lymphocyte recirculation and leukocyte emigration.* . **T.A., Springer.** 1995, Annu. Rev. Physiol. .

73. *Hydrodynamic interaction between erythrocytes and leukocytes affects rheology of blood in microvessels.* . **Pappu V., Bagchi P.** 2007, Biorheology.

74. *Molecular mechanisms of platelet adhesion and activation.* **Andrews R.K., López J.A., Berndt M.C.** 1997, Int. J. Biochem. Cell Biol. .

75. *On the near-wall accumulation of injectable particles in the microcirculation: smaller is not better.* **Lee T.R., Choi M., Kopacz A.M., Yun S.H., Liu W.K., Decuzzi P.** 2013, Sci. Rep. .

76. *Steps toward mapping the human vasculature by phage display.* **Arap W., Kolonin M.G., Trepel M., Lahdenranta J., Cardó-Vila M., Giordano R.J., Mintz P.J., Ardelt P.U., Yao V.J., Vidal C.I.** 2002, Nat. Med.

77. *The preferential targeting of the diseased microvasculature by disk-like particles.* **Adriani G., de Tullio M.D., Ferrari M., Hussain F., Pascazio G., Liu X., Decuzzi P.** 2012, Biomaterials. .

78. *Intravascular delivery of particulate systems: does geometry really matter?* **Decuzzi P., Pasqualini R., Arap W., Ferrari M.** 2009, Pharm. Res. .

79. *Rapid tumoritropic accumulation of systemically injected plateloid particles and their biodistribution.* **van de Ven A.L., Kim P., Haley O., Fakhoury J.R., Adriani G., Schmulen J., Moloney P., Hussain F., Ferrari M., Liu X.** 2012, J. Control. Release. .

80. *Size and shape effects in the biodistribution of intravascularly injected particles.* **Decuzzi P., Godin B., Tanaka T., Lee S.Y., Chiappini C., Liu X., Ferrari M.** 2010, J. Control. Release.

81. *An injectable nanoparticle generator enhances delivery of cancer therapeutics.* **Xu R., Zhang G., Mai J., Deng X., Segura-Ibarra V., Wu S., Shen J., Liu H., Hu Z., Chen L.** 2016, Nat. Biotechnol.

82. *The effect of particle size on the biodistribution of low-modulus hydrogel PRINT particles.* **Merkel T.J., Chen K., Jones S.W., Pandya A.A., Tian S., Napier M.E., Zamboni W.E., DeSimone J.M.** 2012, J. Control. Release.

83. *Using mechanobiological mimicry of red blood cells to extend circulation times of hydrogel microparticles.* **Merkel T.J., Jones S.W., Herlihy K.P., Kersey F.R., Shields A.R., Napier M., Luft J.C., Wu H., Zamboni W.C., Wang A.Z.** 2011, Proc. Natl. Acad. Sci. .

84. *avb3 Integrin-targeted PLGA-PEG nanoparticles for enhanced anti-tumor efficacy of a Pt(IV) prodrug.* . **Graf N, Bielenberg DR, Kolishetti N, Muus C, Banyard J, Farokhzad OC, et al.** 2012, ACS Nano .

85. *Surfactant-free, drug-quantum-dot coloaded poly(lactide-co-glycolide) nanoparticles: towards multifunctional nanoparticles.* **Nehilla BJ, Allen PG, Desai TA.** 2008, ACS Nano.

86. *Multifunctional nanoparticles for combined doxorubicin and photothermal treatments.* . **Park H, Yang J, Lee J, Haam S, Choi I-H, Yoo K-H.** 2009, ACS Nano .

87. *Nanotechnology for breast cancer therapy.* . **Tanaka T, Decuzzi P, Cristofanilli M, Sakamoto J, Tasciotti E, Robertson F, et al.** 2009, Biomed Microdevices.

88. *Direct fabrication and harvesting of monodisperse, shape-specific nanobiomaterials.* **Rolland JP, Maynor BW, Euliss LE, Exner AE, Denison GM, DeSimone JM.** 2005, J Am Chem Soc .

89. *Role of target geometry in phagocytosis.* **Champion JA, Mitragotri S.** 2006, Proc Natl Acad Sci .

90. *The hydrogel template method for fabrication of homogeneous nano/microparticles.* **Acharya G, Shin CS, McDermott M, Mishra H, Park H, Kwon IC, et al.** 2010, J. Controlled Release.

91. *Mesoporous silicon particles as a multistage delivery system for imaging and therapeutic applications.* . **Tasciotti E, Liu X, Bhavane R, Plant K, Leonard AD, Price BK, et al.** 2008, Nat Nanotechnol.

92. *The effect of particle size on the biodistribution of low-modulus hydrogel PRINT particles.* **Merkel TJ, Chen K, Jones SW, Pandya AA, Tian S, Napier ME, et al.** 2012, J. Controlled Release .

93. *A study of drug release from homogeneous PLGA microstructures.* . **Acharya G, Shin CS, Vedantham K, McDermott M, Rish T, Hansen K, et al.** 2010, J Control Release.

94. *Engineering discoidal polymeric nanoconstructs with enhanced magneto-optical properties for tumor imaging.* **Key J, Aryal S, Gentile F, Ananta JS, Zhong M, Landis MD, Decuzzi P.** 2013, Biomaterials, pp. 34(21): p. 5402-10.

95. *Dexamethasone-loaded Polymeric Nanoconstructs for Monitoring and Treating Inflammatory Bowel Disease.* **Lee, A., et al.** 2017, Theranostics, pp. 7(15): p. 3653-3666.

96. *Doxorubicin-loaded nanocarriers: A comparative study of liposome and nanostructured lipid carrier as alternatives for cancer therapy.* **Fernandes, R.S., et al.** 2016, Biomed Pharmacother, pp. 84: p. 252-257.

97. *Modulating Phagocytic Cell Sequestration by Tailoring Nanoconstruct Softness.* **Palomba, R., et al.** 2018, ACS Nano, pp. 12(2): p. 1433-1444.

98. *Mechanotransduction in development.* **Farge E., et al.** 2011, Curr. Top. Dev. Biol.

99. *A tense situation: forcing tumour progression.* **Butcher D. T., Alliston T. and Weaver V. M.** 2009 , Nature Rev. Cancer.

100. *Cell Mechanics: From Single Scale-Based.* **Chauvière A., Preziosi L. and Verdier C.** 2009, Models to Multiscale Modeling , Vol. 32.

101. *The invasive growth of malignant tumours as a purely mechanical process* . **Eaves G., et al.** 1973, J. Pathology.

102. *The invasive growth of malignant tumours: an experimental interpretation based on elastic-jelly models.* **Young, et al.** 1959, J. Pathol. Bacteriol.

103. *Mechanical factors activate beta-catenin-dependent oncogene expression in APC mouse colon.* **Whitehead J., Vignjevic D., Futterer C., Beaurepaire E., Robine S. and Farge E.** 2008, HFSP J.

104. *Causes, consequences, and remedies for growth-induced solid stress in murine and human tumors.* **Stylianopoulos, T. et al.** 2012, Proc. Natl. Acad. Sci.

105. *Mechanical Control of Cell flow in Multicellular Spheroids.* **Morgan Delarue, Fabien Montel, Ouriel Caen, Jens Elgeti, Jean-Michel Siaugue, Danijela Vignjevic,Jacques Prost, Jean-Franc¸ois Joanny, and Giovanni Cappello.** 2013, PHYSICAL REVIEW LETTERS.

106. *Compressive Stress Inhibits Proliferation in Tumor Spheroids through a Volume Limitation.* **Morgan Delarue, Fabien Montel, Danijela Vignjevic, Jacques Prost, Jean-Francois Joanny and Giovanni Cappello.** 2014, Biophysical Journal.

107. *Effect of an osmotic stress on multicellular aggregates.* **Sylvain Monnier, Morgan Delarue, Benjamin Brunel, Monika E. Dolega, Antoine Delon and Giovanni Cappello.** 2015, Methods, pp. 94, 114-119.

108. *Cell-like pressure sensors reveal increase of mechanical stress towards the core of multicellular spheroids under compression.* **M.E. Dolega, M. Delarue, F. Ingremeau, J. Prost, A. Delon & G. Cappello.** 2016, Nature Comunications.

109. *Solid stress generated by spheroid growth estimated using a linear poroelasticity model.* **Tiina Roosea, Paolo A.Netti, Lance L. Munn, Yves Boucher and Rakesh K.Jaina.** 3, 2003, Microvascular Research, Vol. 66.

110. *Solid Stress inhibits the growth of multicelular tumor spheroids.* **Helmlinger, G., Netti, P. A., Lichtenbeld, H. C., Melder, R. J. & Jain, R. K.** 1997, Nat. Biotechnol., pp. 15, 778–783 .

111. *Friends or foesbipolar effects of the tumour stroma in cancer.* **E., Mueller M. M. and Fusenig N.** 2004, Nature Rev. Cancer.

112. *Stromal fibroblasts in cancer: a novel tumor-promoting cell type.* **Orimo A., and Weinberg R.** 2006, Cell Cycle.

113. *Integrins and extracellular matrix in mechanotransduction.* **Schwartz M.A., et al.** 2010, Cold Spring Harb Perspect Biol 2.

114. *The extracellular matrix: Not just pretty fibrils.* **Hynes R.O., et al.** 2009, Science.

115. *Tissue cells feel and respond to the stiffness of their substrate.* **Discher D.E., Janmey P., Wang Y.l.** 2005, Science.

116. *Migration of tumor cells in 3D matrices is governed by matrix stiffness along with cell-matrix adhesion and proteolysis.* **Zaman MH, et al.** 2006, Proc Natl Acad Sci.

117. *Matrix elasticity directs stem cell lineage specification.* . **Engler A.J., Sen S., Sweeney H.L., Discher D.E.** 2006, Cell.

118. *Coevolution of solid stress and interstitial fluid pressure in tumors during progression: implications for vascular collapse.* **Stylianopoulos, T. et al.** 2013, Cancer Res.

119. *Cell tension, matrix mechanics, and cancer development.* **Huang S., Ingber D.E.** 2005, Cancer Cell.

120. *Drug resistance in cancer: an overview.* **Housman, G. et al.** 2014, Cancers (Basel).

121. *Hypoxia–a key regulatory factor in tumour growth.* **A.L., Harris.** 2002, nat rev.

122. *The Role of Matrix Compliance on Cell Responses to Drugs and Toxins: Towards Predictive Drug Screening Platforms.* **Zustiak, S. P.** 2015, Macromol. Biosci.

123. *Role of three-dimensional matrix stiffness in regulating the chemoresistance of hepatocellular carcinoma cells.* **Liu, C. et al.** 2015, Biotechnol. Appl. Biochem.

124. *Human Organ Chip Models Recapitulate Orthotopic Lung Cancer Growth, Therapeutic Responses, and Tumor Dormancy In Vitro.* **Hassell, B. A. et al.** 2017, Cell Rep. .

125. *Flow perfusion effects on three-dimensional culture and drug sensitivity of Ewing sarcoma.* **Santoro, M., Lamhamedi-Cherradi, S.-E., Menegaz, B. A., Ludwig, J. A. & Mikos, A. G.** 2015, Proc. Natl. Acad. Sci.

126. *Stemness and chemoresistance in epithelial ovarian carcinoma cells under shear stress.* **Ip, C. K. M. et al.** 2016, Sci. Rep.

127. *Control of Cyclin D1 , p27 Kip1 , and Cell Cycle Progression in Human Capillary Endothelial Cells by Cell Shape and Cytoskeletal Tension.* **Huang, S., Chen, C. S. & Ingber, D. E.** 1998.

128. *Cell cycle-mediated drug resistance: an emerging concept in cancer therapy.* **Shah, M. A. & Schwartz, G. K.** 2001, Clin. Cancer Res. .

129. *A model of quiescent tumour microregions for evaluating multicellular resistance to chemotherapeutic drugs.* **H.R. Mellor, et al.** 2005, British Journal of Cancer.

130. *Gemcitabine: Metabolism and molecular mechanisms of action, sensitivity and chemoresistance in pancreatic cancer.* **Lucas de Sousa Cavalcante, Gisele Monteiro.** 2014, European Journal of Pharmacology.

131. *Identification and analysis of single-nucleotide polymorphisms in the gemcitabine pharmacologic pathway.* . **Fukunaga A.K., Marsh S., Murry D.J., Hurley T.D., McLeod H.L.** 2004, Pharmacogenomics J.

132. *Cellular pharmacology of gemcitabine.* **Mini E., Nobili S., Caciagli B., Landini I., Mazzei T.** 2006, Ann Oncol 17.

133. *Pharmacogenomics of gemcitabine: can genetic studies lead to tailor-made therapy?* **H. Ueno, et al.** 2007, British Journal of Cancer.

134. *Action of 2', 2'-difluorodeoxycytidine on DNA synthesis.* . **Huang, P., et al.** 1991, Cancer Res.

135. *Excision of 2',2'-difluorodeoxycytidine (gemcitabine) monophosphate residues from DNA.* **Gandhi V., et al.** 1996, Camcer Res.

136. *Cellular elimination of 2',2'-difluorodeoxycytidine 5'-triphosphate: a mechanism of self-potentiation.* **Heinemann V., et al.** 1992, Cancer Res.52.

137. *Smarter drugs emerging in pancreatic cancer therapy. .* **Kleger, A., Perkhofer, L., Seufferlein, T.** 2014, Ann. Oncol. 25.

138. *Beyond first-line chemotherapy for advanced pancreatic cancer: an expanding array of therapeutic options?* **Walker, E.J., Ko, A.H..** 2014, World J. Gastroenterol. 20.

139. *Determinants of resistance to 2',2'-difluoro-2'-deoxycytidine (Gemcitabine).* **Andries M. Bergman, Herbert M. Pinedo, Godefridus J. Peters.** 2001, Churchill livingstone - Drug Resistance updates.

140. *Stroml biology and therapy in pancreatic cancer.* **Neesse A., et al.** 2011, Gut.

141. *Gemcitabine-Based Therapy in Pancreas Cancer. Gemcitabine-Docetaxel and Other Novel Combinations.* **Jacobs., Andrew D.** 2002, Cancer.

142. *Gemcitabine (G) and Taxotere (T) in patients with unresectable pancreatic carcinoma.* **Jacobs AD, Otero H, Picozzi V, et al.** 1999, Proc Am Soc Clin Oncol.

143. *A Phase I/II study of gemcitabine (G) and docetaxel (D) in patients (pts) with unresectable pancreatic cancer. .* **Jacobs AD, Otero H, Picozzi V, et al.** 2000, Proc Am Soc Clin Oncol.

144. *Improvements in survival and clinical benefit with gemcitabine as first-line therapy for patients with advanced pancreas cancer: a randomized trial.* **Burris HA 3rd, Moore MJ, Anderson J, et al.** 1997, J Clin Oncol. .

145. *Pancreatic cancer.* **Kleeff J, Korc M, Apte M, et al.** 2016, Nat Rev Dis Primers .

146. *Hyaluronan-Derived Swelling of Solid Tumors, the Contribution of Collagen and Cancer Cells, and Implications for Cancer Therapy.* **Voutouri C., Polydorou C., Papageorgis P., Gkretsi V., Stylianopoulos T.**

147. *Cellular capsules as a tool for multicellular spheroid production and for investigating the mechanics of tumor progression in vitro.* **Kévin Alessandri, et al.** 2013, Proceedings of the National Academy of Sciences.

148. *AAPT Diagnostic Criteria for Chronic Cancer Pain Conditions.* **Paice JA. Mulvey M. Bennett M., Dougherty PM., Farrar JT., Mantyh PW., Miaskowski C., Schmidt B., Smith TJ.** 2017, J. Pain.

149. *Solid stress and elastic energy as measures of tumour mechanopathology.* **Hadi T. Nia, et al.** 2016, Nature Biomedical Engineering.

150. *Obesity-Induced Inflammation and Desmoplasia Promote Pancreatic Cancer Progression and Resistance to Chemotherapy.* **Incio, J., Liu, H., Suboj, P., Chin, S. M., Chen, I. X., Pinter, M., … Jain, R. K.** 2016, Cancer Discovery.

151. *Improvements in survival and clinical benefit with gemcitabine as first-line therapy for patients with advanced pancreas cancer: a randomized trial.* **Burris HA 3rd, Moore MJ, Andersen J, et al.** 1997, J Clin Oncol.

152. *A phase II trial of gemcitabine in patients with 5-FU-refractory pancreas cancer.* **Rothenberg ML, Moore MJ, Cripps MC, et al.** 1996, Ann Oncol.

153. *Adjuvant chemotherapy with fluorouracil plus folinic acid vs gemcitabine following pancreatic cancer resection: a randomized controlled trial.* **Neoptolemos JP, Stocken DD, Bassi C, et al.** 2010, JAMA.

154. *FOLFIRINOX versus gemcitabine for metastatic pancreatic cancer.* **Conroy T, Desseigne F, Ychou M, et al.** 2011, N Engl J Med .

155. *Increased survival in pancreatic cancer with nab-paclitaxel plus gemcitabine.* **Von Hoff DD, Ervin T, Arena FP, et al.** 2013, N Engl J Med.

156. *Inhibition of Hedgehog signaling enhances delivery of chemotherapy in a mouse model of pancreatic cancer.* **Olive KP, Jacobetz MA, Davidson CJ, et al.** 2009, Science .

157. *Molecular genetic basis of pancreatic adenocarcinoma.* **Hilgers W, Kern SE.** 1999, Genes Chromosomes Cancer.

158. *Genetic progression in the pancreatic ducts.* **Hruban RH, Wilentz RE, Kern SE.** 2000, Am J Pathol .

159. *Stromal biology and therapy in pancreatic cancer: a changing paradigm.* **Neesse, et al.** 2015, Gut.

160. *Pathogenic Mechanisms of Pancreatitis.* **Manohar, Murli et al.** 2017, World Journal of Gastrointestinal Pharmacology and Therapeutics.

161. *Depletion of Carcinoma-Associated Fibroblasts and Fibrosis Induces Immunosuppression and Accelerates Pancreas Cancer with Reduced Survival.* **Özdemir, Berna C. et al.** 2014, Cancer Cell.

162. *Hyaluronan Impairs Vascular Function and Drug Delivery in a Mouse Model of Pancreatic Cancer.* **Jacobetz, Michael A. et al.** 2013, Gut.

163. *Cell and environment interactions in tumor microregions: the multicell spheroid model.* **Sutherland, R. M.** 1988, Science.

164. *Multicellular tumor spheroids: an underestimated tool is catching up again.* **Hirschhaeuser, F., H. Menne, L. A. Kunz-Schughart.** 2010, J. Biotechnol.

165. *Externally applied forces can phenotypically revert malignant breast epithelial structures.* **Venugopalan, G.** 2012, Mol. Biol. Cell.

166. *Are biomechanical changes necessary for tumor progression?* **Fritsch, A., M. Hockel, J.A.Kas.** 2010, Nat. Phys.

167. *Morphogenetic fields of embryonic development in locoregional cancer spread.* **Hockel, M.** 2015, Lancet Oncol.

168. *Collective cell migration in morphogenesis, regeneration and cancer.* **Friedl, P. & Gilmour, D.** 2009, Nat. Rev. Mol. Cell Biol.

169. *Stress clamp experiments on multicellular tumor spheroids. .* **Montel, F., M. Delarue, ., J. F. Joanny.** 2011, Phys. Rev. Lett.

170. *Isotropic stress reduces proliferation in multicellular spheroids.* **Montel, F., M. Delarue,., J. Prost.** 2012, New J. Phys.

171. *Isotropic stress reduces cell proliferation in tumor spheroids.* **Montel, F.** 2012, New J. Phys., pp. 14, 55008.

172. *Structure and dynamics of multicellular assemblies measured by coherent light scattering.* **Benjamin Brunel, Carles Blanch, Aurélien Gourrier, Vanni Petrolli, Antoine Delon, Jean-François Joanny, Rémi Carminati, Romain Pierrat, Giovanni Cappello.** 2017, New Journal of Physics.

173. *Cell shape and cell division.* **M. Théry, M. Bornens.** 2006, Curr. Opin. Cell Biol. 18 .

174. *Cell movement is guided by the rigidity of the substrate.* **C.M. Lo, H.B. Wang, M. Dembo, Y.L. Wang.** 2000, Biophys. J. .

175. *Matrix elasticity directs stem cell lineage specification.* **A.J. Engler, S. Sen, H.L. Sweeney, D.E. Discher.** 2006, Cell 126.

176. *KRAS Mutant Pancreatic Cancer: No Lone Path to an Effective Treatment.* **Daniel Zeitouni, Yuliya Pylayeva-Gupta, Channing J. Der, and Kirsten L. Bryant.** 2016, Cancers (Basel).

177. *Spheroid based drug screen: considerations and practical approach.* . **Friedrich, J., C. Seidel, L. A. Kunz-Schughart.** 2009, Nat. Protoc.

178. *Energy metabolism transition in multi-cellular human tumor spheroids.* **Rodrıguez-Enrıquez, S., J. C. Gallardo-Pe´rez,., R. Moreno-Sanchez.** 2008, J. Cell. Physiol.

179. *Multicellular tumor spheroids: An underestimated tool is catching up again.* **W. Mueller-Klieser, et al.** 2010, J. Biotechnol.

180. *Role of taxanes in pancreatic cancer.* **Carmen Belli, Stefano Cereda, Michele Reni.** 2012, World J Gastroenterol .

181. *Mode of action of docetaxel – a basis for combination with novel anticancer agents.* **Roy S. Herbst, et al.** 2003, Cancer Treatment Reviews.

182. *Radiolabeled Polymeric Nanoconstructs Loaded with Docetaxel and Curcumin for Cancer Combinatorial Therapy.* **Stigliano, Cinzia.** 2015, Advanced functional materials.

183. *Osmotic Pressure of Latex Dispersions.* **Cabane., C. Bonnet-GonnetL. L. BelloniB. and B.** 1994, ACS Publications.

184. *Casein Micelle Dispersions under Osmotic Stress.* **Bouchoux Antoine, et al.** 2008, Biophysical Journal.

185. *MEK/ERK signaling pathway regulates the expression of Bcl-2, Bcl-XL, and Mcl-1 and promotes survival of human pancreatic cancer cells.* **Marie-Josée Boucher Jean Morisset Pierre H. Vachon John C. Reed Jean Lainé, Nathalie Rivard.** 2000, Journal of Cellular Biochemistry.

186. *A high-throughput imaging and nuclear segmentation analysis protocol for cleared 3D culture models.* **Molly E. Boutin, et al.** 2018, Vol. Scientific Reports.

187. *The Effect of Matrix Stiffness on the Differentiation of Mesenchymal Stem Cells in Response to TGF-β.* **Song Li, et al.** 2011, Biomaterials.

188. *Matrix stiffness regulates migration of human lung fibroblasts.* **Hasegawa Y, et al.** 2017, Physiol Rep.

189. *The effect of substrate stiffness on adult neural stem cell behavior.* **Molly S. Shoichet, et al.** 36, 2009, Vol. 30.

190. *Tumor matrix stiffness promotes metastatic cancer cell interaction with the endothelium.* **Sara Zanivan, et al.** 2017, EMBO J. .

191. *Matrix stiffness induces epithelial–mesenchymal transition and promotes chemoresistance in pancreatic cancer cells.* **Río Hernández, et al.** 2017, Oncogenesis volume 6.

192. *Extracellular matrix stiffness and composition jointly regulate the induction of malignant phenotypes in mammary epithelium.* **David J. Mooney, et al.** 2014, Nature Materials volume 13.

193. *The role of matrix stiffness in hepatic stellate cell activation and liver fibrosis.* **Wells RG, et al.** 2005, J Clin Gastroenterol.

194. *Matrix stiffness affects spontaneous contraction of cardiomyocytes cultured within a PEGylated fibrinogen biomaterial. Acta Biomaterialia.* **DrorSeliktar, et al.** 2007, Volume 3, Issue 1.

195. *The effects of matrix stiffness and RhoA on the phenotypic plasticity of smooth muscle cells in a 3-D biosynthetic hydrogel system.* **Andrew J.Putnam, et al.** 2008, Biomaterials, volume 29, Issue 17.

196. *SCWISh network is essential for survival under mechanical pressure.* **Morgan Delarue, et al.** 2017, PNAS.

197. *Cell Cycle-mediated Drug Resistance.* **Schwartz., Manish A. Shah and Gary K.** 2001, Clinical Cancer Research.

198. *Substrate stiffness influences the outcome of antitumor drug screening in vitro.* **Jiantao, Feng, et al., et al.** 2013, Clinical hemorheology and microcirculation.

199. *Stemness and chemoresistance in epithelial ovarian carcinoma cells under shear stress.* **C. K. Ip, S.-S. Li, M. Y. Tang, S. K. Sy, Y. Ren, H. C. Shum, and A. S. Wong.** 2016, Scientific Reports.

200. *Enzymatic targeting of the stroma ablates physical barriers to treatment of pancreatic ductal adenocarcinoma.* **Provenzano PP, Cuevas C, Chang AE, Goel VK, Von Hoff DD, Hingorani SR.** Cancer Cell : s.n., 2012.

201. *Physical oncology: New targets for nanomedicine.* **Alba Nicolas-Boluda, Amanda K.A. Silva, Sylvie Fournel, Florence Gazeau.** 2017, Biomaterials.

202. **Mack, Chris.** *Fundamental Principles of Optical Lithography: The Science of Microfabrication.* s.l. : John Wiley & Sons, Ltd., 2007.

203. *2001.* **S. Kawata, H. B. Sun, T. Tanaka, K. Takada.** Nature.

204. **J. Fischer, M. Wegener.** 2011, Opt. Mater. Express.

205. **T. G. Leong, A. M. Zarafshar, D. H. Gracias.** 2010, Small.

206. **M. P. Stocker, L. Li, R. R. Gattass, J. T. Fourkas.** 2011, Nat. Chem. .

207. *Heidelberg DWL 66fs Laser Writer Manual.* **Sun, Yong.** s.l. : Heidelberg Company.

208. **Franssila, Sami.** *Introduction to Microfabrication, Second Edition.* 2010.

209. **Kang, Shin-Won.** *Application of Soft Lithography for Nano Functional Devices.* 2010.

210. **Brett, C.M.A., Oliveira Brett, A.M.** *Electrochemistry, principles, methods and applications.* Oxford : Oxford University Press, , 1994.

211. **Coulter, Beckman.** *Multisizer 4e Coulter Counter Book.* 2009.

212. **Pecora, R.** *Dynamic Light Scattering: Applications of Photon Correlation Spectroscopy.* 1938.

213. *Tumor Microenvironment and Metabolism. .* **Yang., Li V.** 2017, International Journal of Molecular Sciences.

214. *Micro-Environmental Mechanical Stress Controls Tumor Spheroid Size and Morphology by Suppressing Proliferation and Inducing Apoptosis in Cancer Cells.* **Gang Cheng, Janet Tse,Rakesh K. Jain,Lance L. Munn.** 2009, PLOS ONE.

215. *Homeostatic competition drives tumorgrowth and metastasis nucleation.* **Basan M., Thomas Risler, Joanny J-F., Sastre-Garau X. and Prost J.** 2009, HFSP J.

216. *From single cells to tissue architecture—a bottom-up approach to modelling the spatio-temporal organisation of complex multi-cellular system.* . **Galle J., Hoffmann M. and Aust G.** 2009, Math. Biol.

217. *Modeling the effect of deregulated proliferation and apoptosis on the growth dynamics of epithelial cell populations in vitro.* **Galle J., Loeffler M. and Drasdo D.** 2005, Biophys. J.

218. *On the role of physics in the growth and pattern formation of multi-cellular systems: what can we learn from individual-cell based models?* . **Drasdo D., Hoehme S. and Block M.** 2007, J. Stat. Phys.

219. *Mathematical modelling of the loss of tissue compression responsiveness and its role in solid tumour development.* **Chaplain M. A., Graziano L. and Preziosi L.** 2006, Math. Med. Biol.

220. *Validation of the 6th edition AJCC pancreatic cancer staging system: report from the national cancer database.* **Bilimoria, et al.** 2007, Cancer.

221. *Dissecting cancer through mathematics: from the cell to the animal model.* **Byrne H. M., et al.** 2010, Nature Rev. Cancer.

222. *Gelatin-coated magnetic iron oxide nanoparticles as carrier system: drug loading and in vitro drug release study.* **Gaihre B., et al.** 2009, Int. J. Pharm. .

223. *Individual-based and continuum models of growing cell populations: a comparison.* **Byrne H., and Drasdo D.** 2009, J. Math. Biol.

224. *Cancer statistics.* **Jemal A, Siegel R, Ward E, et al.** 2008, CA.

Valorization

During my PhD, we explored two complementary axes of research:

1/ Can we improve the design of blood – cells inspired Nanoconstructs in terms of drug-loading efficiency, phagocytic cells sequestration, and tumor accumulation?

Publications

"Deformable Discoidal Polymeric Nanoconstructs for the precise delivery of therapeutic and imaging agents", Palange A, Palomba R, Rizzuti I F, Ferreira M, Decuzzi P *, Molecular Therapy- 2017.

"Modulating phagocytic cell sequestration by tailoring nanoconstruct softness", R Palomba, AL Palange, IF Rizzuti, M Ferreira, A Cervadoro, MG Barbato, Claudio Canale, Paolo Decuzzi. ACS nano – 2018.

"A tissue chamber chip for assessing nanoparticle mobility in the extravascular space", Valeria Lusi, Thomas L Moore, Federica Laurino, Alessandro Coclite, Rui Perreira, Miguel Ferreira, Ilaria Rizzuti, Roberto Palomba, Paolo Zunino, Marti Duocastella, Shoshy Mizrahy, Dan Peer, Paolo Decuzzi – 2019.

"OPTIMIZING THE PHARMACOLOGICAL PROPERTIES OF DISCOIDAL POLYMERIC NANOCONSTRUCTS AGAINST TRIPLE NEGATIVE BREAST CANCER" Ilaria Francesca Rizzuti, Miguel Ferreira, Anna Lisa Palange, Maria Grazia Barbato, Valentina Di Francesco, Martina Di Francesco, and Paolo Decuzzi. (Article in revision)

Other activities

Participation and Poster sessions at European Foundation for Clinical Nano-medicine, https://www.clinam.org, Basel Switzerland 7-10 May: Discoidal Polymeric Nanoconstructs: Tuning Size, Shape, Surface properties and mechanical Stiffnes; Rizzuti IF, Palange AL, Ferreira M, Palomba R, Decuzzi P.

Participation and Poster session at CRS Annual Meeting & Exposition July 16–19 Boston, Massachusetts, U.S.A https://www.controlledreleasesociety.org/meetings/annual/program/Pages/default.aspx: TUMOR-ON-A-CHIP: SELECTING NANOMEDICINES FOR VASCULAR TRANSPORT EFFICIENCY AND ANTI-CANCER POTENCY, Ilaria F. Rizzuti, Rui C. Pereira, Chiara Manneschi, Annalisa Palange, Paolo Decuzzi.

2/ Once the drug is locally present in the tumor, what would be the impact of mechanical stress on its efficacy?

Publications

"Mechanical-control of chemotherapeutic efficacy through modulation of cell proliferation." Ilaria Francesca Rizzuti, Pietro Mascheroni, Silvia Arcucci, Audrey Prunet, Catherine Barentin, Charlotte Riviere, Helene Delanoe-Ayari, Haralampoulos Hatzirikou, Julie Guillermet-Guibert, and Morgan Delarue (currently in submission).

Other activities

Co-training and co-teaching of Julie Pignolet at the LAAS-CNRS during her Master's internship

Apendix

a. Nanotechnology tools

There are two types of approaches to the creation of artificial nanostructures. The TOP-DOWN approach starts with macroscopic materials while the BOTTON-UP approach starts with atoms and molecules. Lithography is a TOP-DOWN technique. The objective of lithography is to define micro or nanometric three-dimensional structures of a device. The most common lithographic technique is optical lithography.

1. Photolithography or optical lithography

A conventional optical lithography system consists of: a light source, a photomask, an optical system and the photoresist deposited on the wafer. Photolithography, also called UV lithography, is a process used in the microfabrication of three-dimensional and two-dimensional structures inside a thin film or a substrate. It uses light to transfer a geometric design from a photomask to a photoresist or simply photosensitive resist, deposited on a substrate. Photolithography arises from the necessity to shape a film on a substrate (and replicate it in many copies, on many substrates). This happens through two distinct steps:

- exposure (to UV light);
- development, or selective removal of some parts of resist, depending on whether they have been exposed or not, through the covering with the mask.

The fundamental steps of the lithographic process are:

- substrate preparation;
- coating [by spinner];
- pre-cooking [pre-bake or soft bake];
- alignment of the photomask;
- exposure;
- development;
- annealing [post-bake or hard bake];
- other processes on the substrate so masked by the resist;
- removal of the resist [stripping];
- cleaning after the process [ashing].

1.1. Resists

The resist consists of:

- a non-photosensitive basic substance (resin, polymer) consisting of a set of monomers, with a very high molecular weight (100,000-200,000 atomic masses);
- a photosensitive substance, sensitive to the wavelength used;
- a solvent to reduce the viscosity and allow the substrate to be covered.

The resist can be positive or negative:

- positive is a type of resist for which the part of the resist that is exposed to the light becomes soluble during the development, while the unexposed portion remains insoluble to development (alkaline solutions);
- negative resist, (generally less used) instead, is a type of resist in which the portion exposed to the light polymerizes and becomes insoluble to development. While the unexposed part remains soluble during the development (organic sovents).

Advanced lithographic techniques with higher resolution, currently being studied as potential substitutes for conventional photolithography, include: lithography in the extreme UV (EUV), soft X-ray litography, Direct Laser Writing (DLW) and electron beam writing (e-beam), ionic ray writing focused (FIB) and probe lithography (202).

2. Direct Laser Writer Lithography

The significane of direct laser writing (DLW) lithography increased considerably during the last years (203) (204) (205). Two-photon direct laser writing (DLW) is 3D printing for the microscopic world. This techniques has a resolution around 600-700 nm and goes beyond the smallest shapes and sizes that can be accomplished by garden variety 3D printing.

The mechanism on which DLW is based is free radical polymerization. Hereby, a photoinitiator is excited by one or two-photon excitation (1PE and 2PE, respectively) into the first excited singlet state. Since typically photoinitiators are now designed to show a very high intersystem crossing (ISC) rate (>85%) the excited molecule will populate its triplet state from where it can react with environmental molecules forming radical compound that can start the polymerization reaction of the resin, which is mostly an acrylate. By carefully choosing the resin (206) and the photoinitiator, very solid structures with sub-micron sizes can be fabricated. The Heidelberg DWL 66fs is a high resolution pattern generator for mask

making and direct writing. Its capabilities and flexibility make it an ideal lithographic tool for research. It uses acousto-optic modulators to adjust the laser intensity, and acousto-optic deflectors to scan the beam. During an exposure, only the stage moves. The substrate is held down on the stage by vacuum and moves in the x-y plane. Its position is constantly monitored by an interferometer system with a resolution of 10 nm. The optical setup utilizes a diode laser (λ = 405 nm) as its light source. It can expose both 2D and 3D structures, e.g. gray scale lithography with thick photoresists. There are two write heads available: 4 mm & 20 mm. Both heads use an air-gauge to monitor N_2 pressure change, which is then feedback to the lens piezo actuators for auto focus. During a scan, user patterns are divided into stripes along Y-axis, each stripe contains 100 pixels. The stage moves along Y-axis to finish exposing one stripe, then steps in X-axis to start exposing the next stripe. The user patterns are then stitched together. In term of resolution, the 4 mm write head can achieve a minimum feature size of ~800 nm, the 20 mm head can achieve a minimum feature size of ~4 µm. The 20 mm head writes about 12 times faster than the 4 mm head (207).

3. Deep Reactive Ion Etching (RIE)

Once the resist mask is prepared by lithography, the uncovered material is removed by a chemical etching (gas or plasma) - physical (sputter). Reactive Ion Etching (RIE) is a plasma etching technique that uses reactive ions like F- or Cl- (halogens) produced by ionizing gases, to interact with exposed surfaces of samples that results in chemical etching. The plasma is struck in the gas mixture and ions accelerate toward substrate and the reaction occurs on the surface (chemical). The main advantage of the RIE is the anisotropic etching (unlike in wet etching) (208).

4. Soft Lithography

Soft lithography represents a non-photolithographic strategy based on a principle of self-assembly and printing of a replica. It provides a convenient, effective and low-cost method for the formation and fabrication of micro- and nanostructures. In soft lithography, a 'stamp', i.e. a master with raised structures on the surface, obtained with lithography, models an elastomer generating structures whose dimensions can vary from hundreds of nanometers to hundreds of microns.

The key element of soft lithography is the elastomeric material able to model itself and take the shape of the microstructured surface of a rigid master. The most widely used elastomeric material is polydimethylsiloxane (PDMS). PDMS has unique properties because it has an

inorganic dorsal siloxane and silicon-bound organic methyl groups. It has a very low glass transition temperature, and therefore it is fluid at room temperature but can easily be converted into a solid state. The applications of elastomeric PDMS have been extensively studied and are well documented in the literature. The prepolymers and the cross-linking catalyst are sold from different companies and in large quantities. The procedure provides the mixture of elastomeric pre-polymer and catalyst and then, they are deposited by casting on the master made by lithography. The monomers or pre-polymers with the catalyst, also called curing agent, polymerize even at room temperature, but often the cross-linking reaction is accelerated putting the mixture and its master at temperatures between 60 and 90 ° C. The interfacial properties of PDMS elastomer can be easily changed by pre-polymer modifications or by surface plasma treatment. PDMS presents problems that still have to be solved in soft litography, firstly, during the curing it shrinks araund 1% and, once hardened, it spontaneously swells on contact with non-polar organic solvents such as hexane and toluene. Because of its elasticity it is subject to a process of thermal expansion and this leads to a difficult precision and reproducibility in nanofabrication (209).

5. Electronic microscopy

Electron microscopy (EM) is a technique for obtaining high resolution images of biological and non-biological specimens. It is used in biomedical research to investigate the detailed structure of tissues, cells, organelles and macromolecular complexes. The high resolution of EM images results from the use of electrons (which have very short wavelengths) as the source of illuminating radiation.

5.1. Scanning electron microscope (SEM)

In the SEM technique, an electron beam strikes the sample to be observed; the beam is not fixed but is scanned. Numerous particles are emitted from the sample, including secondary electrons, which are detected and converted into electrical impulses that reconstruct the image.

5.2. Transmission electron microscope (TEM)

The TEM is analogous in many ways to the conventional (compound) light microscope. In the TEM technique, the electrons that make up the beam pass completely through the sample. This, therefore, must have a reduced thickness, between 5 and 500 nm. The magnifying power is up to a million times.

The main difference between SEM and TEM is that SEM creates an image by detecting reflected or knocked-off electrons while TEM uses transmitted electrons (electrons which are passing through the sample) to create an image. As a result, TEM offers valuable information on the inner structure of the sample, such as crystal structure, morphology and stress state information, while SEM provides information on the sample's surface and its composition.

6. Atomic force Microscope (AFM)

The AFM technique is based on the measurement of the weak forces (nano Newtons) that are between a thin tip and the atoms on the sample surface. The tip is positioned on a flexible arm, cantilever, at a distance from the surface below the nanometer, when the sample is translated along the xy plane below the tip, between surface and tip there are attractive or repulsive forces with a consequent deflection of the tip in the z direction. Surface morphology is reconstructed from the measurements of tip deflection.

In the last years, Atomic Force Microscopy (AFM) has become a powerful tool not only to study the surface morphology but also the nanomechanics of all kind of samples. In particular, the AFM can be used to do Young Modulus and stiffness measurements. The AFM probe is used as a picoindentor: when the AFM probe touches the surface of sample it tries to penetrate the material , then the oppositional force of the sample is measured, this is the Stiffness (210).

7. Multisizer coulter counter

The machine provides size distribution in number, volume and surface area of the particles, with an overall sizing range of 0.4 µm to 1600 µm. Its response is unaffected by particle color, shape, composition or refractive index. Particles suspended in a weak electrolyte solution are drawn through a small aperture separating two electrodes through which an electric current flows. The voltage applied across the aperture creates a "sensing zone". As each particle passes through the aperture (or "sensing zone") it displaces its own volume of conducting liquid, momentarily increasing the impedance of the aperture. This change in impedance produces a tiny but proportional current flow into an amplifier that converts the current fluctuation into a voltage pulse large enough to measure accurately. The Coulter Principle states that the amplitude of this pulse is directly proportional to the volume of the particle that produced it. Scaling these pulse heights in volume units enables a size distribution to be acquired and displayed. In addition, if a metering device is used to draw a

known volume of the particle suspension through the aperture, a count of the number of pulses will yield the concentration of particles in the sample (211).

8. Dynamic Light scattering (DLS)

In DLS measurements the sample is illuminated by a laser beam, and the variations in intensity of the scattered light are measured as a function of time. The intensity variations measured by the detector are generated by the Brownian movement of the particles at the origin of the scattering. At the same temperature and viscosity, the "small" particles move rapidly - creating rapid variations in the scattering intensity - while the "large" particles move more slowly - creating slow intensity variations. The speed of the intensity variations is measured, and the particle diffusion coefficient calculated by the correlation function. Then, the Stokes - Einstein equation converts the diffusion coefficient into a hydrodynamic diameter. The measurement of the zeta potential serves to predict the dispersion stability or electrostatic interactions, and to measure the isoelectric point. Most particles or nanoparticles dispersed in water have a surface charge, caused by ionization or absorption of charged species. The charged particles are surrounded in solution by different ionic layers, whose composition is different from that of the bulk. When they move in solution (Brownian movement for example) the particles move together with a double ionic layer. The Zeta potential is the potential at the level of this double layer, also called the “slipping plane”. The zeta potential turns out to be the main force of the interactions between the particles, and it is very sensitive to the composition of the species loaded into the dispersion. For nanoparticles, particles that are small enough or of low density to remain suspended, the value of the Zeta Potential makes it possible to predict their stability. Indeed, a high zeta potential value (i.e. <30mV e> + 30mV) causes the nanoparticles to remain far from each other, repelling each other enough to eliminate the possibility of agglomeration, aggregation and / or flocculation (212).

b. A mathematical model perfectly predicts the effect of compressive stress on drug efficacy.

We assume that the total number of cells N varies in the spheroid according to

$$\dot{N} = \dot{N}_p - \dot{N}_d - \dot{N}_a,$$

where Np, Nd, Na are the number of proliferating cells, cells dying due to drug action and apoptosis, respectively. We assume that these terms have the following functional form:

$$\dot{N}_p = \gamma \int_V \rho\omega \, dV, \quad \dot{N}_d = \delta \int_V \rho\omega \, dV, \quad \dot{N}_a = \alpha \int_V \rho \, dV,$$

where ρ is the cellular density, γ, δ, α, are the proliferation, drug-induced death and apoptosis rates, respectively, and ω is the radial distribution of proliferating cells in the spheroid (see the SI of [1]). In the following we assume that cell proliferation is exponentially distributed over the spheroid radius, with a characteristic length l:

$$\omega = \exp\left(-\frac{R-r}{\ell}\right)$$

where r is the spheroid radial coordinate. We enforce spherical symmetry and write

$$\dot{N} = \frac{4}{3}\pi\dot{\rho}R^3 + 4\pi\rho R^2\dot{R},$$

and

$$\dot{N}_p - \dot{N}_d = 4\pi\rho(\gamma-\delta)\int_0^R e^{-\frac{R-r}{\ell}} r^2 \, dR, \quad \dot{N}_a = 4\pi\rho\alpha\int_0^R r^2 \, dR.$$

By calculating the integrals, we obtain

$$\frac{\dot{\rho}}{\rho}\frac{R}{3} + \dot{R} = (\gamma-\delta)\ell\left[1 - 2\frac{\ell}{R} + 2\frac{\ell^2}{R^2}\left(1 - e^{-\frac{R}{\ell}}\right)\right] - \frac{\alpha}{3}R.$$

We assume that the characteristic proliferation length is small if compared to the radius. Under this condition, the latter equation simplifies to

$$\frac{\dot{\rho}}{\rho}\frac{R}{3} + \dot{R} = (\gamma-\delta)\ell - \frac{\alpha}{3}R, \quad \ell \ll R.$$

The variation of cell density ˙ρ is linked to the pressure that is exerted on the spheroid. When spheroids are compressed by Dextran, this term can be set to zero over the timescale of spheroid growth. In the case of compression by agarose, however, pressure changes over time need to be taken into account. This happens because the spheroid deforms the agarose while growing and the gel responds elastically by exerting a pressure on the spheroid. We assume that under the deformation regime that occurs in our experiments the agarose can be described by a linear elastic behavior. Therefore, the variation of density ˙ρ and pressure P˙ can be linked by the following relation

$$\dot{\rho} = \frac{\rho}{\chi}\dot{P} = \frac{\rho}{\chi}\frac{4}{3}\frac{E}{R}\dot{R},$$

where χ is the spheroid compression bulk modulus. We have therefore

$$\left(1 + \frac{4}{9}\frac{E}{\chi}\right)\dot{R} = (\gamma - \delta)\ell - \frac{\alpha}{3}R,$$
$$\dot{R} = \frac{\gamma - \delta}{\beta}\ell - \frac{\alpha}{3\beta}R,$$
$$\dot{R} = \left(\frac{\gamma}{\beta}\ell - -\frac{\alpha}{3\beta}R\right) - \frac{\delta}{\beta}\ell,$$

where β = 1 + 4E/(9χ). Note that the proliferation rate and characteristic length γ and `, as well as the apoptotic rate α, depend on pressure and should be written as a function of spheroid radius. However, previous experimental work [1] as well as our observations (see Figure 1) suggest that the latter quantities reach an asymptotic value after a few kPa of pressure. Similar pressure values are obtained in the agarose gels that we consider even for small deformations, so that we can neglect the dependence of γ, ℓ and α on the spheroid radius and use directly their asymptotic values.

Since our experiments are performed over a timescale in which apoptotic death in the spheroid is not thoroughly developed, i.e. $\alpha t/(3\beta) \ll 1$, we rewrite the growth equation as

$$\dot{R} = g - d\frac{g}{g_0}$$

where g is the effective growth rate (including the early effects of cell apoptosis in the spheroid), and d is the death rate induced by the drug. In writing the last equation we assumed that d is independent of the external pressure acting on the spheroid. The dependence on

pressure is only considered for the growth rate g, which takes the value g0 in control conditions (i.e. no compression and no drug).

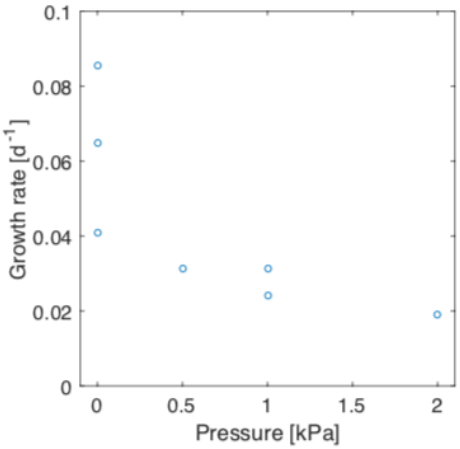

Figure 4: Growth rates estimated from the Dextran experiments.

Reference

[1] Fabien Montel et al. “Isotropic stress reduces cell proliferation in tumor spheroids”. In: New Journal of Physics 14.5 (2012), p. 055008.